

Extensions of the Verhulst Model, Order Statistics and Products of Independent Uniform Random Variables

Maria de Fátima Brilhante¹, Maria Ivette Gomes², and Dinis Pestana³

- ¹ Universidade dos Açores, DM, and CEAUL — Centro de Estatística e Aplicações da Universidade de Lisboa, Ponta Delgada, Portugal
(E-mail: fbrilhante@uac.pt)
- ² Universidade de Lisboa, Faculdade de Ciências, DEIO, and CEAUL — Centro de Estatística e Aplicações da Universidade de Lisboa; and Instituto de Investigação Científica Bento da Rocha Cabral, Lisboa, Portugal
(E-mail: ivette.gomes@fc.ul.pt)
- ³ Universidade de Lisboa, Faculdade de Ciências, DEIO, and CEAUL — Centro de Estatística e Aplicações da Universidade de Lisboa; and Instituto de Investigação Científica Bento da Rocha Cabral, Lisboa, Portugal
(E-mail: dinis.pestana@fc.ul.pt)

Abstract. Several extensions of the Verhulst sustainable population growth model exhibit different interesting characteristics more appropriate to deal with less controlled population dynamics. As the logistic parabola $x(1-x)$ arising in the Verhulst differential equation is closely related to the Beta(2,2) probability density, and the retroaction factor $1-x$ is the linear truncation of MacLaurin series of $-\ln x$ (the growth factor x is the linear truncation of $-\ln(1-x)$), in previous papers the authors introduced a more general four parameters family of probability density functions, of which the classical Beta densities are special cases. Using differential equations extending the original Verhulst, they have been able to identify combinations of parameters that lead to extreme value models, either for maxima or for minima, and also remarked that the traditional logistic model is a (geometric) extreme value model arising from geometric thinning of the original sequence. The observation that in the support $(0, 1)$ the logistic parabola $x(1-x)$ is, up to a multiplicative factor, the product of the densities of minimum and maximum of two standard independent uniform random variables (and also the median of three independent standard uniforms), and that on the other hand $(-\ln x)^{n-1}$ is, up to the multiplicative factor $1/\Gamma(n)$, the density of the product of n independent uniforms, we reexamine the ties of products and of order statistics of independent uniforms to dynamical properties of populations arising in these extensions of the Verhulst model.

Keywords: Extended Verhulst models, instabilities in population dynamics, products and order statistics of uniform random variables.



1 Extensions of the Verhulst model

Extensions of the classical Verhulst differential equation for modeling population dynamics

$$\frac{dN(t)}{dt} = rN(t)(1 - N(t)), \quad (1)$$

where $N(t)$ denotes the size of the population at time t and $r > 0$ is the malthusian reproduction rate, have recently been considered.

From the fact that the logistic parabola $x(1-x)$ arising from equation (1) is, in the support $(0, 1)$, closely tied to the Beta(2,2) probability density function (pdf), natural extensions of equation (1) using more general beta densities have been investigated by Aleixo *et al.* [1] and Pestana *et al.* [5], namely by considering the differential equation

$$\frac{dN(t)}{dt} = r(N(t))^{p-1}(1 - N(t))^{q-1}. \quad (2)$$

The normalized solution of equation (1) belongs to the family of logistic functions, which are connected to extreme value models, more precisely to max-geo-stable laws, and occurring in randomly stopped extremes schemes with geometric subordinator. On the other hand, Aleixo *et al.* [1] showed that the normalized solution of equation (2) also belongs to the class of max-geo-stable laws if $p = 2 - \alpha$ and $q = 2 + \alpha$ (the classical Verhulst model being the special case $\alpha = 0$).

By noticing that the retroaction factor $1 - x$ in the logistic parabola is the linear truncation of MacLaurin series of $-\ln x$, and that the growth factor x is the linear truncation of MacLaurin series of $-\ln(1 - x)$, Brillhante *et al.* [2] introduced a general four parameters family of densities, named the BeTaBoOp family, which was used to further extend equation (2) in Brillhante *et al.* [2] and [4].

Definition. A random variable X is said to have a BeTaBoOp(p, q, P, Q) distribution, with $p, q, P, Q > 0$, if its pdf is

$$f(x) = kx^{p-1}(1-x)^{q-1}(-\ln(1-x))^{P-1}(-\ln x)^{Q-1}I_{(0,1)}(x), \quad (3)$$

where $k^{-1} = \int_0^1 t^{p-1}(1-t)^{q-1}(-\ln(1-t))^{P-1}(-\ln t)^{Q-1}dt$ (Hölder's inequality guarantees that $k^{-1} < \infty$).

Observe that the Beta(p, q) density is the BeTaBoOp($p, q, 1, 1$) density. On the other hand, if in (3) $q = P = 1$, the Betinha(p, Q) density introduced by Brillhante *et al.* [3] is obtained, where $k = \frac{p^Q}{\Gamma(Q)}$ and $\Gamma(\alpha) = \int_0^\infty t^{\alpha-1}e^{-t}dt$ is the gamma function.

¹A random variable X is said to have a Beta(p, q) distribution, with $p, q > 0$, if its pdf is $f(x) = \frac{x^{p-1}(1-x)^{q-1}}{B(p,q)}I_{(0,1)}(x)$, where $B(p, q) = \int_0^1 t^{p-1}(1-t)^{q-1}dt$ is the Beta function.

Hence, for a general discussion of growth models, it seems interesting to investigate the general differential equation

$$\frac{dN(t)}{dt} = r(N(t))^{p-1}(1 - N(t))^{q-1}(-\ln(1 - N(t)))^{P-1}(-\ln N(t))^{Q-1}, \quad (4)$$

specially for the case when some of the parameters take the value 1.

Note that exact solutions exist for equation (4) for some special combinations of the parameters. However, when solving the related difference equation

$$x_{t+1} = c(x_t)^{p-1}(1 - x_t)^{q-1}(-\ln(1 - x_t))^{P-1}(-\ln x_t)^{Q-1}$$

by the fixed point method, bifurcation and chaos behavior is observed (see Brillhante *et al.* [2] and [4]).

2 Understanding population dynamics through order statistics and products of powers of uniform random variables

In section 1 we saw that the Verhulst differential equation and extensions are linked to BeTaBoOp densities. Using the fact that these densities can be expressed as functions of densities of order statistics and/or products of independent standard uniform random variables, we reexamine in this section the dynamical properties of populations described by the Verhulst model and extensions.

Let U_1, \dots, U_n be independent and identically distributed (iid) standard uniform random variables, and let $U_n^{(*)}$ denote their product, whose pdf is

$$f_{U_n^{(*)}}(u) = \frac{(-\ln u)^{n-1}}{\Gamma(n)} \mathbf{I}_{(0,1)}(u).$$

More generally, since $-\delta \ln U_i = -\ln U_i^\delta \curvearrowright \text{Exponential}(\delta)$, $i = 1, \dots, n$, $\delta > 0$, it follows that $V = -\sum_{i=1}^n \ln U_i^\delta = -\ln \prod_{i=1}^n U_i^\delta \curvearrowright \text{Gamma}(n, \delta)$. Therefore, $U_n^{\delta(*)} = \prod_{i=1}^n U_i^\delta = \exp(-V)$ has pdf

$$f_{U_n^{\delta(*)}}(u) = \frac{u^{1/\delta-1}(-\ln u)^{n-1}}{\delta^n \Gamma(n)} \mathbf{I}_{(0,1)}(u)$$

and distribution function

$$F_{U_n^{\delta(*)}}(u) = \frac{\Gamma(n, -\frac{\ln u}{\delta})}{\Gamma(n)} = u^{1/\delta} \sum_{k=0}^{n-1} \frac{(-\ln u)^k}{\delta^k k!}, \quad u \in (0, 1).$$

On the other hand, let $U_{k:n}$ denote the k -th ascending order statistic, whose pdf is

$$f_{U_{k:n}}(u) = \frac{u^{k-1}(1 - u)^{n-k}}{B(k, n + 1 - k)} \mathbf{I}_{(0,1)}(u),$$

i.e. $U_{k:n} \sim \text{Beta}(k, n + 1 - k)$. In particular, the pdf of the minimum $U_{1:n}$ is $f_{U_{1:n}}(u) = n(1-u)^{n-1} \mathbb{I}_{(0,1)}(u)$, and the pdf of the maximum $U_{n:n}$ is $f_{U_{n:n}}(u) = nu^{n-1} \mathbb{I}_{(0,1)}(u)$.

For the special case $n = 2$, it is obvious that $U_1 U_2 = U_{1:2} U_{2:2} \preceq U_{1:2} \preceq U_{2:2}$, and a similar result holds true for all $n \in \mathbb{N}$, $2 \leq n$.

Thus, when $p, q, P, Q \in \mathbb{N}$, the pdf of the $\text{BeTaBoOp}(p, q, P, Q)$ random variable is, up to a multiplicative factor, the product of the densities of the maximum $U_{p:p}$ of p independent standard uniforms, of the minimum $U_{1:q}$ of q independent standard uniform random variables, of the product $U_Q^{(*)}$ of Q independent standard uniform random variables, and of $1 - U_P^{(*)}$. Observe also that in the long-standing established jargon of population dynamics, the x^{p-1} and $(-\ln(1-x))^{P-1}$ are growing factors, and $(1-x)^{q-1}$ and $(-\ln x)^{Q-1}$ are retroaction factors, curbing down population growth. In view of the above remarks on the connection to ascending order statistics and products of independent standard uniform random variables, we shall say that $(-\ln x)^{\nu-1}$ is a lighter retroaction factor than $(1-x)^{\nu-1}$, and that $(-\ln(1-x))^{\mu-1}$ is a heavier growth factor than $x^{\mu-1}$.

In this perspective, it is expectable that the normalized solution of the differential equation linked to the $\text{Betinha}(2,2) \equiv \text{BeTaBoOp}(2,1,1,2)$ density, which can be obtained by replacing in (1) the retroaction factor $1 - N(t)$ by the lighter one $-\ln N(t)$, will correspond to less sustainable growth.

In fact, the solution of that differential equation is the Gompertz function, that up to a multiplicative factor is the extreme value Gumbel distribution. Observe that while the logistic distribution, which is a stable limit law for suitably linearly modified maxima of geometrically thinned sequences of iid random variables in its domain of attraction, is known to be appropriate to model sustainable growth, the Gumbel distribution arises as stable limit law of suitably normalized maxima of all the random variables in its domain of attraction, and therefore stochastically dominates the logistic solution, and is a suitable model for uncontrolled growth, such as the one observed for cells of cancer tumours.

More generally, Brillhante *et al.* [2] have shown that the normalized solution of the differential equation tied to the more general $\text{BeTaBoOp}(2, 1, 1, 2 + \alpha)$ density, i.e.

$$\frac{dN(t)}{dt} = rN(t)(-\ln N(t))^{1+\alpha}, \quad (5)$$

belongs to the class of extreme value laws for maxima, more precisely Gumbel if $\alpha = 0$, Fréchet if $\alpha > 0$ and Weibull for maxima if $\alpha < 0$. Therefore, equation (5) reveals to be more appropriate than (1) to deal with less controlled population dynamics.

² Note that Rachev and Resnick [6] established a connection between extreme stable laws and geometrically thinned extreme value laws, which implies, in particular, that when they have the same index — 0 in case of the Gumbel and of the logistic stable limits — they share the same domain of attraction.

On the other hand, if the growth factor $N(t)$ in (1) is replaced by $(-\ln(1 - N(t)))^{1+\alpha}$, we get a differential equation linked to the BeTaBoOp(1, 2, 2 + α , 1) density, whose normalized solution now belongs to the class of extreme value laws for minima. From the fact that if $X \sim \text{BeTaBoOp}(p, q, P, Q)$, then $1 - X \sim \text{BeTaBoOp}(q, p, Q, P)$, simplifies the investigations concerning the structural properties of the BeTaBoOp family, namely those related to products of uniform random variables.

Therefore, equations (1), (2) and (5) can be viewed as special cases of the more general differential equation (4) for modeling population dynamics, which embodies simultaneously two different growth patterns depicted in the growing terms $(N(t))^{p-1}$ and $(-\ln(1 - N(t)))^{P-1}$, and two different environmental resources control of the growth behavior, depicted in the retroaction terms $(1 - N(t))^{q-1}$ and $(-\ln N(t))^{Q-1}$.

We obtained explicit solutions for (4), using Mathematica, for a few special combinations of parameters, but so far only the ones connected with some form of stability and of extreme value models — either in the iid setting or in the geometrically thinned setting — seem to be suitable to characterize growth. In the sequel we shall comment on growth characteristics, in general, in terms of the order relation among parameters, and specially when all the parameters are integers.

3 Further comments for the special case of integer parameters

The Verhulst model is usually associated with the idea of sustainable growth. This is the case since the retroaction term $1 - N(t)$ slows down the growth impetus $rN(t)$, an equilibrium often interpreted as sustainability. Another way of seeing this is to observe that the logistic parabola $x(1 - x)$ tied to the Verhulst model is, up to a multiplicative factor, the product of the densities of the order statistics $U_{2:2}$ and $U_{1:2}$ — respectively, maximum and minimum of U_1 and U_2 . Therefore, the growth term ruled by $U_{2:2}$ has an “equal” opposite effect, exerted by the retroaction term ruled by $U_{1:2}$, which is curbing down the population growth to sustainable levels. On the other hand, we also observe that the logistic parabola is proportional to the density of $U_{2:3}$, i.e. the median of U_1 , U_2 and U_3 , thus reinforcing the idea of equilibrium.

We now amplify the above remarks to other interesting cases of the generalized Verhulst growth theory:

1. The logistic parabola generalization $x^{p-1}(1 - x)^{q-1}$, which is linked to the BeTaBoOp($p, q, 1, 1$) \equiv Beta(p, q) density, is:

- Proportional to the product of the densities of $U_{p:p}$ and $U_{1:q}$:

Since $U_{1:q} \preceq U_{p:p}$, for all $p, q \in \mathbb{N}$, and $U_{p:p}$ is associated with the growth term x^{p-1} , population growth is observed. However, if $p = q$, the retroaction term ruled by $U_{1:p}$ will curb down the population growth to sustainable levels, because $U_{1:p}$ and $U_{p:p}$ are equally distant order

statistics, in the sense that they are of the type $U_{k:n}$ and $U_{n-k+1:n}$. Therefore, when $p = q$, we may think that $U_{1:p}$ and $U_{p:p}$ are exerting equal opposite effects, ensuring this way a sustainable growth. On the other hand, if $p \neq q$, uncontrolled population dynamics is observed.

- Proportional to the density of $U_{p:p+q-1}$:

If $p = q$, then $U_{p:2p-1}$ is the median of $2p - 1$ iid standard uniform random variables, thus reinforcing the idea of sustainable growth, i.e. population equilibrium, as seen above. But if $p \neq q$, we are dealing with uncontrolled population dynamics, since $U_{p:p+q-1} \preceq U_{\lfloor (p+q-1)/2 \rfloor + 1:p+q-1}$ for $p < q$, and $U_{p:p+q-1} \succeq U_{\lfloor (p+q-1)/2 \rfloor + 1:p+q-1}$ for $p > q$, where $U_{\lfloor (p+q-1)/2 \rfloor + 1:p+q-1}$ is the median of $p + q - 1$ iid standard uniform random variables.

2. The expression $x^{p-1}(-\ln x)^{Q-1}$, which is linked to the BeTaBoOp($p, 1, 1, Q$) \equiv Betinha(p, Q) density, is:

- Proportional to the product of the densities of $U_{p:p}$ and $U_Q^{(*)}$:

From the fact that $U_Q^{(*)} \preceq U_{p:p}$, for all $p, Q \in \mathbb{N}$, the growth term is again the dominant one, and consequently population growth is also observed in this setting. Now the question is whether it is possible to have in this case sustainable growth. The answer is no, because if we compare the two retroaction terms $(1 - x)^{Q-1}$ and $(-\ln x)^{Q-1}$, which are proportional to the densities of $U_{1:Q}$ and $U_Q^{(*)}$, respectively, we have $U_Q^{(*)} \preceq U_{1:Q}$. Therefore, $U_Q^{(*)}$ is exerting a weaker control effect on population growth than $U_{1:Q}$ would, which leads necessarily to unsustainable population growth, even if $Q = p$.

- Proportional to the density of $U_Q^{1/p(*)}$, which applies to the more general case $p > 0$:

By noting that $U_Q^{1/p(*)} = \left(U_Q^{(*)} \right)^{1/p}$, it follows that $U_Q^{1/p(*)} \preceq U_Q^{(*)}$ if $p > 1$, and $U_Q^{(*)} \preceq U_Q^{1/p(*)}$ if $p < 1$. Comparing $U_Q^{1/p(*)}$ and $U_Q^{(*)}$ with $U_{1:Q}$, associated with the retroaction factor $(1 - x)^{Q-1}$, we conclude that:

- (i) if $p > 1$, $U_Q^{(*)} \preceq U_{1:Q}$, thus revealing that $U_Q^{1/p(*)}$ has a weaker control effect on population growth, as already unveiled above;
- (ii) if $p < 1$, $U_{1:Q} \preceq U_Q^{1/p(*)}$, therefore showing that $U_Q^{1/p(*)}$ has a stronger control effect on population growth.

Both cases are suitable to model unsustainable population growth.

3. The expression $(1-x)^{q-1}(-\ln(1-x))^{P-1}$, tied to the BeTaBoOp(1, q, P, 1) density, is proportional to the product of the densities of $U_{1:q}$ and $1-U_P^{(*)}$, associated with the retroaction and growth terms $(1-x)^{q-1}$ and $(-\ln(1-x))^{P-1}$, respectively.

Since $U_{1:q} \preceq 1-U_P^{(*)}$ for all $q, P \in \mathbb{N}$, the growth factor is the dominant one, and therefore population growth will also happen. On the other hand, the fact that $U_{P:P} \preceq 1-U_P^{(*)}$, where $U_{P:P}$ is associated with the (absent) growth term x^{P-1} , shows that in this case we have a strong growth impetus, counteracted by growth control mechanisms influenced by $U_{1:q}$. Note that $U_{1:q}$ exerts a stronger control effect than $U_q^{(*)}$ would on population growth. Hence, this case is also suitable for modeling populations with unsustainable growth, as the previous one, but where a more uncontrolled population growth is observed.

Also note that Brillhante *et al.* [2] showed that the normalized solution for the differential equation linked to the BeTaBoOp(1, 2, 2 + α, 1) density belongs to the class of extreme value laws for minima, which seems to be the consequence of the higher control forces needed to refrain the more uncontrolled population growth through the influence of $U_{1:q}$.

4. The expression $x^{p-1}(-\ln(1-x))^{P-1}$, tied to the BeTaBoOp(p, 1, P, 1) density, is proportional to the product of the densities of $U_{p:p}$ and $1-U_P^{(*)}$, with $U_{p:p} \preceq 1-U_P^{(*)}$ only if $p \leq P$. Thus, the growth pattern which is linked with the factor x^{p-1} is the dominant one, whenever $p \leq P$.

On the other hand, since the growth control mechanisms are absent in this setting, the associated differential equation is ideal for modeling populations that almost surely grows to infinity, extinction being almost impossible.

5. The expression $(1-x)^{q-1}(-\ln x)^{Q-1}$, linked to the BeTaBoOp(1, q, 1, Q) density, is proportional to the product of densities of $U_{1:q}$ and $U_Q^{(*)}$, where $U_Q^{(*)} \preceq U_{1:q}$ if $q \leq Q$. Therefore, the retroaction term tied to $(1-x)^{q-1}$ is the dominant one, whenever $q \leq Q$.

Given that we only have growth control factors in this case, the corresponding differential equation is useful for modeling populations that are almost surely doomed to extinction.

6. The expression $x^{p-1}(1-x)^{q-1}(-\ln x)^{Q-1}$, tied to the BeTaBoOp(p, q, 1, Q) density, is proportional to the product of the densities of $U_{p:p}$, $U_{1:q}$ and $U_Q^{(*)}$, with $U_Q^{(*)} \preceq U_{1:q} \preceq U_{p:p}$ if $q \leq Q$. Again population growth is noticed since the dominant term is the growth term.

However, when $p = q = Q$, $U_{1:p}$ manages to “compensate” the growth effect of $U_{p:p}$ by curbing down the population growth to sustainable levels. This action is reinforced by the other retroaction term $(-\ln x)^{p-1}$ ruled by $U_p^{(*)}$. A more interesting case occurs when the growing parameter p and

the retroaction parameters q and Q meet an equilibrium, in the sense that $p = q + Q$.

7. The expression $x^{p-1}(1-x)^{q-1}(-\ln(1-x))^{P-1}$, which is linked to the BeTaBoOp($p, q, P, 1$) density, is proportional to the product of the densities of $U_{p:p}$, $U_{1:q}$ and $1 - U_P^{(*)}$, with $U_{1:q} \leq U_{p:p} \leq 1 - U_P^{(*)}$ for $p \leq P$.

Uncontrolled population growth is the case again even if $p = q = P$. This is so because although $U_{1:p}$ “compensates” the effect of $U_{p:p}$, it does not do the same for the growth term ruled by $1 - U_P^{(*)}$, whose influence is stronger than $U_{p:p}$. However, equilibrium is observed whenever the growing parameter p and P and the retroaction parameter q verify the relation $p + P = q$.

8. The expression $x^{p-1}(1-x)^{q-1}(-\ln(1-x))^{P-1}(-\ln x)^{Q-1}$, which is linked to the BeTaBoOp(p, q, P, Q) density, is proportional to the product of the densities of $U_{p:p}$, $U_{1:q}$, $1 - U_P^{(*)}$ and $U_Q^{(*)}$, where $U_Q^{(*)} \leq U_{1:q} \leq U_{p:p} \leq 1 - U_P^{(*)}$ if $p \leq P$ and $q \leq Q$.

In this setting equilibrium is observed when $p + P = q + Q$.

Acknowledgements

This research has been supported by National Funds through FCT — Fundação para a Ciência e a Tecnologia, project PEst-OE/MAT/UI0006/2011.

References

1. Aleixo, S., Rocha, J.L., and Pestana, D., Probabilistic Methods in Dynamical Analysis: Population Growths Associated to Models Beta (p, q) with Allee Effect, in Peixoto, M. M.; Pinto, A.A.; Rand, D.A.J., editors, *Dynamics, Games and Science, in Honour of Maurício Peixoto and David Rand*, vol II, Ch. 5, pages 79–95, New York, Springer Verlag, 2011.
2. Brillhante, M.F., Gomes, M.I., and Pestana, D., BetaBoop Brings in Chaos. *Chaotic Modeling and Simulation*, 1: 39–50, 2011.
3. Brillhante, M.F., Pestana, D., and Rocha, M.L., Beticos, *Bol. Soc. Port. Matemática*, 177–182, 2011.
4. Brillhante, M.F., Gomes, M.I., and Pestana, D., Extensions of Verhulst Model in Population Dynamics and Extremes, *Chaotic Modeling and Simulation*, 2(4): 575–591, 2012.
5. Pestana, D., Aleixo, S., and Rocha, J.L., Regular variation, paretian distribution, and the interplay of light and heavy tails in the fractality of asymptotic models, in Skiadas, C.H., I. Dimotikalis, I., and Skiadas, C. (eds), *Chaos Theory: Modeling, Simulation and Applications*, Singapore, 2011. World Scientific, 309–316.
6. Rachev, S.T., and Resnick, S., Max-geometric infinite divisibility and stability, *Communications in Statistics — Stochastic Models*, 7:191–218, 1991.

Multifractal and Energy Parameters Can Underlie an Express Diagnostics of the Human Motor Dysfunction

Olga E. Dick

Physiology of Russian Academy of Science, St. Petersburg, Russia
E-mail: glazov.holo@mail.ioffe.ru

Abstract. The aim is to determine characteristics of tremor determined as fast involuntary shaking and arising during the performance of the motor task by healthy subjects and patients with akinetic-rigid form of Parkinson's disease. The motor task is to keep the force by hands under isometric conditions (without finger movement in space). The tremor (the fast component) isolated from the registered trajectory of the isometric force varies by the amplitude for healthy and parkinsonian subjects but it poorly differs by frequency making difficulties in distinguishing frequency spectra. The wavelet multilevel decomposition and multifractal analysis allowed us to compare the numerically expressed energy and multifractal parameters of tremor instead of the registered trajectories. At each decomposition level the energy parameters of physiological tremor are less than for parkinsonian tremor. The parkinsonian impairment degree correlates with deviation of the parameter values from the values obtained for the healthy persons. Antiparkinsonian drug administration in the dose usual for the parkinsonian patients leads to a decrease of differences between both the energy and multifractal parameters for the healthy and parkinsonian subjects. Thus, the considered energy and multifractal characteristics can underlie an express diagnostics of the human motor dysfunction and determine the strategy of selection of optimal drugs for relieving parkinsonian tremor.

Keywords: Parkinson's disease, Tremor, Wavelet decomposition, Multifractal.

1 Introduction

Involuntary shaking (tremor) of a body part can accompany some motor tasks, e.g., sustaining effort of fingers [1]. The mechanism underlying these involuntary oscillations appears to be related to discharges in feedback loops between motor cortical areas and basal ganglia and in the transcortical loop between the somatosensory and motor cortical areas [1, 2, 3]. Tremor may result from mechanical resonance in muscles and mobile parts of the skeleton, with the resonance frequency depending on the stretching strength applied to the limbs [4]. Under normal conditions, involuntary shaking has a small amplitude and does not impair motor performance [5]. The dispersion of frequency of involuntary oscillations from 8 to 12 Hz indicates asynchronous firing of individual motor units and a delay of the spread of impulses along feedback loops [6, 7]. If a task requires fine control of the steady positions of fingers,



tremor in the 16–50 Hz range is added [8]. The appearance of high frequency oscillations is usually related to the involvement of sensory information processing.

Pathological tremor disrupting the movement performance or posture maintenance is specified by a higher amplitude than physiological tremor has. It is related to an increasing synchronization of motor units. For example, synchronization of neurons in the nuclei of the thalamus and basal ganglia, from which descending signals are indirectly transmitted to the muscles explains the large tremor of 3–6 Hz typical for patients with Parkinson's disease [1]. We studied tremor arising during keeping the force by hands under isometric conditions (without finger movement in space). Sometimes, especially in the case of akinetic–rigid parkinsonian form this considerably nonstationary tremor does not differ noticeably in frequency in comparison with healthy subjects [9].

The aim of the work is to find scores giving evaluation of differences in involuntary shaking of fingers by performing a motor task by a healthy subject and a patient with Parkinson's disease. For estimating the nonstationary signal features we use methods of nonlinear dynamics, namely, wavelet transform and multifractal analysis, which allow us to compare the numerically expressed energy parameters and scaling exponents of tremor. This analysis may serve as the basis for a diagnostics of the human motor dysfunction.

2 The experimental procedure

We used the results of testing 12 healthy subjects aged 43–54 years and 10 parkinsonian patients with bilateral akinesia and tremor aged 45–62 years. The motor task was to control the isometric muscle effort with the strength of muscle contraction shown by the positions of marks on a monitor. The subjects sat in front of a monitor standing on a table and pressed on platforms containing stress sensors with their fingers. The sensors transformed the pressure strength of the fingers of each hand into an electric signal. The rigidity of the platforms made it possible to record the effort in the isometric mode, i.e., without noticeable movement of fingers at the points of contact with the sensors. The isometric effort was recorded for 30 s in tests of two types: in the first test, the subject's fingers sustained an upward muscle effort, with the back of each hand pressing against the base of the platform; in the second test, the effort was downward. In both cases, the subject's arms were straightened.

The patients with Parkinson's disease did not take any drugs before the test on the day of testing. Usually, these patients received nakom, an antiparkinsonian preparation containing levodopa and carbidopa (a decarboxylase inhibitor) at doses of 200 and 50 mg, respectively, three times a day to compensate for dopamine deficiency.

The recorded trajectory of isometric effort consisted of a slow trend and a fast involuntary component (tremor), which was isolated from the recorded trajectory using the MATLAB software.

3 Wavelet transform and multifractality

3.1 Estimation of parameters of the energy spectral density of tremor

The algorithm of multilevel wavelet decomposition and reconstruction of a signal allows to represent the analyzed signal as the sum

$$x(t_i) = A_m(t_i) + D_m(t_i) + \dots + D_1(t_i),$$

where the component $A_m(t_i)$ gives the coarse approximation to the initial signal at the m^{th} level of decomposition and $D_1(t_i), \dots$ and $D_m(t_i)$ determine details. The component $D_1(t_i)$ characterizes details at the highest frequencies. Thus, the algorithm permits to elucidate features of the signal at various frequencies. The central frequency of the wavelet corresponding to the j^{th} level of decomposition was calculated as $f_r f_s / 2^j, j = 1, \dots, m$, where $f_s = 50$ Hz is the sampling frequency and $f_r = 0.71$ is the central frequency of the mother Daubechies wavelet db_4 used in this work. To analyze the tremor details we used the method for estimating parameters of the energy spectral density of a signal [9].

Let $S(f)$ be the energy spectral density of the component $D(t)$ equal to the square of the Fourier transform:

$$S(f) = \left| \int D(t) e^{-2\pi i f t} dt \right|^2.$$

Then the total energy accumulated in the frequency range $[f_1, f_2]$ is

$$e = \int_{f_1}^{f_2} S(f) df.$$

As an energy parameter of the energy spectral density we use the value

$$k = e_{\max} / ((f_2 - f_1) f_{\max}),$$

where f_{\max} is the frequency value corresponding to e_{\max} and the frequencies f_1 and f_2 correspond to values $0.05 * S_{\max}$ and $0.95 * S_{\max}$. Thus, the frequency range $[f_1, f_2]$ specifies the energy spectrum kept after 5% filtration of noise.

The parameter k describes the relation between the maximal accumulation of the signal energy, the frequency corresponding to the maximum of the energy spectral density, and the frequency range $[f_1, f_2]$ at which the energy is accumulated.

3.2 Estimation the global wavelet spectrum of the tremor

To evaluate the difference between physiological and pathological tremors, we used the wavelet transform modulus maxima (WTMM) method [10] based on the continuous wavelet transform of a time series describing the examined tremor $x(t)$:

$$W(a, t_0) = a^{-1} \int_{-\infty}^{+\infty} x(t) \psi^* \left((t - t_0) / a \right) dt,$$

where a and t_0 are the scale and space parameters, $\psi((t - t_0)/a)$ is the wavelet function obtained from the basic wavelet $\psi(t)$ by scaling and shifting along the time, symbol * means the complex conjugate. As the basic wavelet we use the complex Morlet wavelet:

$$\psi(t) = D \exp(-0.5t^2) [\exp(-i\omega_0 t) - \exp(-0.5\omega_0^2)],$$

where the function

$$D = \frac{\pi^{-1/4}}{\sqrt{1 - 2 \exp(-0.75\omega_0^2) + \exp(-\omega_0^2)}}.$$

The value $\omega_0 = 2\pi$ gives the simple relation between the scale a and the frequency f : $f = 1/a$.

The modulus of the wavelet spectrum $|W(f, t_0)|$ characterizes the presence and intensity of the frequency f at the moment t_0 in the signal and $|W(f, t_0)|^2$ describes the instantaneous distribution of the tremor energy over frequencies, that is, the local spectrum of the signal energy at the time t_0 .

The value

$$E(f) = \int_{t_1}^{t_2} |W(f, t_0)|^2 dt_0$$

determines the global wavelet spectrum, i.e., the integral distribution of the wavelet spectrum energy over frequency range on the time interval $[t_1, t_2]$.

3.3 Estimation the tremor multifractality

Information about possible multifractal feature of the signal and its localization t_0 reflects in the asymptotic behavior of coefficients $|W(a, t_0)|$ at small a

values and large f values, respectively. The faster the wavelet coefficients decrease at $f \rightarrow \infty$, the more regular the signal is around that point. Abnormal small decrease of the wavelet coefficients at $a \rightarrow 0$ in a neighborhood of the point t_0 testifies about singularity of the signal at the point. Thus, the rate of the change of the modulus of the wavelet coefficients enables to analyze the presence or absence of singularities of the signal.

The degree of singularity of the signal $x(t)$ at the point t_0 is described by the Hölder exponent, $h(t_0)$, the largest exponent such that the analyzed signal in a neighborhood of the point t_0 can be represented as the sum of the regular component (a polynomial $P_n(t)$ of order $n < h(t_0)$) and a member describing a non - regular behavior [10]:

$$x(t) = P_n(t) + c|t - t_0|^{h(t_0)}.$$

The value $h(t_0)$ is the measure of singularity of the signal at the point t_0 since the smaller $h(t_0)$ value, the more singular the signal.

In view of the simple dependence $W(a, t_0) \sim a^{h(t_0)}$ at $a \rightarrow 0$ [10], the Hölder exponent can be calculated by

$$h(t_0) \sim \log_{10} W(a, t_0) / \log_{10} a.$$

However, with increasing the scale a the influence of neighbouring nonregularities can lead to inaccuracy, that is why we determined the Hölder exponents on the basis of statistical description of local singularities by partition functions [11].

The algorithm consists of the following procedures.

- 1) The continuous wavelet transform of the time series is used.
- 2) A set $L(a)$ of lines of local modulus maxima of the wavelet coefficients is found at each scale a
- 3) The partition functions are calculated by the sum of q - powers of the modulus maxima of the wavelet coefficients along the each line at the scales smaller the given value a :

$$Z(q, a) = \sum_{l \in L(a)} \left(\sup_{a^* \leq a} |W(a^*, t_l(a^*))| \right)^q,$$

$t_l(a^*)$ determines the position of the maximum corresponding to the line l at this scale

- 4) By the fact that the partition function is $Z(q, a) \sim a^{\tau(q)}$ at $a \rightarrow 0$ [11], the scaling exponent can be extracted as

$$\tau(q) \sim \log_{10} Z(q, a) / \log_{10} a.$$

5) Choosing different values of the power q one can obtain a linear dependence $\tau(q)$ with a constant value of the Hölder exponent

$$h(q) = d\tau(q)/dq = \text{const}$$

for monofractal signals and nonlinear dependence $\tau(q) = qh(q) - D(h)$ with large number of the Hölder exponents for multifractal signals.

6) The singularity spectrum (distribution of the local Hölder exponents) is calculated from the Legendre transform [11]:

$$D(h) = qh(q) - \tau(q).$$

Using the global wavelet spectra and the WWTM algorithm for the different tremor recording we obtain the maximum of the global tremor energy (E_{\max}) and two multifractal parameters:

a) the width of the singularity spectrum

$$\Delta h = h_{\max} - h_{\min},$$

where h_{\max} and h_{\min} are the maximal and minimal values of the Holder exponent corresponding to minimal and maximal tremor fluctuation, respectively;

b) the asymmetry of the singularity spectrum

$$\Delta = |\Delta_2 - \Delta_1|,$$

where $\Delta_1 = h_{\max} - h_0$ and $\Delta_2 = h_0 - h_{\min}$, $h_0 = h(q = 0)$.

Smaller Δh indicates that the time series tends to be monofractal and larger Δh testifies the enhancement of multifractality. The asymmetry parameter Δ characterizes where, in the region of strong singularities ($q > 0$) or in the region of weak singularities ($q < 0$), the singularity spectrum is more concentrated.

To compare the mean values in each of the examined group of subjects the Student criterion was applied.

4 Results and discussion

Two components of oscillations of the isometric force trajectory of the human hand, namely, slow trend and tremor, are given in Fig. 1 for the healthy subject (Fig. 1a) and for the parkinsonian patient before (Fig. 1b) and after nakom medication (Fig. 1c). The amplitude of parkinsonian tremor is nearly twice larger than physiological tremor isolated for the healthy subject. Two hours after nakom medication the parkinsonian tremor reduced by amplitude to the values specified for the healthy subject. The differences in slow components were not essential.

The right column of Fig. 1 shows the curves $\tau(q)$ (Fig. 1d), $h(q)$ (Fig. 1e) and the singularity spectra $D(h)$ for the same subjects. The nonlinear dependence $\tau(q)$ indicates the large number of Hölder exponents. These dependences and the form of singularity spectrum $D(h)$ testifies the multifractality of both physiological and parkinsonian tremor. However, the Hölder exponents differ for the two subjects. The differences are maximal at weak fluctuations ($q < 0$).

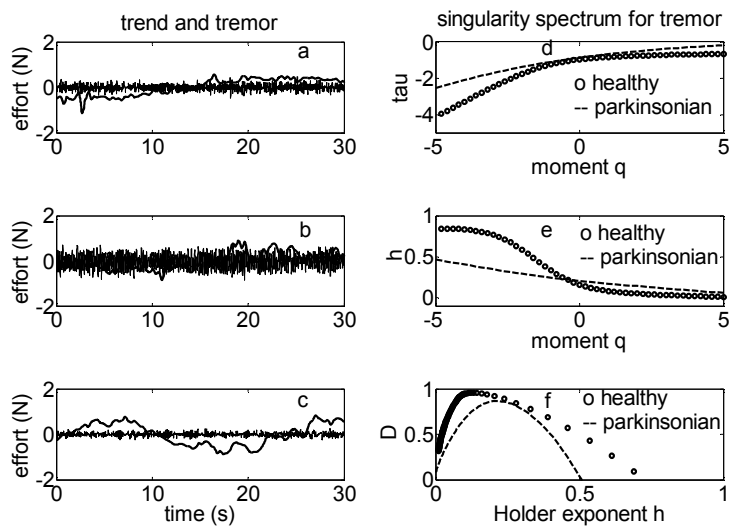


Fig. 1. Examples of two components of the isometric force trajectory of the human hand (slow trend and tremor) for a healthy subject (a) and for a patient with Parkinson disease before the drug administration (b) and after (c). Multifractal curves for tremor: $\tau(q)$ (d), $h(q)$ (e) and singularity spectra $D(h)$.

The healthy tremor is characterized by the largest width Δh and, therefore, by the significant degree of multifractality. The decline in the width of the singularity spectrum shows a reduction of nonuniformity of the parkinsonian tremor and a fall in the multifractality degree.

The singularity spectrum asymmetry Δ is also larger for healthy tremor and for parkinsonian one the value of Δ is close to 0.1.

The decrease of the both parameters in tremor of patients with Parkinson's disease is due to decreasing contribution of weak fluctuations (for $q < 0$).

In healthy tremor the singularity spectrum is expanded so that the dynamics of persistent sequences exhibits both anticorrelated (for $h < 0.5$) and correlated (for $h > 0.5$) behavior.

The decrease of h_{max} in parkinsonian tremor as compared with the physiological one testifies about the enhancement of the anticorrelation degree so that the

tremor tend to become more random and less smooth. The consequent values are anticorrelated ($h < 0.5$), i.e., persistent sequences in pathological tremor are characterized by stochastically up - down patterns in which large values are more likely to be followed by small values and vice versa.

Antiparkinsonian drug administration leads to the increase of the multifractal parameters increasing both the width and the asymmetry of the singularity spectrum.

The energy parameter k enhances with increasing the decomposition level (Fig. 2). For the healthy tremor the means of k values are less than for the parkinsonian one on all the levels. The differences between the parameter k values for the healthy and parkinsonian subjects reduce with increasing the decomposition level. Maximal differences (in three orders) are observed at the first level that is for the high frequency details. This level specifies frequencies located near 17.8 Hz. At the last decomposition level the means of k values distinguish much less. But even at the fourth level with frequencies close to 2.2 Hz the values differ.

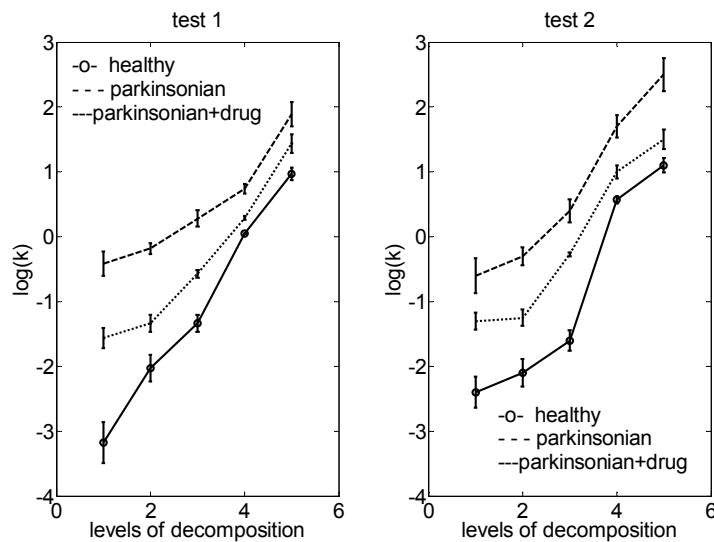


Fig.2 Dependences of mean values of the energy parameter k on the decomposition level. The solid line corresponds to the healthy tremor, the dashed lines specifies the parkinsonian tremor before and after nakom administration.

Antiparkinsonian drug administration in the dose usual for the parkinsonian patients leads to a decrease of differences between means of k for the healthy and parkinsonian subjects at all the decomposition levels. This testifies that two hours after medication of the drug compensating deficit of dopamine in basal ganglia tremor arising during maintenance of isometric force by the

parkinsonian subject becomes similar to physiological tremor by the energy parameter of the spectral density of the tremor detail components. Calculation of the instantaneous frequency - time distributions $|W(f, t_0)|^2$ and global wavelet spectra $E(f)$ enables us to find the enormous enhancement (about in 300 times) of the maximal global energy E_{\max} in parkinsonian tremor as compared with the healthy one (Fig.3).

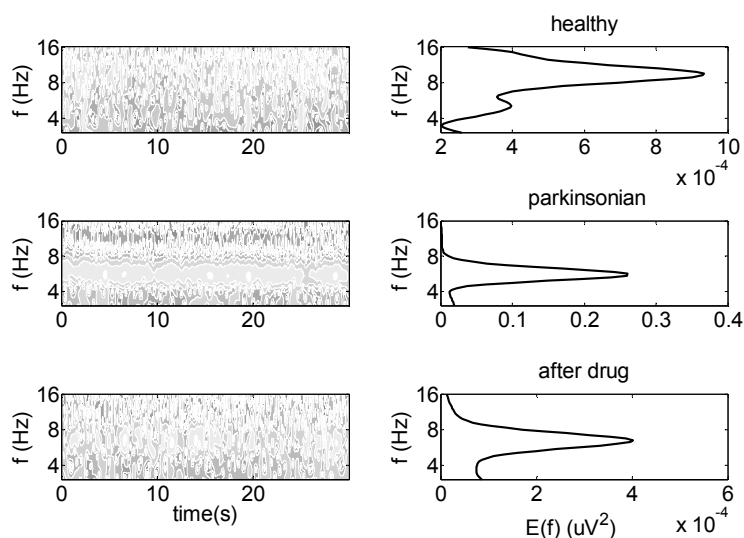


Fig. 3. Examples of the instantaneous frequency-time distributions of the tremor energy $|W(f, t_0)|^2$ (left column) and global wavelet spectra $E(f)$ (right column) for the same subjects as in Fig.1.

The maximal value E_{\max} of physiological tremor is in the frequency range of alpha rhythm [8, 14] Hz. For the pathological tremor E_{\max} is shifted in the theta range [4, 7.5] Hz. Two hours later after antiparkinsonian drug medication the energy value dramatically reduces to the value specified for the healthy volunteers.

The similar dynamics of the energy and multifractal parameters is observed for all the examined subjects. It enables us to use the common practice of averaging the recordings of all subjects for testing significant variations among the groups. The values of E_{\max} , Δh and Δ averaged by subjects in every group are given in Table 1. The significant distinctions between the states (pathological or physiological tremor) are identified by all the three parameters ($p=0.02$, $p=0.03$ and $p=0.01$, respectively).

state	test	hand	E_{\max}^* 10^{-4}	Δh	Δ	clinical manifes- tation of tremor
healthy	1	right	7.5±0.3	0.75±0.06	0.37±0.03	no
		left	6.8±0.2	0.82±0.07	0.42±0.04	
	2	right	8.7±0.3	0.78±0.07	0.38±0.04	
		left	7.9±0.3	0.69±0.05	0.45±0.05	
parkinsonian	1	right	2150±115	0.34±0.03	0.14±0.03	yes
		left	2397±146	0.29±0.02	0.19±0.01	
	2	right	1976±101	0.38±0.02	0.11±0.01	
		left	2110±131	0.41±0.03	0.15±0.01	
parkinsonian 2 hours after drug medication (68% patients)	1	right	5.2±0.1	0.81±0.08	0.51±0.05	no
		left	8.2±0.3	0.86±0.07	0.56±0.05	
	2	right	9.3±0.3	0.71±0.07	0.41±0.04	
		left	7.3±0.2	0.74±0.07	0.54±0.04	
parkinsonian 2 hours after drug medication (32% patients)	1	right	1870±106	0.43±0.03	0.13±0.01	yes
		left	1687±92	0.35±0.02	0.17±0.01	
	2	right	1933±113	0.42±0.02	0.22±0.01	
		left	1881±103	0.37±0.02	0.15±0.01	

Table 1. Comparison of the mean values, averaging over subjects inside the every examined group. The subject's fingers sustained an upward muscle effort (test 1) and downward effort (test 2).

Our results demonstrate that clinical manifestation of tremor is correlated with the significant enhancement of the maximal global energy and the decrease of the width and the asymmetry of the singularity spectrum. The disappearance of the clinical features of the pathological tremor in 68 % of the examined patients is accompanied by approximation of the multifractal and energy parameters to the values obtained for the healthy subjects.

We have shown that parkinsonian damage of the brain leads to the characteristic breakdown or modification in the long-range correlations of neuronal activity that can be a useful indicator of a dysfunctional network in the central nervous system.

The long-range correlations can be related to fractality of intracellular process defining the amplitude and the velocity of the action potential propagation. So, the long-range correlations of sequences of life time of ion channels and

dynamics of change in the membrane - binding calcium concentration have been shown in [12]. The long-term memory in ion channel dynamics leads to the memory in fluctuations of a nerve fiber excitability [13]. An increase of the number of excitable fibers during propagation of rhythmical impulses is accompanied by a decrease of the long-range correlations in sequences of the action potential amplitudes and an increase of correlations in the velocities of the action potential propagation [14]. It may underlie the reduction of the long-term memory for parkinsonian disruption of the central control by movements as evidenced by the increasing synchronization and decrease of the multifractality of involuntary oscillations.

Conclusions

Our examination of differences in physiological and pathological tremor arising during the maintenance of isometric force by hands of a healthy subject and a subject with Parkinson's disease demonstrates that the energy parameters and multifractal characteristics can serve as estimations of the human motor dysfunction since their values reflect the degree of deviation of pathological involuntary oscillations from the normal ones.

References

1. J. H. McAuley, C. D. Marsden. Physiological and pathological tremors and rhythmic central motor control. *Brain*, 123, 8, 1545-1567, 2000.
2. C. D. Marsden. Origins of normal and pathological tremor. In: Findley L. J., Capildeo R. (eds) *Movement disorders: tremor*. MacMillan Press, London, 37-84, 1984.
3. B. Vallbo, J. Wessberg. Organization of motor output in slow finger movements in man, *J. Physiol.*, 469, 673-691, 1993.
4. S. F. Farmer, M. Swash, D. A. Ingram, J. A. Stephens. Changes in motor unit synchronization following central nervous lesions in man, *J. Physiol.*, 463, 83-105, 1993.
5. R. Elble. Physiologic and essential tremor, *Neurology*, 36, 225-231, 1986.
6. S. Grillner. The motor infrastructure: from ion channels to neuronal networks, *Nature Reviews Neuroscience*, 4, 573- 586, 2003.
7. J. H. McAuley, J. C. Rothwell, C. D. Marsden Frequency peaks of tremor, muscle vibration and electromyographic activity at 10 Hz, 20 Hz and 40 Hz during human finger muscle contraction may reflect rhythmicities of central neural firing, *Exp. Brain Res.*, 114, 525-541, 1997.
8. G. P. Van Galen, R. R. Van Doorn, L. R. Schomaker. Effects of motor programming on the power spectral density function of finger and wrist movements, *J. Exper. Psychol.*, 16, 755- 765, 1990.
9. O. E. Dick, S. P. Romanov, A. D. Nozdrachev. Energy and Fractal Characteristics of Physiological and Pathological Tremors of the Human Hand, *Human Physiology*, 36, 2, 203-210, 2010.
10. J. F. Muzy, E. Bacry, A. Arneodo. Multifractal formalism for fractal signals: the structure-function approach versus the wavelet-transform modulus-maxima method, *Phys. Rev. E*, 47, 875-884, 1993.

11. Arneodo, E. Bacry, J. F Muzy. The thermodynamics of fractals revisited with wavelets. *Physica A*, 213, 232-275, 1995.
12. W. A. Varanda, L. S. Liebovitch, J. N. Figueroa, R. A. Nogueira. Hurst analysis applied to the study of single calcium - activated potassium channel kinetics. *J. Theor. Biol.*, 206, 343- 353, 2000.
13. S. B. Lowen, L. S. Liebovitch, J. A. White. Fractal ion – channel behaviour generates fractal firing patterns in neuronal models. *Phys. Rev. E.*, 59, 5970 – 5980, 1999.
14. R. Brazhe, G. V. Maksimov. Self – organized critical gating of ion channels: on the origin of long – term memory in dwell time series. *Chaos*, 16, 33129 - 33135, 2006.

Acknowledgements

A part of the work was supported by the Program of Presidium of RAS “*Fundamental sciences for medicine in 2014 year*”

The Mechanisms of Chaotization in Switching Power Converters with Compensation Ramp

Dmitrijs Pikulins

Riga Technical University, Riga, Latvia
E-mail: dmitrijs.pikulins@rtu.lv

Abstract: Recently much attention has been paid to investigation of nonlinear dynamics of switching power converters, as this kind of dynamical systems, being inherently hybrid, is capable of exhibiting a wide variety of well known smooth as well as novel non-smooth phenomena. This research shows the diversity of complex interactions of smooth bifurcations and border collisions in one of the most typical power circuits – boost converter under current mode control – applying the method of complete bifurcation groups. The effects of realistic parameters and implementation of compensation signals on the robustness of chaotic modes of operation are investigated and explained in details.

Keywords: Bifurcations, Chaos, Non-smooth phenomena, Switching power converters.

1. Introduction

It is common knowledge for the majority of engineers working in the field of power electronics, that the only acceptable operating regime of switching power converters (SPC) is the period-1 (P1) mode, when all waveforms repeat at the same rate as driving clock element. So, all the efforts of practicing engineers are directed to insurance of stable operation of DC-DC converters, eliminating the possibilities of occurrence of any subharmonic oscillations. On the other hand, recent investigations have shown that the operation of SPC in subharmonic or even chaotic modes allows achieving higher performance characteristics of these devices. In example, paper [1] presents the novel control strategy, allowing simple digital implementation and excellent transient response. The idea of the control is based on the use of various combinations of two different control pulses that from the point of view of nonlinear dynamics could be treated as operation in a variety of subharmonic regimes. The other research [2] shows the applicability of inherently arising chaotic modes of operation of switching converters to the reduction of high levels of electromagnetic noise, generated by this kind of devices. Thus it has been demonstrated, that contrary to generally accepted opinion, the non-linear operating modes of switching converters could be efficiently utilized, providing new progressive control perspectives.

The methodology of implementation of the control ramp is widely used as the

Received: 19 July 2014 / Accepted: 20 September 2014

© 2014 CMSIM



ISSN 2241-0503

compensation tool for the irregularities of the current loop, ensuring stable P1 operation of SPC. In general, the introduction of this compensating signal shifts the border of the first period-doubling bifurcation, estranging the appearance of subharmonic oscillations that are usually avoided. However, the same ramp also modifies the structure of the parameter space even after the period-doubling bifurcation, defining noticeable changes in the dynamics of the system. This research is dedicated to exploration of different mechanisms of chaotization and further aftereffects in the operation of SPC, defined by the implementation of mentioned compensation technique.

It has been demonstrated during several last decades, that the conventional models and methodologies used to predict the appearance of subharmonic oscillations in switching power converters are generally oversimplified and not capable of providing reliable data in many cases [3]-[6]. This fact determined the development of great number of scientific researches dedicated to possible improvements of already existing models and to the introduction of new promising approaches. Recently one innovative methodology – method of complete bifurcation groups (MCBG) [7]-[9] – has been applied to investigation of rare phenomena and chaos in SPC, allowing the detection and detailed analysis of previously unobserved operating regimes. MCBG is utilized within current research in order to provide the most complete analysis of the observed non-linear phenomena in the dynamics of SPC.

The structure of the paper is as follows. The second section presents the simplified discrete-time model of the boost SPC, introducing the compensating ramp in the current control loop. The results of the complete bifurcation analysis, including the construction of bifurcation map and various bifurcation diagrams, are presented and discussed in section 3. The concluding remarks and comments are given in the last section.

2. The Model of Boost Converter with Compensation Ramp

The SPC under study is widely used boost converter with peak current mode control, exhibiting unstable dynamics as the duty cycle exceeds 0.5 [3]. The main methodology of extending the region of stable P1 operation in this kind of devices is the introduction of compensation ramp signal, which is also included in the dynamical model.

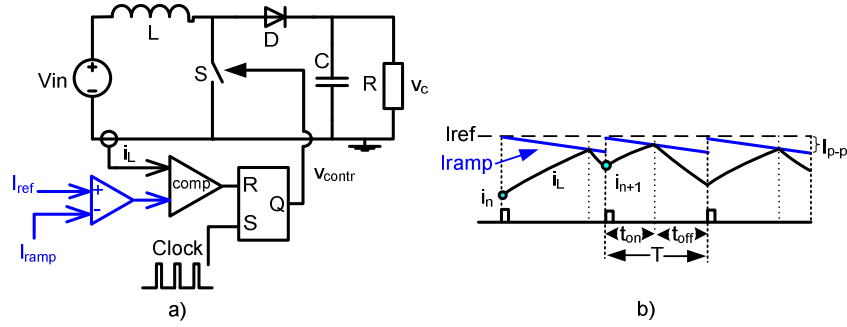


Fig. 1. (a) The simplified model of current - mode controlled boost converter; (b) waveforms of inductor current and compensation ramp.

The simplified model of boost SPC is shown in Fig. 1. The operation of converter is as follows: the switch is turned *ON* as the clock pulse arrives and turned *OFF* as the value of inductor current reaches the compensation ramp. The dynamics of this energy conversion circuit could be described by two systems of difference equations, depending on the sequence of switching events. If the clock pulse arrives before the inductor current reaches the I_{ramp} , the obtained discrete time model is the following:

$$\begin{aligned} v_{n+1} &= v_n e^{-T/(RC)} \\ i_{n+1} &= i_n + V_{in} T L. \end{aligned} \quad (1)$$

If the inductor current reaches I_{ramp} before the arrival of the next clock pulse the map would include the *ON* and *OFF* intervals:

$$\begin{aligned} v_{n+1} &= e^{-mt_{off}} [K_1 \cos(\mu t_{off}) + K_2 \sin(\mu t_{off})] + V_{in} \\ i_{n+1} &= e^{-mt_{off}} [C[-m(K_1 \cos(\mu t_{off}) + K_2 \sin(\mu t_{off})) + \\ &+ \mu(-K_1 \sin(\mu t_{off}) + K_2 \cos(\mu t_{off}))] + (K_1 \cos(\mu t_{off}) \\ &+ K_2 \sin(\mu t_{off})) / R] + V_{in} / R, \end{aligned} \quad (2)$$

where

$$\begin{aligned} t_{on} &= (I_{ref} - i_n) / (V_{in} / L + S_c); K_1 = v_n e^{-2mt_{on}} - V_{in}; \\ t_{off} &= T - t_{on}; K_2 = [I_{ref} / C - (v_n e^{-2mt_{on}} + V_{in})] / \mu; \\ m &= 1 / (2RC); p = 1 / \sqrt{LC}; \mu = \sqrt{p^2 - m^2}; S_c = I_{p-p} / T. \end{aligned} \quad (3)$$

The borderline I_{border} defines the case, when the clock pulse arrives exactly at the time instance the inductor current reaches the control signal:

$$I_{border} = I_{ref} - T(V_{in} / L + S_c). \quad (4)$$

It has been shown that this discrete-time model could be efficiently applied to the study of nonlinear dynamics and estimation of stability boundaries of main period-1 and subharmonic modes of operation [8].

The provided model (1)-(4) is used in the process of the construction of bifurcation map, complete bifurcation diagrams, calculating parameters of different periodic regimes as well as estimating their stability.

The values of main parameters of boost converter under test are as follows: $R=40$ (Ω); $L=1.5$ (mH); $C=5$ (μF); $T=100$ (μS); $V_{in}=5$ (V); $I_{ref}=[0.2\dots 0.9]$ (A); $S_c=[0\dots 2000]$ (A/s).

3. Results of the complete bifurcation analysis

As it has been mentioned in the introduction, the analysis of the global dynamics of boost SPC will be provided by means of one of the most progressive techniques – method of complete bifurcation groups. This methodology has proved to be very useful during the complete analysis of nonlinear phenomena, observed in various classes of smooth as well as non-smooth dynamical systems [7]-[9].

The complete bifurcation analysis of the boost converter begins with the construction of bifurcation map, selecting reference current and compensation ramp as primary and secondary bifurcation parameters (see Fig. 2). As the mechanisms of chaotization are of special interest and the P1 orbits are not involved in the rapid transitions to chaotic modes of operation, the range of parameters defining stable P1 regime is disregarded in the constructed bifurcation map. As it could be seen from Fig. 2 for $S_c=0$ the classical period doubling route to chaos should be observed. As the value of compensation ramp is increased other subharmonic operation regimes (as well as periodic windows) just after the P2 appear, defining the formation and structure of chaotic regions.

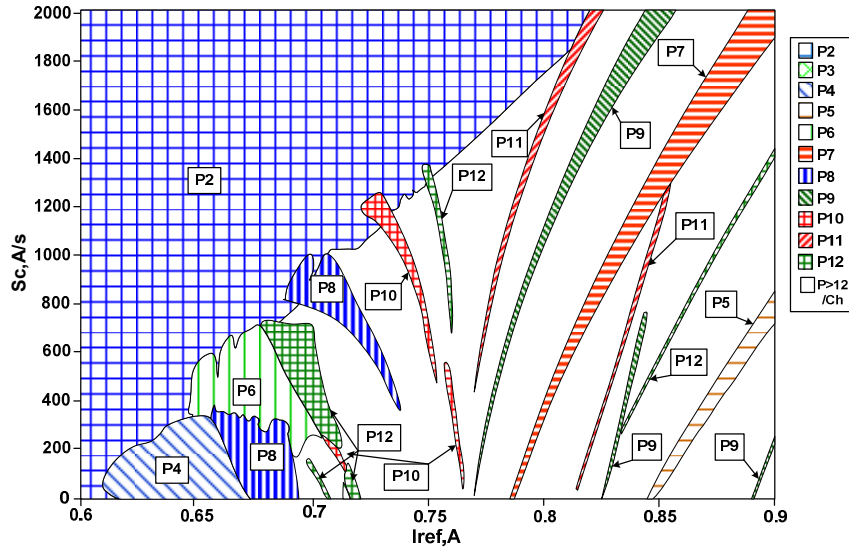


Fig.2. The bifurcation map of the boost converter.

This map will be referred to during the analysis of complete bifurcation diagrams, constructed as the horizontal cross-sections of Fig. 2.

It should be understood, that in this case the complete bifurcation diagrams are 3-dimensional graphs, depicting the sampled inductor current and capacitor voltage on two axes and the bifurcation parameter on the third one. For the clearness of analysis only the projection of this graph to the plane defined by the inductor current and the bifurcation parameter (I_{ref}) will be observed, as only in this plane the collisions with the border defined by (4) could be precisely detected and interpreted.

In order to analyze the influence of the incrementing compensation ramp on the chaotization of the system, first let's examine the complete bifurcation diagram for the boost converter without the compensation.

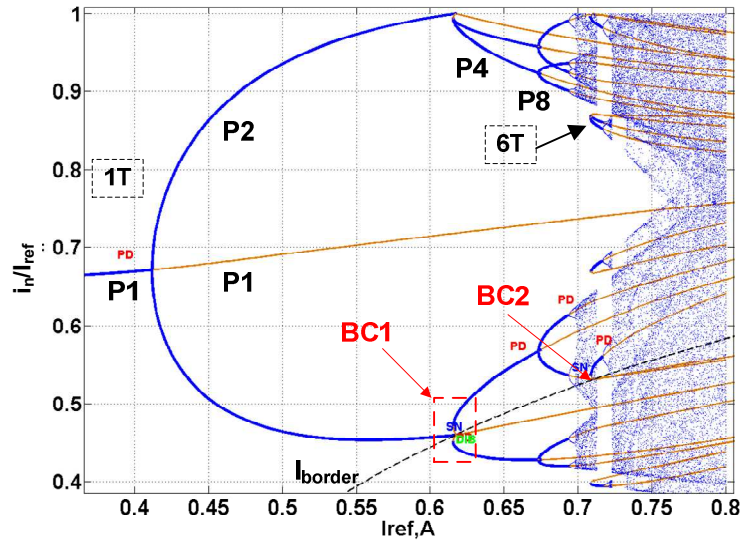


Fig. 3. The complete bifurcation diagram for $S_c=0$ (A/s).

The bifurcation diagram, depicting stable (dark lines) and unstable (light-colored lines) periodic regimes, as well as chaotic regions (shaded area), is shown in the Fig. 3. It could be seen, that for small values of reference current, the system operates in the stable P1 regime and moves to P2 mode through classical period doubling bifurcation. Further increment of I_{ref} leads to the development of non-smooth phenomena, when stable or unstable orbits collide with the I_{border} (dashed line), leading to non-smooth transition from P2 to P4 regimes (see point BC1), as well as change of shape of unstable branch of 6T bifurcation group (see point BC2). Thus it could be concluded, that for the selected set of system parameters, collisions with the border have slightly changed the topology of bifurcation diagram, without any noticeable rapid jumps between different modes of operation.

The second bifurcation diagram, constructed for $S_c=200$ (A/s) is shown in the Fig. 4. One of the most interesting features of the observed diagram is the presence of rather uncommon phenomena that will be referred as “cutting border collision” (CBC). It is well known, that the collision with borders in hybrid systems could lead to the appearance of non-smooth bifurcations, when the multipliers do not smoothly cross the unit circle, indicating the widely observed period-doubling or saddle-node bifurcations, but rather “jump” over the border of unit circle, depicting the rapid change in the stability of definite regime under investigation. In the mentioned case the periodic regime still continues to exist, but its stability suddenly changes. However the CBC leads to the “disappearance” of all stable as well as unstable periodic regimes that cross the defined borderline.

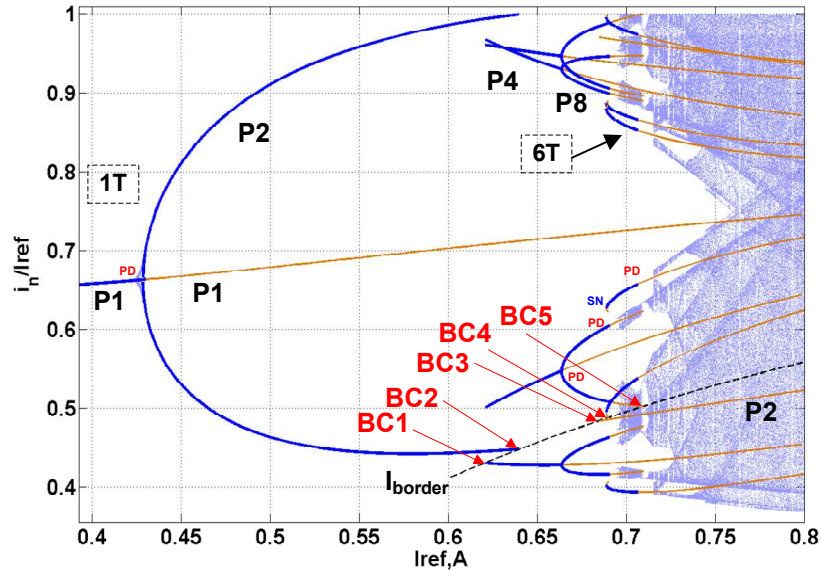


Fig. 4. The complete bifurcation diagram for $S_c=200$ (A/s).

This phenomenon could be observed, in example, in points BC1, BC2 and BC4 in the Fig. 4, where stable P2, P4 and unstable P8 regimes collide with the borderline defined in (4) and disappear without any signs of bifurcations. The route to chaos in this case is formed by rather uncommon period-doublings, leading to the infinite number of unstable periodic orbits and chaotic mode of operation.

It has been shown in the Fig. 3, that for $S_c=0$ (A/s) the border collision of 6T bifurcation group leads to some changes in the shape of bifurcation diagram. However the diagram in the Fig. 4 demonstrates that the same collision for $S_c=200$ (A/s) causes the disappearance of unstable branch of 6T bifurcation group, preserving the stable branch, leading to the development of independent chaotic regime.

It is interesting to note that the P2 orbit appears at point BC3 as unstable regime and continues to exist for larger values of I_{ref} . So it could be assumed that in the interval $I_{ref}=[0.64...0.68]$ (A) this regime slides along the borderline (4). Other orbits after the CBC are not observed within the parameter range of interest.

As the transition from P2 to P4 in the Fig.4 is caused by highly non-smooth event, it would be interesting to investigate the topology of basins of attraction of coexisting P2 and P4 modes of operation for $I_{ref}=0.63$ (A).

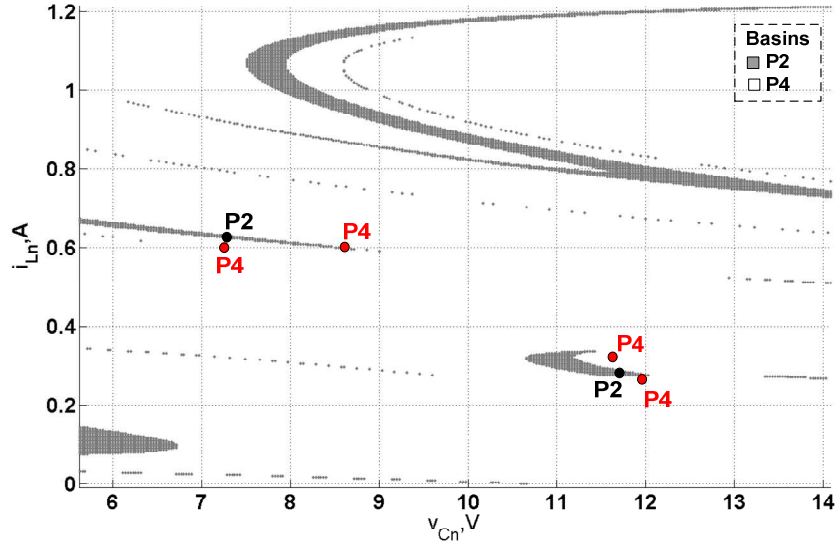


Fig. 5. Basins of attraction of P2 and P4 regimes for $S_c=200$ (A/s) and $I_{ref}=0.63$ (A) with corresponding attractors.

As it could be seen from Fig. 5, despite the border collisions observed in the complete bifurcation diagrams, the basins of attraction of P2 and P4 regimes, forming rather complex structure, still remain smooth and no sign of uncommon topological peculiarities are observed.

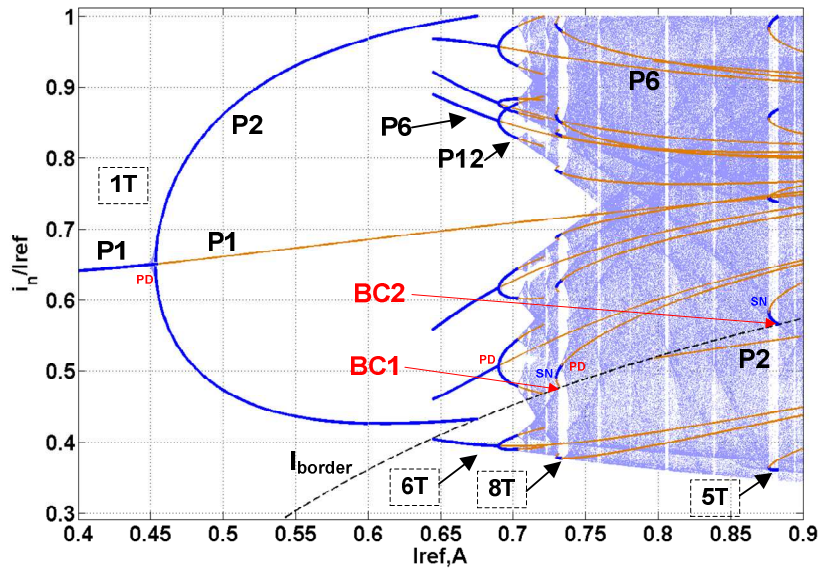


Fig. 6. The complete bifurcation diagram for $S_c=500$ (A/s).

Further increment of the compensation ramp practically leads to the enlargement of stable P1 region and essentially changes the sequence and types of bifurcations. Fig. 6 depicts the complete bifurcation diagram of the boost converter for $S_c=500$, showing that the first period doubling at $I_{ref}=0.45$ is followed by rapid transition from P2 to P6 operating regime with definite region of coexistence of both mentioned orbits. Further chaotization is governed by unstable orbits arising from the P6 regime through classical period-doublings. Points BC1 and BC2 in the Fig. 6 demonstrate to possible interactions of periodic orbits, appearing from saddle-node bifurcations with the borderline (4). At point BC1 the cutting border collision eliminates only the unstable regime of 8T bifurcation group, allowing the gradual development of chaotic attractor. However at point BC2 the stable branch of 5T bifurcation group collides with the borderline and rapid chaotification is observed without the development of sequent period-doubling cascade.

The bifurcation map, shown in the Fig. 2, allows asserting that further increasing the value of S_c leads to the implementation of direct P2-P6, P2-P8, P2-P10 etc. transitions as well as the development of increasingly wider periodic windows, excluding the possibility of existence of practically useful robust chaotic modes of operation.

4. Conclusions

The results of complete bifurcation analysis allow revealing some interesting changes in chaotification scenario of the compensated boost switching power converter. For the converters with small output capacitance and without compensating ramp (i.e. $S_c=0$) the classical smooth period doubling route to chaos could be observed. As the value of the compensating ramp signal is increased the non-smooth effects, emerging from the interaction of bifurcation branches of stable and unstable periodic regimes with the borderline (4), take place, determining the general appearance of bifurcation diagram and transition to chaotic mode of operation.

It should be noted that, taking into account the topology of complete bifurcation diagrams constructed within this research, the definition of bifurcation group in MCBG (see e.g. [7]) should be revised, as the P2 and P4 regimes in the Fig. 4, corresponding to the same 1T bifurcation group have no common bifurcation points and are not mutually connected with stable or unstable branches.

Acknowledgements

This research was funded by a grant (No. 467/2012) from the Latvian Council of Science.

References

1. M. Qin and J. Xu. Multiduty ratio modulation technique for switching DC-DC converters operating in discontinuous conduction mode. *IEEE Trans. Ind. Electron.*, vol. 57, no. 10, 3497-3507, 2010.
2. J.H.B. Deane and D.C. Hamill. Improvement of power supply EMC by chaos. *Electron. Lett.*, vol. 32, no. 12, 1045-1049, 1996.

3. S. Banerjee and G. C. Verghese (Ed.) . *Nonlinear Phenomena in Power Electronics . Attractors, Bifurcations, Chaos, and Nonlinear Control*, IEEE Press, 2001.
4. M. di Bernardo, C.J. Budd, A.R. Champneys, P. Kowalczyk. *Piecewise-Smooth Dynamical Systems: Theory and Application*, Springer –Verlag, Berlin, 2008.
5. M. di Bernadro , E. Fosas, G. Olivar, F. Vasca. Secondary bifurcations and high-periodic orbits in the voltage controlled buck converter. *International Journal of Bifurcation and Chaos*, vol.12, no.7, 2755-2771, 1997.
6. D.C. Hammil, J.H.B. Deane, D.J. Jefferies. Modeling of chaotic dc/dc converters by iterative nonlinear mappings. *IEEE Transactions on Circuits and Systems Part I*, vol.35, no.8, 25-36, 1992.
7. M. Zakrzhevsky. New Concepts of Nonlinear Dynamics: Complete Bifurcation Groups, Protuberances, Unstable Periodic Infinitiums and Rare Attractors. *Journal of Vibroengineering*, vol.10, iss.4, 421-441, 2008.
8. D. Pikulins. Subharmonic oscillations and chaos in dc-dc switching converters. *Electronics and Electrical Engineering, Kaunas: Technologija*, 4: 33-36, 2013.
9. D. Pikulins. Effects of Non-Smooth Phenomena on the Dynamics of DC-DC Converters. *Scientific Journal of RTU: 4 series*, 29: 119-122, 2011.

A vision of the Brownian motion models useful in random systems analysis

Gabriel V. Orman and Irinel Radomir

Department of Mathematics and Computer Science, "Transilvania" University of
Braşov, 500091 Braşov, Romania.
(E-mail: ogabriel@unitbv.ro)

Abstract. There are many cases when we refer to *chaos* and *chaotic and complex systems* to describe the comportment of some natural phenomena. In this context, we shall discuss, in this paper, some aspects which appear in the study of various systems. Firstly, we shall refer to the *Brownian transition probabilities* in connection with the conditions assumed on the transition probabilities; and then the *standard Brownian motion* is considered in connection with the "passage times" which are the most important Markov times.

Keywords: stochastic differential equations, stochastic calculus, Markov processes, Markov property, Brownian motion..

1 Introduction

Starting from the observation that many a time we refer to *chaos* and *chaotic and complex systems* to describe the comportment of some natural phenomena, it is very useful, from a mathematical point of view, to talk about a passing from *chaotic and complex systems* to *Brownian motion*. In this way we can refer to the *Brownian motion* which is a more realistic model of such phenomena.

Its fascinating properties and its far-reaching extension of the simplest normal limit theorems to functional limit distributions acted, and continue to act, as a catalyst in random systems analysis. As some authors remarks too, the Brownian motion reflects a perfection that seems closer to a law of nature than to a human invention.

In Physics, the ceaseless and extremely erratic dance of microscopic particles suspended in a liquid or gas, is called *Brownian motion*. It was systematically investigated by Robert Brown (1828, 1829), an English botanist, from movement of grains of pollen in water to a drop of water in oil. He was not the first to mention this phenomenon and had many predecessors but Brown's investigation brought it to the attention of the scientific community.

Brownian motion was frequently explained as due to the fact that particles were alive. It is only in 1905 that kinetic molecular theory led Einstein to



the first mathematical model of Brownian motion. He began by deriving its possible existence and then only learned that it had been observed.

A completely different origin of mathematical Brownian motion is a game theoretic model for fluctuations of stock prices due to L. Bachelier from 1900. In his doctoral thesis, *Théorie de la spéculation*, Ann. Sci. École Norm. Sup., 17, 1900, 21-86, he hinted that it could apply to physical Brownian motion. Therein, and in his subsequent works, he used the heat equation and, proceeding by analogy with *heat propagation* he found, albeit formally, distributions of various functionals of mathematical Brownian motion. Heat equations and related parabolic type equations were used rigorously by Kolmogorov, Petrovsky, Khintchine.

But Bachelier was unable to obtain a clear picture of the Brownian motion and his ideas were unappreciated at the time. This because a precise definition of the Brownian motion involves a measure on the path space, and it was not until 1908-1909 when É. Borel published his classical memoir on Bernoulli trials: *Les probabilités dénombrables et leurs applications arithmétique*, Rend. Circ. Math. Palermo 27, 247-271, 1909. But as soon as the ideas of Borel, Lebesgue and Daniell appeared, it was possible to put the Brownian motion on a firm mathematical foundation. And this was achieved in 1923 by N. Wiener, in his work: *Differential space*, J. Math. Phys. 2, 131-174, 1923.

Many researchers were fascinated by the great beauty of the theory of Brownian motion and many results have been obtained in the last decades. As for example, among other things, in *Diffusion processes and their sample paths* by K. Itô and H.P. McKean, Jr., in *Theory and applications of stochastic differential equations* by Z. Schuss, or in *Stochastic approximation* by M.T. Wasan as in *Stochastic calculus and its applications to some problems in finance* by J.M. Steele.

In fact, the construction of the Brownian motion as a limit of a rescaled random walk can be generalized to a class of Markov chains. In this context, at the 4th CMSIM international Conference, we discussed some aspects relating to the approximation in the study of Markov processes and Brownian motion; also, we referred to the Markov property from a perspective of K. Itô.

Itô's integral and other details and related topics in stochastic calculus and applications in random systems analysis are developed among other by B. Øksendal and A. Sulem, J.M. Steele, P. Malliavin, P. Protter, D.W. Stroock.

2 In short about transition probabilities

In some previous papers we have discussed on Markov processes in a vision of K. Itô and we have emphasized the aspects regarding to the Markov property. In this context a fundamental concept is that of *transition probabilities* which will be considered, in short, below.

Let S be a *state space* and consider a particle which moves in S . Also, suppose that the particle starting at x at the present moment will move into the set $A \subset S$ with probability $p_t(x, A)$ after t units of time, "irrespectively of its past motion", that is to say, this motion is considered to have a *Markovian character*.

The *transition probabilities* of this motion are $\{p_t(x, A)\}_{t,x,A}$ and is considered that the time parameter $t \in T = [0, +\infty)$.

The state space S is assumed to be a *compact Hausdorff space with a countable open base*, so that it is homeomorphic with a compact separable metric space by the Urysohn's metrization theorem. The σ -field generated by the open space (the topological σ -field on S) is denoted by $K(S)$. Therefore, a *Borel set* is a set in $K(S)$.

It will be assumed that the transition probabilities $\{p_t(x, A)\}_{t \in T, x \in S, A \in K(S)}$ satisfy the following conditions:

- (1) for t and A fixed,
 - a) the transition probabilities are Borel measurable in x ;
 - b) $p_t(x, A)$ is a probability measure in A ;
- (2) $p_0(x, A) = \delta_x(A)$ (i.e. the δ -measure concentrated at x);
- (3) $p_t(x, \cdot) \xrightarrow{weak} p_t(x_0, \cdot)$ as $x \rightarrow x_0$ for any t fixed, that is

$$\lim_{x \rightarrow x_0} \int f(y)p_t(x, dy) = \int f(y)p_t(x_0, dy)$$

for all continuous functions f on S ;

- (4) $p_t(x, U(x)) \rightarrow 1$ as $t \searrow 0$, for any neighborhood $U(x)$ of x ;
- (5) the Chapman-Kolmogorov equation holds:

$$p_{s+t}(x, A) = \int_S p_t(x, dy)p_s(y, A).$$

It is interesting to observe that, if we define,

$$p_t(x, dy) = \frac{1}{t\sqrt{2\pi}} e^{-\frac{(y-x)^2}{2t^2}} dy \quad \text{in } R$$

$$p_t(\infty, A) = \delta_\infty A.$$

then, the conditions (1) – (5) above are satisfied for *Brownian transition probabilities*.

Let now consider $C = C(S)$ to be the space of all continuous functions (it is a separable Banach space with the supremum norm). Then, the *transition operators* can be defined in a similar manner.

Definition 21 *The operators p_t , defined by*

$$(p_t f)(x) = \int_S p_t(x, dy)f(y), \quad f \in C$$

are called "transition operators".

And the conditions for the transition probabilities can be adapted to the transition operators.

Now the Markov process can be defined as follows

Definition 22 A Markov process is a system of stochastic processes

$$\{X_t(\omega), t \in T, \omega \in (\Omega, K, P_a)\}_{a \in S},$$

that is for each $a \in S$, $\{X_t\}_{t \in S}$ is a stochastic process defined on the probability space (Ω, K, P_a) .

The transition probabilities of a Markov process will be denoted by $\{p(t, a, B)\}$. Now let us denote by $\{H_t\}$ the transition semigroup and let R_α be the resolvent operator of $\{H_t\}$.

The next results shows that $p(t, a, B)$, H_t and R_α can be expressed in terms of the process as follows:

Theorem 21 Let f be a function in $C(S)$. Then

1. $p(t, a, B) = P_a(X_t \in B)$.
2. For $E_a(\cdot) = \int_\Omega \cdot P_a(d\omega)$ one has $H_t f(a) = E_a(f(X_t))$.
3. $R_\alpha f(a) = E_a\left(\int_0^\infty e^{-\alpha t} f(X_t) dt\right)$.

Proof. One can observe that 1. and 2. follow immediately.

To prove 3., we will use the following equality:

$$R_\alpha f(a) = \int_0^\infty e^{-\alpha t} H_t f(a) dt = \int_0^\infty e^{-\alpha t} E_a(f(H_t)) dt.$$

Since $f(X_t(\omega))$ is right continuous in t for ω fixed, and measurable in ω for t fixed, it is therefore measurable in the pair (t, ω) . Thus, we can use Fubini's theorem and therefore we obtain

$$R_\alpha f(a) = E_a\left(\int_0^\infty e^{-\alpha t} f(X_t) dt\right),$$

which proves 3.

3 Elements of stochastic differential equations

To describe the motion of a particle driven by a *white noise* type of force (due to the collision with the smaller molecules of the fluid) the Langevin equation

$$\frac{d\nu(t)}{dt} = -\beta\nu(t) + \mathbf{f}(t) \tag{1}$$

is used, where $\mathbf{f}(t)$ is the white noise term. Its solution is the following

$$y(t) = y_0 e^{-\beta t} + e^{-\beta t} \int_0^t e^{\beta s} \mathbf{f}(s) ds. \tag{2}$$

If we denote by $\mathbf{w}(t)$ the Brownian motion, then it is given by

$$\mathbf{w}(t) = \frac{1}{q} \int_0^t \mathbf{f}(s) ds, \tag{3}$$

so that $\mathbf{f}(s) = \frac{q d\mathbf{w}(s)}{ds}$. But $\mathbf{w}(t)$ is nowhere differentiable, such that $\mathbf{f}(s)$ is not a function. Therefore, the solution (2), of Langevin's equation, is not a well-defined function. This difficulty can be overcome, in the simple case, as follows. Integrating (2) by parts, and using (3), it results

$$y(t) = y_0 e^{-\beta t} + q\mathbf{w}(t) - \beta q \int_0^t e^{-\beta(t-s)} \mathbf{w}(s) ds. \quad (4)$$

But all functions in (4) are well defined and continuous, such that the solution (3) can be interpreted by giving it the meaning of (4). Now, such a procedure can be generalized in the following way. Let us given two functions $f(t)$ and $g(t)$ that are considered to be defined for $a \leq t \leq b$. For any partition $P : a \leq t_0 < t_1 < \dots < t_n$, we denote

$$S_P = \sum_{i=1}^n f(\xi_i)[g(t_i) - g(t_{i-1})],$$

where $t_{i-1} \leq \xi_i \leq t_i$. If a limit exists

$$\lim_{|P| \rightarrow 0} S_P = I$$

where $|P| = \max_{1 \leq i \leq n} (t_i - t_{i-1})$, then it is said that I is the *Stieltjes integral* of $f(t)$ with respect to $g(t)$. It is denoted

$$I = \int_a^b f(t) dg(t).$$

Now the stochastic differential equation

$$\begin{aligned} dx(t) &= a(x(t), t)dt + b(x(t), t)dw(t) \\ x(0) &= x_0 \end{aligned} \quad (5)$$

is defined by the Itô integral equation

$$x(t) = x_0 + \int_0^t a(x(s), s)ds + \int_0^t b(x(s), s)dw(s). \quad (6)$$

The simplest example of a stochastic differential equation is the following equation

$$\begin{aligned} dx(t) &= a(t)dt + b(t)dw(t) \\ x(0) &= x_0 \end{aligned} \quad (7)$$

which has the solution

$$x(t) = x_0 + \int_0^t a(s)ds + \int_0^t b(s)dw(s).$$

The *transition probability density* of $x(t)$ is a function $p(x, s; y, t)$ satisfying the condition

$$P(x(t) \in A | x(s) = x) = \int_A p(x, s; y, t) dy$$

for $t > s$ where A is any set in R . It is supposed that $a(t)$ and $b(t)$ are deterministic functions. The stochastic integral

$$\chi(t) = \int_0^t b(s) dw(s)$$

is a limit of linear combinations of independent normal variables

$$\sum_i b(t_i)[w(t_{i+1}) - w(t_i)].$$

Thus, the integral is also a normal variable. But, then

$$\chi(t) = x(t) - x_0 - \int_0^t a(s) ds$$

is a normal variable, and therefore

$$p(x, s; y, t) = \frac{1}{\sqrt{2\pi\sigma}} e^{-\frac{(y-m)^2}{2\sigma}}$$

where

$$m = E(x(t) | x(s) = x).$$

Now

$$E(x(t) | x(s) = x) = x + \int_s^t a(u) du$$

is the expectation of the stochastic integral vanishes.

The variance is given by the relation

$$\sigma = Var x(t) = E \left[\int_s^t b(u) dw(u) \right]^2 = \int_s^t b^2(u) du.$$

Thus, $p(x, s; y, t)$ is given by the following equation

$$p(x, s; y, t) = \left[2\pi \int_s^t b^2(u) du \right]^{-\frac{1}{2}} \cdot e^{-\frac{\left(y - x - \int_s^t a(u) du \right)^2}{2 \int_s^t b^2(u) du}}.$$

For proofs and other aspects see [3], [8], [13], [23], [20].

4 From chaotic motion to Brownian motion

In our days the Brownian motion is of ever increasing importance not only in Probability theory but also in classical analysis and its applications.

Frequently, Brownian motion was explained as due to the fact that particles were alive. Today we know that this motion is due to the bombardment of the particles by the molecules of the medium. In a liquid, under normal conditions, the order of magnitude of the number of these impacts is of 1020 per second.

Let us imagine a chaotic motion of a particle of colloidal size immersed in a fluid. Such a chaotic motion of a particle is called, usually, *Brownian motion* and the particle which performs such a motion is referred to as a *Brownian particle*. Such a chaotic perpetual motion of a Brownian particle is the result of the collisions of particle with the molecules of the fluid in which there is.

But this particle is much bigger and also heavier than the molecules of the fluid which it collide, and then each collision has a negligible effect, while the superposition of many small interactions will produce an observable effect.

On the other hand, for a Brownian particle such molecular collisions appear in a very rapid succession, their number being enormous. For a so high frequency, evidently, the small changes in the particle's path, caused by each single impact, are too fine to be observable. For this reason the exact path of the particle can be described only by statistical methods.

Thus, the influence of the fluid on the motion of a Brownian particle can be described by the combination of two forces in the following way:

1. The considered particle is much larger than the particle of the fluid so that the cumulated effect of the interaction between the Brownian particle and the fluid may be taken as having a hydrodynamical character. Thus, the first of the forces acting on the Brownian particle may be considered to be the forces of *dynamical friction*. It is known that the frictional force exerted by the fluid on a small sphere immersed in it is determined from the Stokes's law: *the drag force per unit mass acting on a spherical particle of radius a is given by $-\beta\mathbf{v}$, with $\beta = \frac{6\pi a\eta}{m}$* , where m is the mass of the particle, η is the coefficient of dynamical viscosity of the fluid, and \mathbf{v} is the velocity of particle.

2. The other force acting on the Brownian particle is caused by the individual collisions with the particles of the fluid in which there is. This force produces instantaneous changes in the acceleration of the particle. Furthermore, this force is *random both in direction and in magnitude*, and one can say that it is a *fluctuating force*. It will be denoted by $\mathbf{f}(\mathbf{t})$. For $\mathbf{f}(\mathbf{t})$ the following assumptions are made:

- a) The function $\mathbf{f}(\mathbf{t})$ is statistically independent of $\mathbf{v}(t)$.
- b) $\mathbf{f}(\mathbf{t})$ has variations much more frequent than the variations in $\mathbf{v}(t)$.
- c) $\mathbf{f}(\mathbf{t})$ has the average equal to zero.

In these conditions, the Newton's equations of motion are given by the following stochastic differential equation

$$\frac{d\mathbf{b}f\mathbf{v}(t)}{dt} = -\beta\mathbf{v}(t) + \mathbf{f}(t) \quad (8)$$

which is called the *Langevin's equation*.

From the Langevin's equation, the statistical properties of the function $\mathbf{f}(t)$ can be obtained if its solution will be in correspondence with known physical laws. One can observe that the solution of (8) determines the *transition probability density* (in brief *the transition density*) $\rho(\mathbf{v}, t, \mathbf{v}_0)$ of the random process $\mathbf{v}(t)$, which verifies the equation

$$P(\mathbf{v}(t) \in A | \mathbf{v}(0) = \mathbf{v}_0) = \int_A \rho(\mathbf{v}, t, \mathbf{v}_0) d\mathbf{v}. \tag{9}$$

We do not insist on these aspects, our purpose has been to introduce the concept of transition density.

Now following K. Itô ([7], [5]) we shall refer shortly to the *k-dimensional Brownian motion* and emphasize some of its results.

But, firstly, we shall remind some aspects regarding to the *3-dimensional Brownian motion* discussed at the 6th CMSIM international Conference.

It is not difficult to observe that a definition of a *Markov process* as in Definition 22 not correspond to many processes that are of a real interest. For this reason it is useful to obtain an extension of this notion (such an extended notion has been proposed by K. Itô).

Let E be a separable Banach space with real coefficients and norm $\|\cdot\|$ and let also $L(E, E)$ be the space of all bounded linear operators $E \rightarrow E$. It can be observed that $L(E, E)$ is a linear space.

Definition 41 *The collection of stochastic processes*

$$X = \{X_t(\omega) \equiv \omega(t) \in S, t \in T, \omega \in (\Omega, K, P_a)\}_{a \in S}$$

is called a "Markov process" if the following conditions are satisfied:

- 1) the "state space" S is a complete separable metric space and $K(S)$ is a topological σ -algebra on S ;
- 2) the "time internal" $T = [0, \infty)$;
- 3) the "space of paths" Ω is the space of all right continuous functions $T \rightarrow S$ and K is the σ -algebra $K[X_t : t \in T]$ on Ω ;
- 4) the probability law of the path starting at a , $P_a(H)$, is a probability measure on (Ω, K) for every $a \in S$ which satisfy the following conditions:
 - 4a) $P_a(H)$ is $K(S)$ -measurable in a for every $H \in K$;
 - 4b) $P_a(X_0 = a) = 1$;
 - 4c) $P_a(X_{t_1} \in E_1, \dots, X_{t_n} \in E_n) = \int \dots \int_{a_i \in E_i} P_a(X_{t_1} \in da_1) P_{a_1}(X_{t_2-t_1} \in da_2) \dots \dots P_{a_{n-1}}(X_{t_n-t_{n-1}} \in da_n)$ for $0 < t_1 < t_2 < \dots < t_n$.

According to Definition 41, X will be referred as a *Markov process in the generalized sense*.

Now let X be a Markov process in a generalized sense and let us denote by $\mathbf{B}(S)$ the space of all bounded real $K(S)$ -measurable functions. Also let us consider a function $f \in \mathbf{B}(S)$.

It is supposed that

$$E_a \left(\int_0^\infty |f(X_t)| dt \right) \tag{10}$$

is bounded in a . Therefore

$$Uf(a) = E_a \left(\int_0^\infty f(X_t) dt \right) \tag{11}$$

is well-defined and is a bounded $K(S)$ -measurable function of $a \in S$.

The Uf is called *the potential* of f with respect to X . Having in view that $Uf = \lim_{\alpha \downarrow 0} R_\alpha f$, it is reasonable to write R_0 instead of U . Based on this fact, $R_\alpha f$ will be called *the potential of order α of f* .

Remark 1. It is useful to retain that $R_\alpha f \in \mathbf{B}(S)$ for $\alpha > 0$; and generally $f \in \mathbf{B}(S)$ while $R_0 f (= Uf) \in \mathbf{B}(S)$ under the condition (10).

Now the name *potential* is justified by the following theorem on *the 3-dimensional Brownian motion*

Theorem 41 *Let X be the 3-dimensional Brownian motion. If $f \in \mathbf{B}(S)$ has compact support, then f satisfies (10) and*

$$Uf(a) = \frac{1}{2\pi} \int_{R^3} \frac{f(b) db}{|b - a|} = \frac{1}{2\pi} \times \text{Newtonian potential of } f. \tag{12}$$

Let us denote by D a bounded domain in $R^n, n \geq 1$.

Definition 42 *A function g is called "harmonic" in D if g is C^∞ in D and if $\Delta g = 0$ (where C^∞ is the class of functions differentiable infinitely many times.).*

Now let f be a continuous function defined on the boundary ∂D and let us denote by X a k -dimensional Brownian motion defined as follows

Definition 43 *The k -dimensional Brownian motion is defined on $S = R^k$ by the equality*

$$p_t(a, db) = (2\pi t)^{-\frac{k}{2}} e^{-\frac{|b-a|^2}{2t}} db = N_t(b - a) db,$$

where $|b - a|$ is the norm of $b - a$ in R^k .

Given a k -dimensional Brownian motion X , if there exists a solution g for the Dirichlet problem (D, f) , then

$$g(a) = E_a(f(X_\lambda)), \tag{13}$$

The Dirichlet problem D, f is to find a continuous function $g = g_{D,f}$ on the closure $\bar{D} \equiv D \cup \partial D$ such that g is harmonic in D and $g = f \circ g \partial D$.

where $\lambda \equiv \lambda_D = \text{exit time from } D$ (that is to say $\lambda_D = \inf\{t > 0 : X_t \notin D\}$, the hitting time of D^C).

In this context an interesting result is given in the following theorem

Theorem 42 *If D is a bounded domain and g is a solution of the Dirichlet problem (D, f) , then*

$$g(a) = E_a(f(X_\lambda))$$

where $a \in D$ and $\lambda = \lambda_D$.

On the other hand, the Dirichlet problem (D, f) has a solution if ∂D is smooth as it is proved in the following theorem

Theorem 43 *If ∂D is smooth, then*

$$g(a) = E_a(f(X_\lambda)),$$

where $\lambda = \lambda_D = \text{exit time from } D$, is the solution of the Dirichlet problem (D, f) .

Note 41 *The expression " ∂D is smooth" means that ∂D has a unic tangent plane at each point x of ∂D and the outward unit normal of the tangent plane at x moves continuously with x .*

Remark 2. Many other details regarding to the topics just discussed, proofs and some related problems can be found in [7], [6], [1], [5], [25], [15], [23], [14], [20], [18].

Conclusion 41 *The Brownian motion can be represented as a random sum of integrals of orthogonal functions. Such a representation satisfies the theoretician's need to prove the existence of a process with the four defining properties of Brownian motion, but it also serves more concrete demands, one of the most important being the "chaotic and complex systems analysis".*

Especially, the series representation can be used to derive almost all of the most important analytical properties of Brownian motion.

It can also give a powerful numerical method for generating the Brownian motion paths that are required in computer simulation.

References

- 1.A.T. Bharucha-Reid. Elements Of The Theory Of Markov Processes And Their Applications. Dover Publications, Inc., Mineola, New York, 1997.
- 2.W. Feller. An Introduction to Probability Theory and its Applications, vol. I, II. John Wiley & Sons, Inc., New York, London, 1960.
- 3.I.I. Gihman and A.V. Skorohod. Stochastic Differential Equations. Springer-Verlag, Berlin, 1972.
- 4.B.V. Gnedenko. The Theory of Probability. Mir Publisher, Moscow, 1976.
- 5.K. Itô. Selected Papers. Springer, 1987.
- 6.K. Itô and H.P. McKean Jr. Diffusion Processes and their Sample Paths. Springer-Verlag, Berlin Heidelberg, 1996.

- 7.K. Itô. Stochastic Processes. Eds. Ole E. Barndorff-Nielsen and Ken-iti Sato. Springer, 2004.
- 8.Kloeden, P. and Platen, E., Numerical Solution of Stochastic Differential Equations. Springer-Verlag, 1992.
- 9.H.J. Kushner and G.G Yin. Stochastic Approximation Algorithms and Applications. Springer-Verlag New York, Inc., 1997.
- 10.M. Loève. Probability theory I. Springer-Verlag, New York, Heidelberg Berlin, 1977.
- 11.M. Loève. Probability theory II. Springer-Verlag, New York, Heidelberg Berlin, 1978.
- 12.P. Malliavin. Integration and Probability. Springer-Verlag New York, Inc., 1995.
- 13.B. Øksendal. Stochastic Differential Equations: An Introduction with Applications. Sixth Edition. Springer-Verlag, 2003.
- 14.B. Øksendal and A. Sulem. Applied Stochastic Control of Jump Diffusions. Springer, 2007.
- 15.P. Olofsson and M. Andersson. Probability, Statistics and Stochastic Processes, 2nd Edition. John Wiley & Sons, Inc., Publication, 2012.
- 16.G.V. Orman. Lectures on *Stochastic Approximation Methods and Related Topics*. Preprint. "Gerhard Mercator" University, Duisburg, Germany, 2001.
- 17.G.V. Orman. Handbook of Limit Theorems and Stochastic Approximation. "Transilvania" University Press, Brasov, 2003.
- 18.G.V. Orman. On Markov Processes: A Survey of the Transition Probabilities and Markov Property. In C. H. Skiadas and I. Dimotikalis, editors, *Chaotic Systems: Theory and Applications*, World Scientific Publishing Co Pte Ltd., 224-232, 2010.
- 19.G.V. Orman. On a problem of approximation of Markov chains by a solution of a stochastic differential equation. In: C.H. Skiadas, I. Dimotikalis and C. Skiadas, editors, *Chaos Theory: Modeling, Simulation and Applications*, World Scientific Publishing Co Pte Ltd., 30-40, 2011.
- 20.G.V. Orman. Aspects of convergence and approximation in random systems analysis. LAP Lambert Academic Publishing, 2012.
- 21.G. V. Orman. *Probability and Stochastic Processes for Chaotic and Complex Systems Analysis* (to appear).
- 22.P. Protter. Stochastic Integration and Differential Equations: a New Approach. Springer-Verlag, 1990.
- 23.Z. Schuss. Theory and Application of Stochastic Differential Equations. John Wiley & Sons, New York, 1980.
- 24.J.M. Steele. Stochastic calculus and financial applications. Springer-Verlag New York, Inc. 2001.
- 25.D.W. Stroock. Markov Processes from K. Itô Perspective. Princeton Univ. Press, Princeton, 2003.
- 26.M.T. Wasan. Stochastic Approximation. Cambridge University Press, 1969.

Study of the Rate-and-State Equation Solutions for Different Critical Stresses by Grassberger-Procaccia Method

S. Turuntaev^{1,2,3}, A. Kamay^{1,2}

¹Moscow Institute of Physics and Technology (State University), 141700, Institutsky per., d.9, Dolgoprudny, Moscow District, Russia

²All-Russian Research Institute of Automatics, 127055, Sushevskaya, d.22, Moscow, Russia

³Institute of Geosphere Dynamics of Russian Academy of Sciences (IDG RAS), 119334, Leninsky prosp., d.38, k.1, Moscow, Russia

(E-mail: s.turuntaev@gmail.com, alesia.kamay@gmail.com)

Abstract: A problem of seismicity variation due to human action is considered. The widely used “stick-slip” model of the seismic regime with “rate-and-state” friction law was adopted for description of a sliding along tectonic faults. The main distinctions of used approach from the common one (Hobbs [7], Erickson et al. [4]) are the followings: we consider two-parameter friction law and vary the value of critical shear stress in the rate-and-state equation in suggestion that this is the value which can be varied by human impact (by mining, fluid injection and production, hydraulic fracturing and so on). Calculations were done for the critical stress varied from 5MPa up to 50 MPa with increment 5 MPa. For each value of the critical stress, the time series of the displacement along the fault, its rate and change of shear stress were calculated. Obtained time series were analyzed with the help of Grassberger-Procaccia method of correlation integral calculation for different embedding space dimensions. It was found that if the critical stress increases, the system behavior changes significantly. Oscillations of the fault sliding become inharmonic, and when the critical stress reaches 45 MPa, the oscillations become quasi-chaotic. An estimation of the obtained attractor dimensions by Grassberger-Procaccia method showed, that an increase of the critical stresses τ^* results in increase of the attractor correlation dimensionality C^* : $\tau^*=5\text{MPa } C^*=1.4$; $\tau^*=15\text{MPa } C^*=1.6$; $\tau^* = 30 \text{ MPa } C^*=2.2$; $\tau^*=45\text{MPa } C^*=2.5$. It was found, that if the critical stress continue to increase, the correlation dimension would stop to increase. A comparison of the obtained results with real induced seismicity data analysis showed that in real case the correlation dimensionality is higher. This discrepancy can be explained by taking into account the presence of the seismic events, which are not related with human influence and which can be considered as a stochastic background. An addition of random component with signal/noise ratio 2 to the model data resulted in increase of the model correlation dimensionality to 4-5, which is in good correspondence with induced seismicity data.

Received: 30 July 2014 / Accepted: 19 October 2014

© 2014 CMSIM



ISSN 2241-0503

Keywords: Rate-and-state Equation, Two-parameter Friction Law, Grassberger and Procaccia Method, Correlation Integral, Seismic Regime, Induced Seismicity.

1 Introduction

Despite the fact that rate-and-state model of friction was proposed in the second half of the previous century, the interest to it has increased in recent years. The reason for that is a success in physics of nonlinear phenomena, in particular, in the area of chaotic system analysis. The rate-and-state model was adopted as quite appropriate basis for describing seismic processes in the Earth crust and for modeling relevant geophysical systems. Currently, it is believed that this model describes the seismic process most adequately.

In 60s, Brace and Byerlee [1] proposed to consider unstable frictional sliding along tectonic faults as a model of earthquakes. The model included a suggestion that a cohesion existing in some parts of the fault prevents free slipping along it and leads to an accumulation of shear stress to a critical level, after which the slip and the earthquake occur.

Peculiarities of the friction forces dependence on the duration of the stationary state of the contact and on the speed of the motion along the fault was examined by Dieterich [3]. Gu et al. [6] experimentally investigated various modes of the frictional movements and determined empirical constants which values are used in many modern variants of the rate-and-state equation.

The origin of the unstable sliding and its dynamics were studied by Ohnaka et al. [8]. The work was focused on the study of mechanism of the transition to instability.

The rate-and-state equation was considered by Hobbs [7] by means of nonlinear dynamics methods. Change of friction was studied as a function of displacement and velocity at a variation of the stiffness coefficient in the rate-and-state equation. The similar approach was implemented by Erickson et al. [4], they examined an appearance of chaotic solutions in the one-parameter velocity-dependent friction equation.

Turuntaev et al. [9] showed that the man-made impact on underground leads to an increase in the “regularity” of the seismic regime. To explain the increase in the seismic regime regularity, a model of fault motion defined by the two-parameter velocity dependent friction law was considered.

In the presented paper, we consider two-parameter type of the friction law and vary the value of critical shear stress in the rate-and-state equation in suggestion that this is the value varied by human impact (by mining, fluid injection and production, hydraulic fracturing and so on). The obtained solutions of the rate-and-state equation are analyzed by means of Grassberger-Procaccia method [5].

2 The model description

Abstracting from internal structure and genesis of the faults, it can be expected that the fault sliding will be governed by the friction law of one type or another,

and that change of the sliding state due to anthropogenic impacts will be resulted in the growth of regularity of the seismic process.

Measurements of the tectonic fault motions show that the motions look like a combination of slow sliding (so-called creep) and fast moves, which accompanied by tremors (earthquakes). This type of the motion can be described with the help of the model proposed by Burridge & Knopov [2], which looks like a system of blocks, elastically connected with each other (Fig. 1 - top view and Fig. 2 - general view of the model). Each block moves under net action of elastic forces from adjacent blocks and frictional force from the stationary substrate. To simplify the model it can be assumed that all the blocks have the same mass, the same area of contact with the surface and that elastic links between the blocks have the same modulus.

Let's consider the rate-and-state motion equation with the two-parameter friction law and let's assume that the man-made impact of any nature reduces the critical shear stress (for example, by increasing the pore pressure by fluid injection or by action of vibrations, etc.).

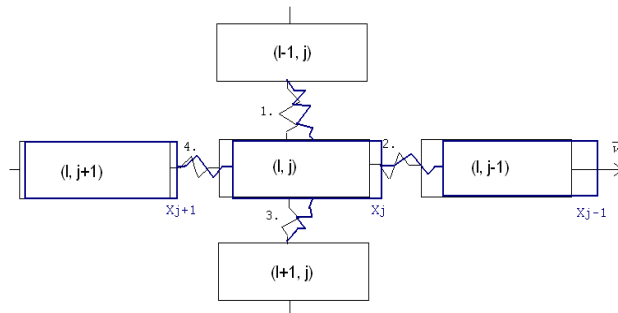


Fig. 1. The model of tectonic blocks (top view).

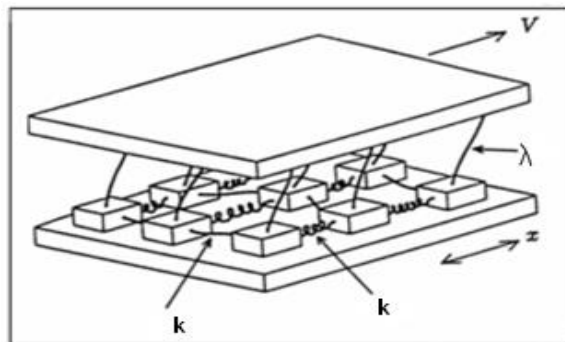


Fig. 2. The Burridge - Knopov (B- K) model of active tectonic faults (general view).

The motion equation for the single-chain of the blocks can be written as follows:

$$m\ddot{x}_j = k(v_0 t - x_{j-1} + 2x_j - x_{j+1}) - \tau_j s \quad (1)$$

where the first term defines the elastic forces from adjacent blocks, the second one is the fault friction: k – stiffness of the elastic links between blocks, v_0 – speed at infinity, τ – shear stress occurs as a result of friction. In this paper we consider the two-parameter friction law in the form proposed by Hobbs [7]:

$$\tau = \tau^* + A \ln\left(\frac{v}{v^*}\right) + \theta_1 + \theta_2 \quad (2)$$

where v^* – constant velocity of the crustal block relative motion, τ^* – critical stress, which can be changed by external influences and can be written as

$$\tau^* = C + \mu(\sigma - p) \quad (3)$$

where C – cohesion coefficient, μ – coefficient of friction, p – pore pressure, σ – normal stress; θ_i – state variable, which characterizes the state of the sliding surfaces, and which evolution over time is determined by the equation:

$$\dot{\theta}_i = -\frac{v}{L_i} \left[\theta_i + B_i \ln\left(\frac{v}{v^*}\right) \right] \quad (4)$$

here L_i – characteristic dimensions of the roughness of sliding surfaces, $i = \overline{1, 2}$. Values of the constants v^* , A , B_i , τ^* , L_i were taken from experiments of Gu et al. [6].

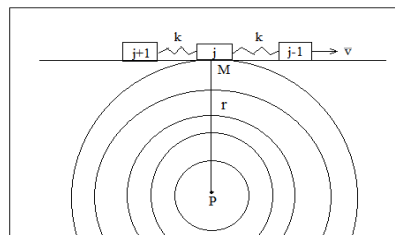


Fig.3. Changes of critical stress on the j -th block boundary at the point M due to change of pore pressure at the point P.

Figure 3 illustrates the way in which one of the parameters of equation (3) can be changed. Let's suppose that the pressure is increased at a point P. At some moment t_{cr} the pressure will change at the point M. It follows from (3) that the increase in the pore pressure will reduce the critical stress $\tau^*(t_{cr}) < \tau^*(0)$, and

consequently, it will reduce the value of the frictional force at which the j -th block begins to move.

According to the motion equation (1), it can cause the block “jump”, and as a result, the redistribution of elastic forces in the links between the blocks. The whole system can come into motion in the result of a change even in one of the parameters. The resulting motion is complex. Turuntaev et al. [9] showed that to analyze such motions, it's reasonable to use the methods developed for the analysis of nonlinear dynamic systems.

3 Results

Numerical simulation of the block motions was carried out under the critical stress τ^* varied from 5 MPa to 50 MPa with increments 5 MPa. For each value of τ^* , time series of the block displacements, its velocity and shear stress at the block base were calculated. Complexity of the obtained time series were analyzed using algorithm for estimating the correlation dimension, based on the calculation of the correlation integral by Grassberger and Procaccia method [5]. Finite-difference scheme used to solve the equation of motion (1) was following

$$\frac{x_{i+1} - 2 \cdot x_i + x_{i-1}}{h^2} = \frac{k}{m} \cdot \left(\frac{x_i - x_{i-1}}{h} \cdot (ih) - x_i \right) - \frac{\tau_i}{s} \quad (5)$$

with initial conditions $x(0) = 0, v(0) = 0$.

The values of the parameters k, m, s were taken from Hobbs [7].

To solve the equation we used the method of direct and reverse run with the following values of the preliminary factors

$$\begin{aligned} A &= a(y_{i-1,j}, y_{i,j}) \cdot \frac{h}{h_x^2} \\ B &= a(y_{i,j}, y_{i+1,j}) \cdot \frac{h}{h_x^2} \\ C &= \left(a(y_{i-1,j}, y_{i,j}) + a(y_{i,j}, y_{i+1,j}) \right) \cdot \frac{h}{h_x^2} + 1 \\ F &= y_{i,j} \end{aligned} \quad (6)$$

which were included in the calculation of the coefficients α_i, β_i in final formulas

$$\alpha_i = \frac{B}{C - A \cdot \alpha_{i-1}}$$

$$\beta_i = \frac{A \cdot \beta_{i-1} + F}{C - A \cdot \alpha_{i-1}} \tag{7}$$

$$y_{i,j} = \alpha_i \cdot y_{i+1,j+1} + \beta_i$$

The values of the time step h , spatial grid h_x and the correction coefficients of approximation in the formulas (5) - (7) were the followings:

$$\begin{aligned} h_x &= 0.01 \\ h &= 0.01 \\ \delta &= 0.01 \\ \alpha &= 0.5 \cdot \gamma \cdot \delta^2 \cdot y_{i-1,j}^{y-1} + y_{i,j}^{y-1} \end{aligned} \tag{8}$$

The selected values of the coefficients give approximation error at the level of $O(h, h_x^2)$, that is enough accuracy for the considered problem.

The graphs of the displacements and the shear stresses for three values of the critical stress τ^* : 5 MPa, 20 MPa, 50 MPa are shown in Figures 4-6.

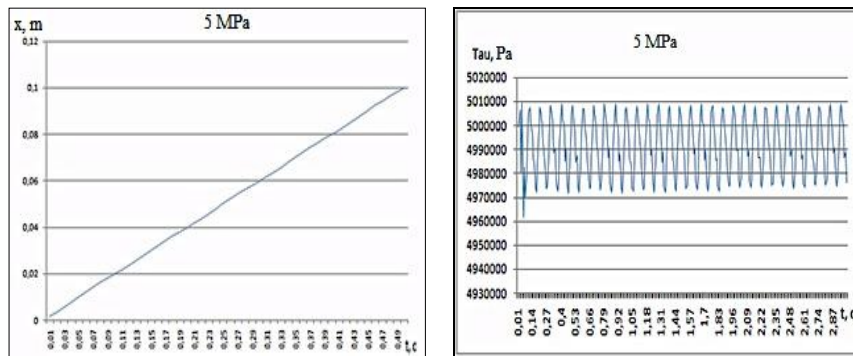


Fig. 4. Dependencies of displacement on time (left panel) and shear stress on time (right panel) at the critical stress equal to 5 MPa.

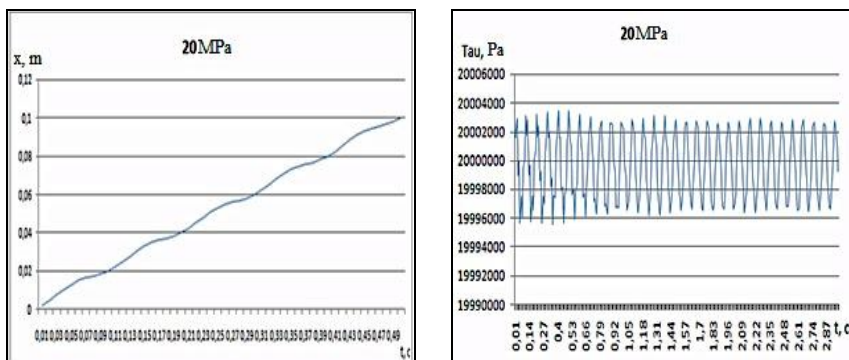


Fig. 5. Dependencies of displacement on time (left panel) and shear stress on time (right panel) at the critical stress equal to 20 MPa.

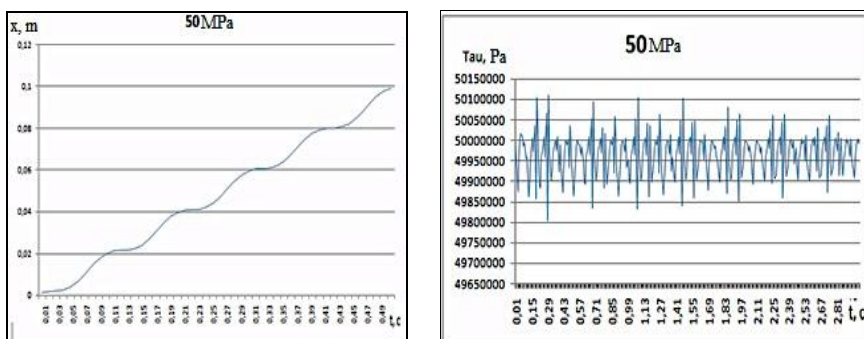


Fig. 6. Dependencies of displacement on time (left panel) and shear stress on time (right panel) at the critical stress equal to 50 MPa.

The graphs of the block motion respectively to motion with constant velocity at infinity v^* are shown in Fig. 7.

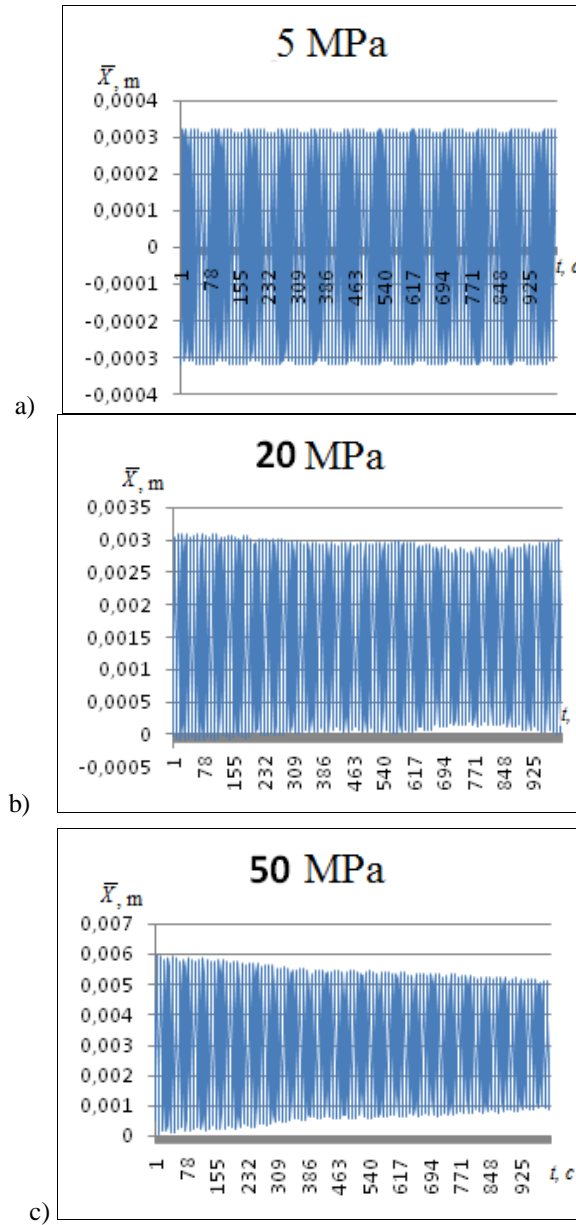


Fig . 7. Dependencies of displacements on time, calculated for the critical values of $\tau^* = 5 \text{ MPa}$, $\tau^* = 20 \text{ MPa}$, and $\tau^* = 50 \text{ MPa}$.

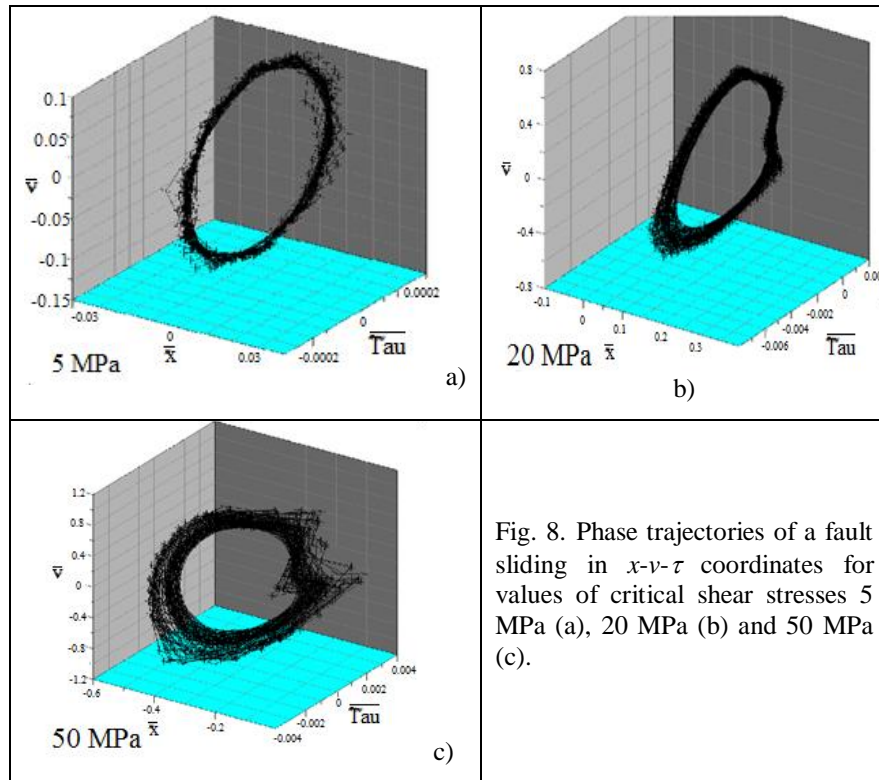


Fig. 8. Phase trajectories of a fault sliding in x - v - τ coordinates for values of critical shear stresses 5 MPa (a), 20 MPa (b) and 50 MPa (c).

Results of the numerical calculations for several values of the critical stresses are shown in Figure 8 as phase trajectories in x - v - τ coordinates. The values are normalized to the characteristic size $L_1, v^* \text{ и } \tau^* = 5 \text{ МПа}$ for the values of the critical stress at 5 MPa, 20 MPa and 50 MPa (Fig. 8a, 8b and 8c, respectively). An estimation of the obtained attractor dimensions by Grassberger-Procaccia method showed, that an increase of the critical stresses results in increase of the attractor correlation dimensionality: $\tau^*=5\text{MPa } C^*=1.4$; $\tau^*=15\text{MPa } C^*=1.6$; $\tau^* = 30 \text{ MPa } C^*=2.2$; $\tau^*=45\text{MPa } C^*=2.5$. (Figure 9).

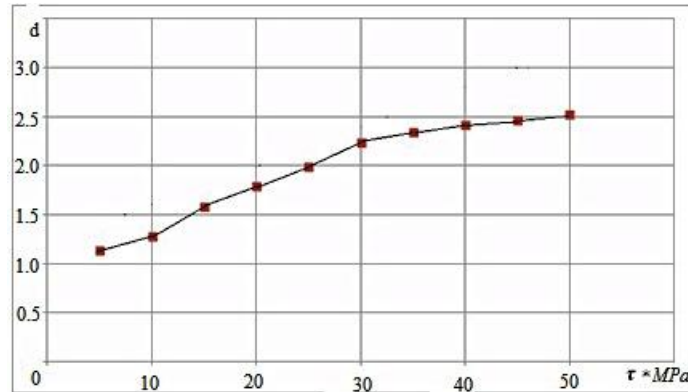


Fig. 9. The dependence of the correlation dimension on the critical stress.

4 Discussion and conclusions

Numerical analysis of the rate-and-state equation with the two-parameter friction law showed significant changes in the stick-slip motion when the critical shear stress varied.

Evaluation of the correlation dimension and the embedding space dimension by Grasberger - Procaccia method for obtained time series has shown that both of these variables have small values. Change of critical stress from 5 MPa to 50 MPa resulted in variation of correlation dimension and embedded space dimension from 1.1 to 2.5 and from 3 to 5, respectively.

In the range of the critical stress from 5 MPa to 30 MPa the correlation dimension increases linearly with critical stress increase; at higher values of the critical stress there is a tendency of saturation of the correlation dimension dependence on the critical stress.

Values of dimensions obtained in the numerical modeling may differ from the values, which were obtained in the analysis of real seismicity (for example, in the area of the Bishkek geodynamic test site, see Turuntaev et al. [9]). We can assume that this difference is caused by significantly higher complexity of real seismic processes in comparison with the model one. This distinguish can be explained by taking into account the presence of the seismic events, which are not related with human influence and which can be considered as a stochastic background. An addition of random component with signal/noise ratio 2 to the model data resulted in increase of the model correlation dimensionality to 4-5, which is in good correspondence with induced seismicity data.

The existence of stable states in the equation solution allows us to specify the problem of seismic activity forecast and of seismic regime control technologies. According to the equation (3), the influence on the movement of the crustal blocks can be performed by changing coefficient of friction by fluid injection. The aim of further research is to study the minimal values of the pore pressure

variations that can change the state of a system of interconnected blocks. We plan to investigate the solutions of the equations of motion (1) with more real parameters than obtained in laboratory experiments (the characteristic parameters of the contacting surfaces, the velocity of relative motion of the fault, stiffness, cohesion, etc.).

At the present stage of the research one can conclude that an increase of the critical stresses in the rate-and-state equation results in increase of the attractor correlation dimensionality: C^* : $\tau^*=5\text{MPa}$ $C^*=1.4$; $\tau^*=15\text{MPa}$ $C^*=1.6$; $\tau^* = 30\text{MPa}$ $C^*=2.2$; $\tau^*=45\text{MPa}$ $C^*=2.5$. It was found, that if the critical stress continue to increase, the correlation dimension would stop to increase.

References

1. Brace W.F., Byerlee J.D. Stick-slip as mechanism for earthquakes. *Science*. 1966. V. 153. № 3739. P. 990-992.
2. Burridge R., Knopov L. Model and theoretical seismicity//Bull. Seism. Soc. Amer. 1967. V. 67. P.341-371.
3. Dieterich J.H. Earthquake nucleation on faults with rate and state-dependent friction. *Tectonophysics*. 1992. V. 211. P. 115-134.
4. Erickson B., Birnir B., Lavalle D. A model for aperiodicity in earthquakes. *Nonlinear Processes in Geophysics*. 2008.
5. Grassberger P., Procaccia I. Measuring the strangeness of strange attractors. *Physica. North-Holland Publishing Company*. 1983. V. 9D. P. 189-208.
6. Gu J. C., Rice J.R., Ruina A.L., Tse S.T. Slip motion and instability of a single degree of freedom elastic system with rate-and-state dependent friction. *J. Mech. Phys. Solids*. 1984. V. 32. P. 167-196.
7. Hobbs B.E. Chaotic behavior of frictional shear instabilities. *Rockbursts and Seismicity in Mines / Fairhurst (ed.)*. 1990. Balkema, Rotterdam. P. 87-91.
8. Ohnaka, M., Kuwahara, Y., Yamamoto, K. and Hirasawa, T. In: Dynamic breakdown processes and the generating mechanism for high-frequency elastic radiation during stick-slip instabilities. American Geophysical Union, Washington D.C., 37: 4. 1986. doi: 10.1029/GM037p0013.
9. Turuntaev S.B., Vorohobina S.V., Melchaeva O.Y. Identification of anthropogenic changes of seismic regime using methods of nonlinear dynamics. *Physics of the Earth*. 2012. № 3. P. 52-65.

Acoustic decoding of a sheep bell and trotters within a sheep herd

V J Law^{1,2}

¹Surface Engineering Group, School of Mechanical and Materials Engineering, University College Dublin, Belfield, Dublin 4, Ireland

²Plasma Technology Laboratory, Department Chemical Engineering, University of Patras, Rio, Greece.

*(e-mail: viclaw66@gmail.com)

Abstract: *Time series analysis is used to de-convolve bell and trotter signals within a herd of sheep for the purpose of identifying the sheep's activity: walking to and from grazing pasture and stock pens. A bimodal model of the standing-wave quarter wavelength closed air-column mode is found to represent the frequency response (1-8 kHz) the elliptical shape and composite design of the iron bell that is commonly attached around the sheep neck.*

Keywords: sheep bells, acoustic recoding, time series, overtones and walking gait.

1. Introduction

For centuries percussion instruments in the form of iron bells have been placed around the neck of sheep (also cattle and goats) to let herders know what's going on with the herd while they are doing other things. Indeed to improve awareness of the shepherds to the herd's activity, the loudest bell is placed on the more active bucks. The tranquil melodic bell ring while sheep are grazing has been used to locate herds on pasture, as well as letting the shepherds know that 'all is well'. In contrast the more rapid and louder ring tones have proven to be a good indicator of nearby predators. To the shepherd who has been brought-up to identify these two extremes, the acoustic signatures are easily identified, however it may be argued that the identifying conditions between these two extremes is much more difficult, and for the average person who is not involved in shepherding.

Time series analysis of a series values sampled of regular intervals has been shown to be a power tool in de-convolving complex noise sources such as: turbulent fluid [1], complex information with industrial plants chemical [2], and White Dwarf stars [3]. This paper reports upon the use of time series analysis and mathematical modelling of the acoustic response of iron bells that are attached to three sheep within a healthy herd containing between 27 to 30 healthy adult male and female 'Sfakia' sheep. The aim of this work is to establish if the bell acoustics can be used to identify the sheep's walking gait as



they move steadily between pastures, rather than the extreme scenarios of grazing and threat of predators. To prevent imparted stress and ‘sheep worrying’ to a single sheep the acoustic measurements were performed at a distance of 20 m from the herd. The measurements were made in the month of October on the outskirts of the Cretan village of Kástelos in Western Crete. The time of the measurements are both in the morning (8-9 am local time) when the sheep are moved down-hill to pastures and in the evening when they are moved back up-hill to the safety of their stock pens in the evening (6-7 pm). The two groups of acoustics measurements characterises the mood and movement of the sheep: in the morning the sheep are fresh from their rest and are herded down-hill with a slope of 10 degrees and average speed of $2.4 \pm 0.2 \text{ m.s}^{-1}$, whereas in the evening the sheep are tired and herded up-hill at an average speed of $1.2 \pm 0.2 \text{ m.s}^{-1}$. The measurement is made over seven consecutive days. It is found that speeds are in good agreement with the kinetic characteristic of the walking gate of a sheep as measured on a pressure sensing walking way [4].

In the case of the bell, when the clapper is struck against the rim, the metal-on-metal impact imparts energy instantaneously as sound travels through metal at approximately 5130 m.s^{-1} into the bell. At this moment a temporary distortion (hum) of the rim occurs from the where the energy is transmitted throughout the bells to produce a continuous succession of partials resonate tones. It is this time dependent combination of strike tone and partials which gives rise to the timbre [5] of the bell. However and unlike tuned cast metal hand-bells and church-bells, the sheep bell’s elliptical shape and composite design imparts boundaries on the transmission of energy throughout the body of the bell due to the stiffness at the two welded acute angles on the major axis and the less stiff regions on the minor axis. In addition the sheep bells perceived timbre also depends on whether the struck region of the rim is damped by the sheep’s neck. Thus the mechanical interaction within a sheep bell’s timbre is potentially more complex, in both pitch and amplitude, when compared to a tuned cast bell.

2. Experiment

2.1 Sheep bell

The sheep bell studied here is of the composite elliptical open-bell design that is made from two formed iron metal sheet (1 mm thick) that are brazed/welded together to form the elliptical shaped aperture behind which a closed air-column acoustic chamber is formed. The edge dimensions of the aperture are typically 11.5 cm between the welded seams and 16 cm from the rim to the bell node. The clapper is made from 4 mm diameter x 10 cm in length.

Finally the bell’s nodal point (minimum vibration point) is attached to the sheep using a leather strap. A photograph of a sheep bell is shown in Fig 1a and a schematic of the aperture of the bell are shown in Fig 1 b.

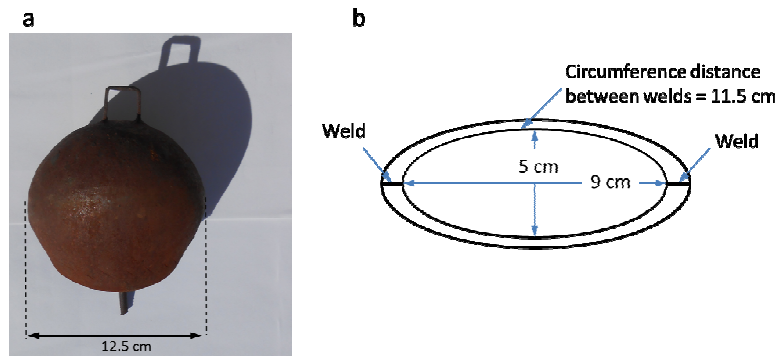


Figure 1a and b: a) photograph of flat side of sheep bell, b) Schematic view of open aperture of sheep bell.

2.1 Acoustic recording

The sound recording and deconvolution analysis used in this study is performed by National instrument LabVIEW 2011 software program running on a Dell laptop. This software has been published elsewhere [6- 10]. The recordings were made using an Omi-directional condenser microphone and sampled at rate of 24000 samples per second with a 24 Bit depth for a period of 1 second. In all cases the measurements were made at a distance of 20 m from the noise source (bell and sheep herd). In order to identify the sheep bells minor and major axis response, a single bell was isolated and freely suspended and the clapper struck using the force of a human hand. The frequency response of a normal healthy human hearing frequency range is defined between 20 Hz to 20 kHz, but is most sensitive in the 1 to 4 kHz range [5]. Therefore it the 20 Hz to 8 kHz range is only considered here. The bell recordings along with a recording of the surrounding acoustic environment (baseline) are used as sound references for subsequent decoding of the sheep traveling upon the road. To standardize the reference measurements with the sheep acoustic recordings a piece-by-piece Savitzky-Golay (SG) [11] moving window of 10 Hz is used smooth the amplitude of the time series data. This digital conditioning of the recordings match the same conditioning process to remove the high frequency sound of the sheep's feet impacting on the concrete road surface.

3. Results

Three sets of 10 bell recordings were made. These sets are reported in sections: 3.1 for a single bell removed from sheep neck and struck by a human hand, 3.2 bells attached to 3 sheep within the herd as the sheep are walking up-hill (evening), and 3.3 as the sheep are herded down-hill in the morning. In all three cases the recording microphone is placed 20 m perpendicular to the direction of the herd movement.

3.1. Sheep bell response (freely suspended)

Figure 2 shows a triplet of reference acoustic spectra for the freely suspended sheep bell. The top spectrum is associated with the clapper striking the bell on the major axis, the middle spectra is associated with the clapper striking on the minor axis and lower spectrum is a measurement of the surrounding area without any strikes (baseline) and is only shown for comparative purpose here.

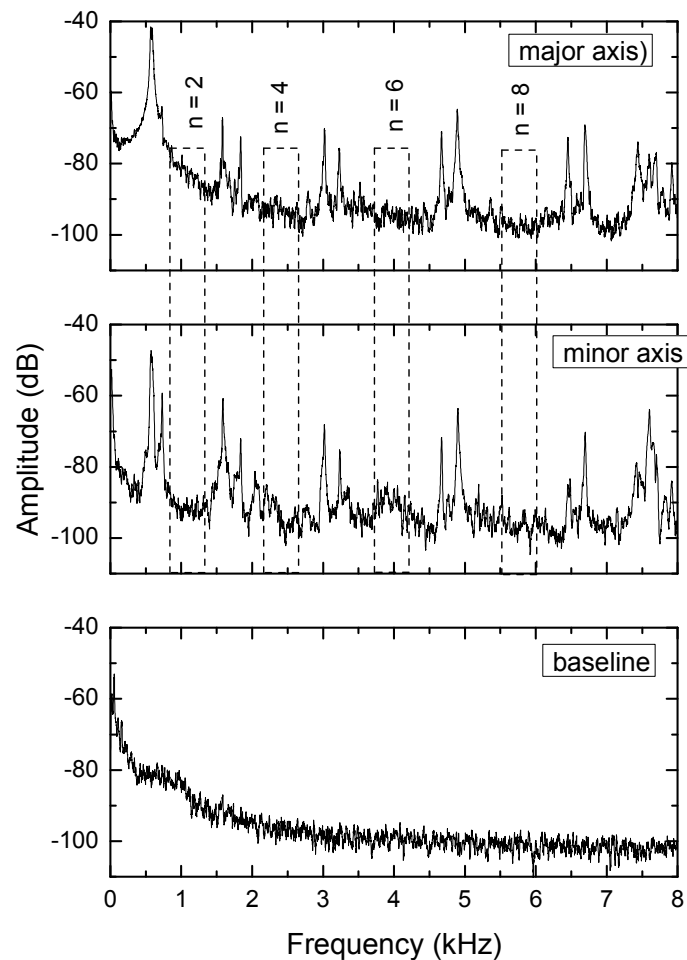


Figure 2: Frequency response of sheep bell as struck on the major, minor axis using a human hand and baseline measurement.

Upon comparison of the spectra's, there a number of features of note: Firstly the strike tone is seen to be formed from doublet peak with frequencies of 600 Hz 740 Hz which is followed by harmonic related overtones/partial that exhibit doublets also. The overtones/partial frequencies in the major axis

spectra appear to have a strong odd harmonic relationship to the strike tone. For example $n = 3, 5, 7, 9$, whereas both even overtones/partial frequencies ($n = 2, 4, 6, 8$ etc.) and odd overtones appear in the minor axis spectra. The disparity that appearance the between odd and odd plus even overtones leads the minor axis spectra having a richer timbre which may be expressed by the normalised mean amplitude (centred around ± 200 Hz) of the even overtones/partials to the strike tone amplitude as denoted using the standard notation of loss to the carrier (dBc), see the annotated dashed box for $n = 2, 4, 6$ and 8 in figure 2 and measured mean values in table 1. In table 1 it can be seen that the loss to the strike tone (carrier) for $n = 4, 6, 8$ is greater for the major axis typically 52.6 dB as compared to typically 41.6 dB for the minor axis. The lost however at $n = 2$ is reversed but only by 3 dB.

Table 1. Strike tone amplitude and dBc values centred (± 200 kHz) around even overtones/partials for both major and minor axis.

Axis	Strike tone (dB)	n = 2 (dBc)	N = 4 (dBc)	n = 6 (dBc)	n = 8 (dBc)
Major axis	-41	-44	-50	-52	-56
Minor axis	-47	-48	-43	-37	-45

To a first approximation (predict single rather doublets), the strike tone frequency (f_o) and the odd overtone/partials frequencies (f_n) may be represented mathematically using a single standing-wave quarter wavelength closed air-column model [5-9] as shown Equation (1).

$$f_n \approx \frac{nc}{4L} \tag{1}$$

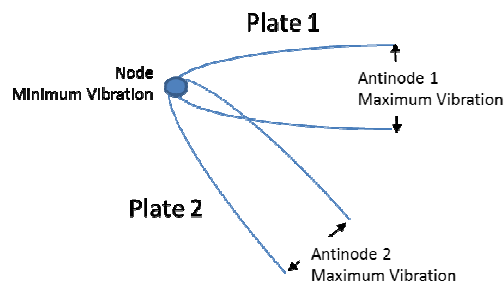
In equation (1), n is modulo frequency number, L is the physical length of resonator and c is the sound velocity at 20 °C (air: $\sim 346 \text{ m.s}^{-1}$; iron: $\sim 5130 \text{ m.s}^{-1}$). For a closed air-column, the bell aperture defines the antinode (maximum pressure vibration) and the node point defines the minimum vibration point. Thus using equation (1), the bells 600-800 Hz strike tones equates to $L = 11.4$ to 11.8 cm. Using the bell's geometric information proved in figure 1 the computed value of L approximates to the bell's major axis and either side of the apertures surface length which would suggest the twin peaks in the strike tone originate from the aperture volume and the metal rim, Given this configuration, odd overtones/partials are readily supported and even overtones/partials are suppressed. To predict both even and odd overtones/partials resonances equation 1 needs to be modified by replacing the 4 the denominator with 2 thus making equation 1 to represent a half wavelength resonator.

The physical constriction of the welded iron bell leads the proposition of a double standing-wave quarter wavelength closed air-column model as shown in

Equation (2) and (3). In these two equations the single (') and double (") represents the first and second frequency within the doublet frequency of the bell and also the length of the first and second plates of the bell.

$$f_n' \approx \frac{nc}{4L'} \quad (2)$$

$$f_n'' \approx \frac{nc}{4L''} \quad (3)$$



Schematic of the doublet bell model

3.2. Sheep bell response as the herd is moving up-hill

Figure 3 shows a representative acoustic frequency spectrum of the 10 recordings of 3 similar bells (with a major axis of 10 cm) attached to 3 individual sheep within the herd. The herd are being walked up-hill at an average speed of $1.2 \text{ m}\cdot\text{s}^{-1}$. The acoustic spectrum shows a clear strike tone at 750 Hz followed by a series of harmonically grouped overtone/partial at 2.3 to 2.66 kHz, 4.08 to 4.85 kHz. The dispersion frequency spans of these of these groups are of the order of 1 kHz.

The frequency position of the overtones/partial reveal two features of note. Firstly it is known that sonic energy travels approximately 14 times faster through iron when compared to air, which will result partials having a different harmonic relationship to the strike tone. Secondly, the odd harmonic relationship of the reference bell, as discussed in section 3.1, is observed; in that they have an odd harmonic relationship ($n = 3$ (2.55 kHz); $n = 5$ (4.25 kHz); and $n = 7$ (5.95 kHz) to the strike tone. Using equation 1 the frequency of the strike tone corresponds to the characteristic bell length of 10 cm. However, the overtones appear to have twice the bandwidth (~ 1 kHz) as compared to the reference iron bell (~ 0.5 kHz).

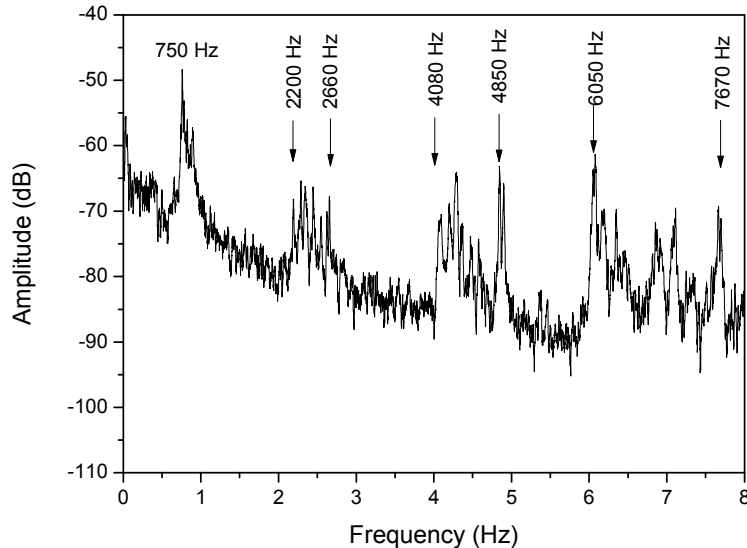


Figure 3: Frequency response of sheep herd walking up-hill at 1.2 m.s^{-1} .

3.3. Sheep bell response as the herd is moving down-hill

Figure 4 shows a representative frequency signature of the 10 acoustic recordings of the same herd with three bells, but as they are walking down-hill in the morning at an average speed of 2.4 m.s^{-1} . When compared to the sheep walking up-hill spectrum (figure 3) the recorded spectrum shows that the strike tone, a 425 Hz tone and overtones/partials are present but there is a significant increase in the number of discrete and irregular frequency spaced (10 to 100 Hz) noise (14 to 20 dBc) peaks between the bell's strike tone and the 3rd overtone/partial without altering the frequency dependent noise floor level at the even harmonics ($n = 2$ (1.7 kHz); $n = 4$ (3.4 kHz); and $n = 6$ (5.1 kHz)) locations.

It is known that when quadrupeds such as sheep change their forward speed from walk to trot their gait cycle duration (beat-to-beat per limb) changes dramatically from 0.8 to 0.1s. Thus for a herd of 30 quadrupeds (of mixed age, size and health) moving at a trot speed of 2.5 m/s, we might expect a mean acoustic frequency response of 1.2 kHz. Given the factor of 2 increase in herd speed between the up-hill (figure 3) and down-hill (figure 4) recordings, the additional irregular peaks may originate from the impact of the sheep's trotters. Our measurements show that the statistical variance for the same herd can be $\pm 0.8 \text{ kHz}$.

To analyse the sheep gait, an audio-visual movie was made for both the upward and downward directions of the herd. It was found that the sheep have a two-beat diagonal gait (trot) where the diagonal pairs of legs move forward at the same time in the down-hill case (2.4 m.s^{-1}). In the up-hill case (1.2 m.s^{-1}) the sheep tend to move one leg at a time. This result is in good agreement with the work of J. Kim and G. Breur who used a pressure sensing walkway to measure

the gait of Suffolk-mix sheep [4]. In their work it was reported that the walking trot gait imparted 50-56% of the sheep's body weight to the synchronised diagonal forward and hind limb with a disparity of 59% to 41% in favour of the forward limb. This would imply the loudness of the sheep trot signature would be greater than the up-hill walking gait where one limb is moved at a time. It is presumed that in our case the loudness (noise) of the sheep walking up-hill gait is not observed due to the noise floor of the acoustic measurement.

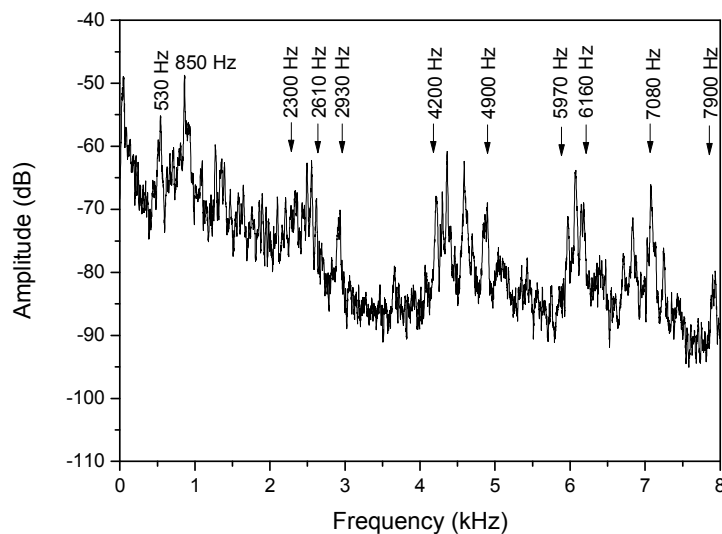


Figure 4: Frequency response of sheep herd walking down-hill at 2.4 m.s^{-1} .

4. Conclusion

Acoustic recordings of iron composite bells have been made in the frequency range of 0 to 8 kHz. The acoustic signature of single (and isolated) reference bell is used to identify the bells strike tone and overtones/partials response when the clapper struck against the metal rim. It is found the bell supports doublets strike tone and doublets of odd overtones/partials and abates the even overtones/partials. A single quarter wavelength closed air column is used to model the acoustic response. However the single model it is not sufficiently detailed to provide the true doublet response on the composite iron bell. Therefore a double quarter-wave model is proposed. Given new model the recordings are then used as a reference to decode the frequency dependent acoustic signature of bells attached to 3 sheep within a herd of 27 to 30 healthy male and female Sfakia sheep as they are walked up-hill and down-hill on an inclined (10%) concrete road at a pace of 1.2 and 2.4 m.s^{-1} , respectively.

Time series analyses of the acoustic recordings of the herd indicate that there is significant difference in the up-hill and down-hill. The difference in acoustic signature is attributed to the change in the walking gait of the sheep: from one-beat-to-beat impact as the sheep alter their gait from a walk to a trot.

Acoustically the difference occurs in the 850 Hz to 2 kHz frequency range which is the sensitive hearing range of the human ear.

It is concluded that the movement behaviour of a sheep herd that lay between the extremes of grazing and predator threat can be discriminated using the non-obtrusive and non-worrying technique of acoustic recording.

Acknowledgements

This work was supported in part by the 7th CHAOS2014 International Conference, Lisbon, Portugal organizing committee.

References

1. N. H. Packard, J. P. Crutchfield, J. D. Farmer, and R. S. Shaw. Geometry from time series. *Phys. Rev. Letts.* **45**(9), 712-716, 1980.
2. N. F. Thornhill, H. Melbø, and J. Wiik. Multidimensional visualization and clustering of historical process data. *Ind. Eng. Chem. Res.* **45**, 5971-5985, 2006.
3. N. Vevtić, S. Zelechowski, H. Feldman, C. Peterson, J. S. Schweitzer. Nonlinear Time Series Analysis of the DB White Dwarf PG 1351+489 Light Intensity Curves. *The Astrophysical Journal.* **635**(1), 527-539, 2005.
4. J. Kim, and G. J. Breur. Temporospacial and kinetic characteristics of sheep walking on a pressure sensitive walkway. *Can. J. Vet. Res.* **72** 50-55, 2008.
5. S. W. Smith. Audio processing. *The scientist and engineer's guide to digital processing.* Chp22, 351-372. California Technical Publishing, San Diego, USA. 1997.
6. J. Tynan, V. J. Law, P. Ward, A. M. Hynes, J. Cullen, G. Byrne, S. Daniels, and D. P. Dowling,. Comparison of pilot and industrial scale atmospheric pressure glow discharge systems including a novel electro-acoustic technique for process monitoring. *PSST*, **19**, 015015, 2010.
7. V. J. Law, C. E. Nwankire, D. P. Dowling, and S. Daniels. Acoustic emission within an atmospheric helium discharge jet. *Chaos Theory: Modeling, Simulation and Applications.* 255-264. Eds: C. H. Skiadas, I. Dimotikalis and C. Skiadas. Publisher: World Scientific 2011.
8. V. J. Law, F. T. O'Neill and D. P. Dowling. Evaluation of the sensitivity of electro-acoustic measurements for process monitoring and control of an atmospheric pressure plasma jet system. *PSST.* **20**(3), 035024, 2011.
9. V. J. Law, D. P. Dowling, J. L. Walsh, F. Iza, N. B. Janson, and M. G. Kong. Decoding of atmospheric pressure plasma emission signals for process control. *CMSIM* **1.** 69-76. 2011.
10. V. J. Law, M. Donegan and B. Creaven. Acoustic metrology: from atmospheric plasma to solo percussive irish dance *CMSIM Journal* **4**, 663-670, 2012.
11. A. Savitzky and M. J. Golay. 1964 Smoothing and differentiation of data by simplified least squared procedures *Anal. Chem.* **36**, 2627-2639, 1964.

Chaotic Neural Networks with a “Small-World” Topology Can Achieve Pattern Recognition*

Ke Qin¹ and B. J. Oommen^{2,3}

¹ University of Electronic Science and Technology of China, Chengdu, China. 611731
(E-mail: qinke@uestc.edu.cn)

² Carleton University, Ottawa, ON, Canada. K1S 5B6

³ University of Agder, Postboks 509, 4898 Grimstad, Norway.
(E-mail: oommen@scs.carleton.ca)

Abstract. This paper confirms the fascinating result that we can design chaotic Neural Networks (NNs) that have a “small-world” or “scale-free” topology and that these NNs can achieve *chaotic* Pattern Recognition (PR). What we imply by this is that the NN yields a strong *periodic* or *more frequent* signal when a pattern is recognized, and in between two consecutively recognized patterns, none of the trained patterns are recalled. Finally, and most importantly, if an untrained pattern is presented, the system yields a chaotic signal. The foundational NN that we employ for this is the Adachi Neural Network (AdNN). The latter is a fascinating NN which has been shown to possess chaotic properties, and to also demonstrate Associative Memory (AM) and PR, while variants of the AdNN have also been used to obtain other PR phenomena, and even blurring. The problem with the Adachi NN is that it is a fully-connected network requiring quadratic computations for the training. Our aim in this paper is to reduce the computations needed for the training *significantly*. In [1] we managed to reduce the AdNN’s computational cost significantly by merely using a linear number of computations by enforcing a Maximum Spanning Tree topology and a gradient search method. However, from the perspective of a network’s *structure*, very few real-life networks have a tree-shaped *linearly*-connected topology. The question we consider in this paper is whether we can reduce the degree of connections of each node to mimic the small-world or scale-free phenomena, more akin to “*real*” NNs. Simultaneously, we shall also attempt to ensure that the newly-obtained network still possesses strong PR characteristics. To achieve this, we first construct a small-world network by means of the so-called N-W model. We then address the problem of computing the weights for the new NN. This is done in such a manner that the modified small-world connection-based NN has approximately the same input-output characteristics, and thus the new weights are themselves calculated using a gradient-based algorithm. By a detailed experimental analysis, we show that the new small-world AdNN-like

*A preliminary version of this paper was presented at CHAOS’14, the 2014 Chaotic Modeling and Simulation International Conference, Lisbon, Portugal, in June 2014. The work of the first author is supported by National Natural Science Foundation of China (Grant NO. 61300093) and Fundamental Research Funds for the Central Universities in China: ZYGX2013J071.

Received: 4 February 2014 / Accepted: 7 September 2014

© 2014 CMSIM



ISSN 2241-0503

network possesses PR properties for appropriate settings. As far as we know, such a small-world AdNN has not been reported, and the results given here are novel.

Keywords: Chaotic Neural Networks, Chaotic Pattern Recognition, Adachi-like Neural Networks, Small-world Networks.

1 Introduction

The goal of the field of Chaotic Pattern Recognition (PR) systems can be expressed as follows: We do not intend a chaotic PR system to report the identity of a testing pattern with a “proclamation” of the pattern’s class. Rather, what we want to achieve, on one hand, is to have the chaotic PR system give a strong *periodic* or *more frequent* signal when a pattern is to be recognized. Further, between two consecutive recognized patterns, none of the trained patterns must be recalled. Finally, and most importantly, if an untrained pattern is presented, the system must give a chaotic signal. This is analogous to how the brain works. Once a pattern is recalled from a memory location, the brain is not “stuck” to it, it is also capable of recalling other Associated Memory (AM) patterns. This ability to “jump” from one memory state to another *in the absence of a stimulus* is one of the hallmarks of the brain, and *this is one phenomenon that a chaotic PR system has to emulate*.

Adachi *et al* and Calitoiu *et al* have done a lot of ground-breaking work in this area [2–4], and we have built on these results in various avenues [3–6], including that of designing a NN that can yield *ideal* chaotic PR [7]. Generally speaking, the computational burden of the original AdNN and its variants [2–4] is quadratic, rendering them to be impractical machines.

This is also true of most of the current NNs which possess a regular topology, e.g., a completely connected graph or a neighbor-coupled graph. In [1] we managed to reduce the AdNN’s computational cost significantly by merely using a linear number of computations by enforcing a Maximum Spanning Tree topology and a gradient search method. In our previous paper [6], we succeeded in creating a Random-AdNN by using the E-R model. Then we computed the weights for the new network by means of gradient search. The newly obtained network was shown to still possess PR and AM properties.

All of these must be contrasted with “real” NNs which usually have irregular topology. In this paper we shall attempt to design and implement a NN (which we shall refer to as “Smallworld-AdNN”) that demonstrates such *chaotic* PR properties, even though this newly-designed network, in and of itself, is a “small-world” or “scale-free” network. This is the primary contribution of this paper. Briefly stated, this is achieved by using the N-W model followed by an effective gradient search strategy, whence the computational burden can be significantly reduced. Further, as we shall show presently, the Smallworld-AdNN is almost as effective as the fully-connected AdNN with regard to its chaotic and PR characteristics.

2 Designing the Smallworld-AdNN

2.1 The Topology of the Smallworld-AdNN

To design the Smallworld-AdNN, we shall first arrive at a topology with edges connected in a small-world manner. There are many ways to generate a small-world NN, for example, by invoking the Watts-Strogatz (W-S) [8] or the Newman-Watts (N-W) models [9], and we shall use the former.

The general steps of the obtaining a W-S model are as follows:

1. Arrange the neurons in a cycle, and index them from 1 to N .
2. Create a neighbor-coupled network, where each neuron is connected with $k/2$ neurons on both its sides. Thus, the degree for each neuron is k .
2. Re-connect each edge of the network with fixed probability pr . That is, for each edge, delete it with a probability pr and connect it with another randomly chosen neuron.

The reader will observe two special situations that arise from this W-S model: The new network becomes a random network if $pr = 1$ while it remains the same if $pr = 0$.

Obviously, the W-S model has the potential of causing some neurons to become isolated. In [9], Watts and his coauthor improved the W-S model by edge addition instead of deletion. Thus the second step is modified as follows: Randomly connect two unconnected neurons with a fixed probability pr . Again, one can then see that if $pr = 1$, the network becomes fully connected while it remains the same if $pr = 0$. It is worth pointing out that the W-S and N-W are essentially the same when pr is small and the number of neurons, N , is large. In this paper, we shall use the N-W model to create a small-world network. Consequently, we build the topology of the Smallworld-AdNN by invoking the following algorithm.

Algorithm 1 Topology_Smallworld-AdNN

Input: N , the number of neurons in the network, and a set of p patterns which the network has to “memorize”.

Output: The topology and initial weights of the Smallworld-AdNN.

Method:

- 1: Create a neighbor-coupled graph, \mathcal{G} , with N vertexes which is to represent the AdNN.
- 2: Connect two randomly chosen unconnected neurons with a fixed probability pr .
- 3: Compute the initial weights of the edges of \mathcal{G} , $\{w_{ij}\}$, by the following:
 $w_{ij} = \frac{1}{p} \sum_{s=1}^p (2x_i^s - 1)(2x_j^s - 1)$, where x_i^s is the i^{th} component of the s^{th} stored pattern.
- 4: If there is no edge between vertex i and j , then let $w_{ij} = 0$;

End Algorithm Topology_Smallworld-AdNN

Since the network topology has been changed and we want the Smallworld-AdNN to maximally approximate the original AdNN, we thus invoke the second step that involves the computation of the weights associated with this structure.

2.2 The Weights of the Smallworld-AdNN: Gradient Search

Since we have successfully created the structure of the Smallworld-AdNN by using the N-W model, our next task is to determine a new set of weights so as to force the Smallworld-AdNN to retain some of its PR properties, namely those corresponding to the trained patterns. We briefly explain below the process for achieving this.

The Smallworld-AdNN is defined by following equations:

$$x_i^S(t+1) = f(\eta_i^S(t+1) + \xi_i^S(t+1)), \quad (1)$$

$$\eta_i^S(t+1) = k_f \eta_i^S(t) + \sum_{e_{ij} \in \mathcal{G}} w_{ij}^{S*} x_j^S(t), \quad (2)$$

$$\xi_i^S(t+1) = k_r \xi_i^S(t) - \alpha x_i^S(t) + a_i. \quad (3)$$

where $\{w_{ij}^{S*}\}$, x_i^S , ξ_i^S and η_i^S are the weights, outputs, and state variables of the Smallworld-AdNN respectively, and have similar meanings to $\{w_{ij}\}$, x_i , ξ_i and η_i of the AdNN. To find the optimal values of $\{w_{ij}^{S*}\}$, we define the square error between the original output of the AdNN and new output at the n^{th} step:

$$E_p = \frac{1}{2} \sum_{i=1}^N (x_i^{A,p} - x_i^{S,p}(n))^2, \quad (4)$$

where $x_i^{A,p}$ and $x_i^{S,p}$ imply the outputs of the i^{th} neuron when the p^{th} pattern is presented to the AdNN network and the Smallworld-AdNN network respectively. The overall global error is defined by $E = \sum_{p=1}^P E_p$ where P is the number of trained patterns. In order to adjust w_{ij}^S to obtain the least global error E , we consider the gradient, Δw_{ij}^S , and move w_{ij}^S by an amount which equals Δw_{ij}^S in the direction where the error is minimized. Formally:

$$\begin{aligned} \Delta w_{ij}^S &= -\beta \frac{\partial E}{\partial w_{ij}^S} = -\beta \frac{\partial \sum_{p=1}^P E_p}{\partial w_{ij}^S} = -\beta \sum_{p=1}^P \frac{\partial E_p}{\partial x_i^{S,p}(n)} \cdot \frac{\partial x_i^{S,p}(n)}{\partial w_{ij}^S} \\ &= \beta \sum_{p=1}^P (x_i^{A,p} - x_i^{S,p}(n)) \cdot \frac{1}{\varepsilon} \cdot x_i^{S,p}(n) \cdot (1 - x_i^{S,p}(n)) \cdot x_j^{S,p}(n), \end{aligned} \quad (5)$$

where β is the learning rate of the gradient search.

The formal algorithm which achieves the update is given in Algorithm 2. Its Lyapunov analysis is found in [10].

The results of a typical numerical experiment which proceeds along the above gradient search are shown in Fig. 1 and 2. Here, we have chosen the learning rate β to be 0.05 and $pr = 0.5$. Specifically, we report our experiments for three cases, i.e., when $k/2 = 4$, $k/2 = 6$ and $k/2 = 10$ respectively. If $k/2 = 4$, the average value of Δw_{ij}^S does not converge at 0, as shown in Fig. 1.

As $k/2$ increases, e.g., $k/2 = 6$, Δw_{ij}^S converges to 0, as shown in Fig. 2 (a). If $k/2$ is even larger, Δw_{ij}^S also converges to 0 but at a faster rate. This phenomenon can be easily explained: The larger the value of $k/2$, the more are

Algorithm 2 Weights_Smallworld-AdNN

Input: The number of neurons, N , a set of P patterns, and the initial weights $\{w_{ij}^S\}$ of the Smallworld-AdNN. These initial weights are $\{w_{ij}^A\}$ for the edges in the smallworld graph, and are set to *zero* otherwise. The parameters and the setting which we have used are the learning rate $\beta = 0.05$, $\varepsilon = 0.015$, $\alpha = 10$, $k_f = 0.2$ and $k_r = 1.02$.

Output: The weights $\{w_{ij}^{S*}\}$ of the Smallworld-AdNN.

Method:

- 1: Compute the outputs of the Smallworld-AdNN corresponding to the P trained inputs.
- 2: For all edges of the Smallworld-AdNN, compute Δw_{ij}^S as per Equation (5). Otherwise, set $\Delta w_{ij}^S = 0$.
- 3: $w_{ij}^S \leftarrow w_{ij}^S + \Delta w_{ij}^S$.
- 4: Go to Step 1 until E is less than a given value or $\Delta w_{ij}^S \approx 0$.

End Algorithm Weights_Smallworld-AdNN

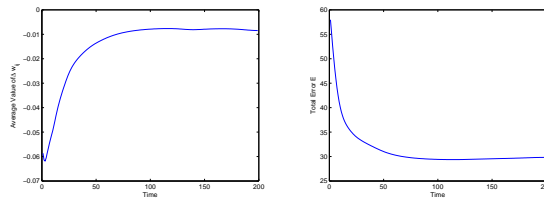


Fig. 1. The figure on the left shows the variation of the average of Δw_{ij}^S (averaged over all values of i and j) over the first 200 iterations of the gradient search scheme. The average converges to a value arbitrarily close to zero after 70 time steps. The figure on the right shows the variation of the global error over the same time frame. Observe that this quantity does not converge to *zero*.

the edges that the Smallworld-AdNN has, leading to a better-fitting effect. In practice, we have opted to choose $k/2 = 6$ to obtain a finer trade-off between the effect of the fit and the associated computational cost.

3 Chaotic and PR Properties of the Smallworld-AdNN

We now briefly report the PR properties of the Smallworld-AdNN. These properties have been gleaned as a result of examining the Hamming distance between the input pattern and the patterns that appear in the output. In this regard, we mention that the experiments were conducted using the Adachi data set, as shown in Fig. 3.

In the ideal setting we would have preferred the Smallworld-AdNN to be chaotic when exposed to untrained patterns, and the output to appear periodically or more frequently when exposed to trained patterns. Besides yielding this phenomenon, the Smallworld-AdNN also goes through a chaotic phase and a PR phase as some of its parameters change.

By studying Fig. 1 and 2 we see that if $k/2 = 6$, the Smallworld-AdNN can fit the original AdNN very well. Thus, we have set the parameters in Algorithm 1 to be $pr = 0.5$ and $K = 6$ so as to obtain a better trade-off effect. In this

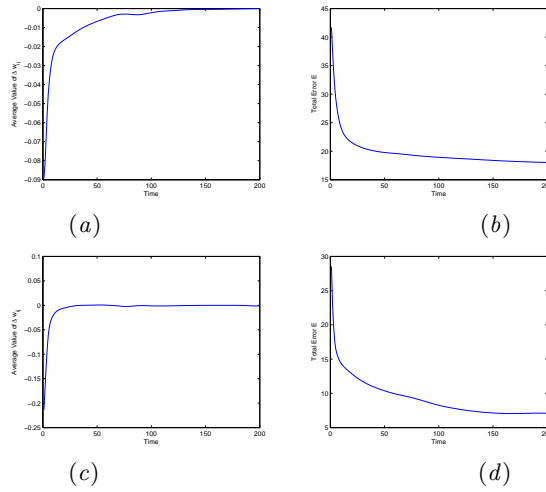


Fig. 2. The figures show the variation of the average of Δw_{ij}^S and the global error over the same time frame. The degree of the connection is $k = 12$ (for (a) and (b)) and $k = 20$ (for (c) and (d)) respectively.

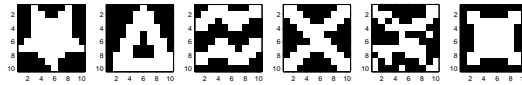


Fig. 3. The 10×10 patterns used by Adachi *et al.* The first four patterns are used to train the network. The fifth patterns are obtained from the corresponding fourth patterns by including 15% noise in (a) and (b) respectively. The sixth pattern is the untrained pattern.

regard, we comment that using the values of $pr = 0.5$ and $k/2 = 6$ are good enough for PR, which also significantly minimizes the computational burden. Indeed, as one can see, the distribution for the degree of each vertex of the Smallworld-AdNN has the form:

$$p(k) = \binom{N}{k-6} \left(\frac{3}{N}\right)^{k-6} \left(1 - \frac{3}{N}\right)^{N-k+6} \tag{6}$$

which is approximately a Poisson distribution, as shown in Fig. 4.

We summarize the results for the Smallworld-AdNN by using different settings of pr . The others parameters are: $k_f = 0.2$, $k_r = 1.02$, $\alpha = 10$, $\varepsilon = 0.015$, $\beta = 0.05$. The results are tabulated in Tables 1, 2 and 3.

Consider Table 1. From this table we clearly see that the Smallworld-AdNN is able to “resonate” the input patterns with corresponding output patterns. If P1 is the input, then the network outputs P1 accordingly, while at the same time, no other trained patterns appear in the output sequence. Even when a noisy pattern is presented to the system, e.g., P5, which is a noisy pattern of P4 with 15% noise, the network still “resonates” P4 instead of P5 in the output sequence. Furthermore, if the input is an untrained pattern, e.g., P6, none of

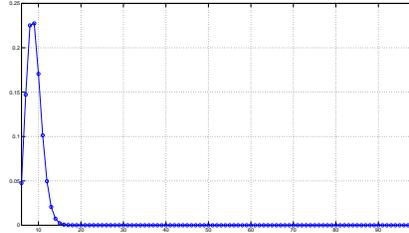


Fig. 4. The degree of each neuron obeys the Poisson distribution. From this figure we can see that most of the neurons have degree 8 or 9, which means that the computational load has been significantly reduced when compared to the original AdNN, which we know has a vertex degree of 99.

Table 1. The frequency of the Hamming distance between the input and the output patterns for the Smallworld-AdNN. The probability $pr = 0.5$ and $k/2 = 6$.

$pr = 0.5, k/2 = 6$		Input Patterns					
		P1	P2	P3	P4	P5	P6
Retrieved Patterns	P1	96	0	0	0	0	0
	P2	0	376	0	0	0	0
	P3	0	0	108	0	0	0
	P4	0	0	0	93	136	0
	P5	0	0	0	9	2	0
	P6	0	0	0	0	0	28

Table 2. The frequency of the Hamming distance between the input and the output patterns for the Smallworld-AdNN. The probability $pr = 0.1$ and $k/2 = 6$.

$pr = 0.5, k/2 = 6$		Input Patterns					
		P1	P2	P3	P4	P5	P6
Retrieved Patterns	P1	49	0	0	0	0	0
	P2	0	126	0	0	0	0
	P3	0	0	53	0	0	0
	P4	0	0	0	68	78	0
	P5	0	0	0	3	1	0
	P6	0	0	0	0	0	3

Table 3. The frequency of the Hamming distance between the input and the output patterns for the Smallworld-AdNN. The probability $pr = 0.9$ and $k/2 = 6$.

$pr = 0.5, k/2 = 6$		Input Patterns					
		P1	P2	P3	P4	P5	P6
Retrieved Patterns	P1	578	0	0	0	0	0
	P2	0	685	0	0	0	0
	P3	0	0	309	0	0	0
	P4	0	0	0	412	389	0
	P5	0	0	0	11	8	0
	P6	0	0	0	0	0	15

the trained patterns will be recalled. In this case, even the input pattern P6 itself, will be retrieved only a few times, as one can see is much less than the other diagonal numbers obtained when input is P1 – P4.

4 Conclusions

In this paper we have concentrated on the field of Chaotic Pattern Recognition (PR), which is a relatively new sub-field of PR. Such systems, which have only recently been investigated, demonstrate chaotic behavior under normal conditions. The system would, however resonate (or produce a single pattern more frequently) when it is presented with a pattern that it is trained with. The network which we have investigated is the Adachi Neural Network (AdNN) [2–4], based on which we have, ourselves, developed results in various avenues [3–6], including that of designing a NN that can yield *ideal* chaotic PR [7]. In this paper we have considered how the topology can be modified so as to render the network to be much closer to “real” neural networks. To achieve this, we have changed the network structure to be that of a Small-world graph, and then computed the best weights for the new graph by using a gradient-based algorithm. Apart from a Lyapunov analysis, by a detailed experimental suite, we have shown that the new Smallworld-AdNN possesses chaotic and PR properties for different settings.

References

1. Qin, K., Oommen, B.J.: Adachi-like chaotic neural networks requiring linear-time computations by enforcing a tree-shaped topology. *IEEE Transactions on Neural Networks* **20**(11) (2009) 1797–1809
2. Adachi, M., Aihara, K.: Associative dynamics in a chaotic neural network. *Neural Networks* **10**(1) (1997) 83–98
3. Calitoiu, D., Oommen, B.J., Nussbaum, D.: Desynchronizing a chaotic pattern recognition neural network to model inaccurate perception. *IEEE Transactions on Systems Man and Cybernetics Part B-Cybernetics* **37**(3) (2007) 692–704
4. Calitoiu, D., Oommen, B.J., Nussbaum, D.: Periodicity and stability issues of a chaotic pattern recognition neural network. *Pattern Analysis and Applications* **10**(3) (2007) 175–188
5. Qin, K., Oommen, B.J.: Chaotic pattern recognition: The spectrum of properties of the Adachi neural network. In: *Lecture Notes in Computer Science*. Volume 5342., Florida, USA (2008) 453–460
6. Qin, K., Oommen, B.J.: *Chaotic* pattern recognition using the Adachi neural network modified in a random manner. In: *Proceedings of CHAOS'13, the 2013 Chaotic Modeling and Simulation International Conference, Istanbul, Turkey* (2013) 540–550
7. Qin, K., Oommen, B.J.: Ideal chaotic pattern recognition is achievable: The Ideal-M-AdNN - its design and properties. In: *Transactions on Computational Collective Intelligence* (2013) 22–51
8. Watts, D.J., Strogatz, S.H.: Collective dynamics of ‘small-world’ networks. *Nature* **393**(4) (1998) 440–442
9. Newman, M., Barabasi, A.L., Watts, D.J.: *The Structure and Dynamics of Networks*. Princeton University Press, New Jersey (2006)
10. Qin, K.: *Generic Analysis of Chaotic Neural Networks and Their Applications in Pattern Recognition and Crypto-systems*. PhD thesis, University of Electronic Science and Technology of China, (2010)

Cascade of Hopf bifurcations in coupled chaotic oscillators

Carla M.A. Pinto

School of Engineering, Polytechnic of Porto, and
Center of Mathematics of the University of Porto,
Rua Dr António Bernardino de Almeida, 431, 4200-072, Porto, Portugal
(E-mail: cap@isep.ipp.pt)

Abstract. We study exotic patterns appearing in a network of coupled Chen chaotic oscillators. Our network consists of two rings coupled through a ‘buffer’ cell, with $\mathbf{Z}_3 \times \mathbf{Z}_5$ symmetry group. Numerical simulations of the network reveal steady-states, rotating waves, and quasiperiodic and chaotic states. The different patterns arise through a sequence of Hopf bifurcations. The network architecture explains certain observed features, whereas the properties of the cells’ internal dynamics, the Chen chaotic oscillator, may explain others.

Keywords: chaos, quasiperiodic states, symmetry, Hopf bifurcation.

1 Introduction

Stewart, Golubitsky and Pivato [16] and Golubitsky, Stewart and Török [10] have developed a theory concerning coupled dynamical systems, or coupled cell networks. A cell is a system of ordinary differential equations. Issues like synchronization phase-relations synchronized chaos, amongst others [5,8] [14,12] have been particularly focused.

General coupled cell networks may be characterized in two main groups in what concerns symmetry. One group consists of the coupled cells systems that possess some degree of symmetry, the other group gathers the coupled cells systems with no symmetry. The networks with exact symmetry are included in the first group.

The common representation of networks of coupled cells is done by directed graphs. The graphs’ nodes correspond to individual cells and the edges to the couplings between them. A ‘cell’ means a nonlinear dynamical system of ordinary differential equations. In Figure 3, the cells are represented by circles and squares and the couplings between them by arrows. Distinct cells/arrows mean distinct dynamics/couplings.

In this paper we are interested in the dynamical features occurring in a coupled system of two unidirectional rings with $\mathbf{Z}_3 \times \mathbf{Z}_5$ exact symmetry. In Section 2, we provide a review of the coupled cells networks formalism. In



Section 3, we simulate the coupled cells systems associated to the networks of two coupled rings of cells in Fig. 1. In Section 4, we conclude this work and shed some light on future research directions.

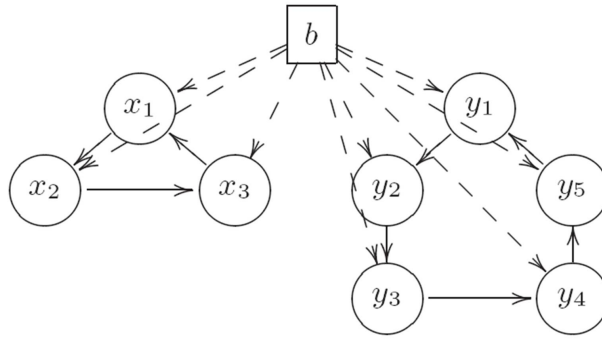


Fig. 1. Network of two coupled unidirectional rings, one with three cells and the other with five, connected through a buffer cell b . The network has $\mathbf{Z}_3 \times \mathbf{Z}_5$ symmetry group.

2 Coupled cells and symmetry

A coupled cells system consists of a finite set of nodes (or cells) \mathcal{C} , and a finite set of edges \mathcal{E} . An equivalence relation on cells in \mathcal{C} is defined, where the equivalence class of c is the type of cell c , an input set of cells $\mathcal{I}(c)$, that consists of cells whose edges have cell c as head. Moreover, an equivalence relation on the edges (or arrows), is also defined, where the equivalence class of e is the type of edge e , and it satisfies the condition that ‘equivalent edges have equivalent tails and edges’. The last condition means that equivalent edges must have tails and edges of the same equivalence class.

For each cell c an internal phase space P_c is defined. The total phase space of the network is the product $P = \prod_{i=1}^n P_c$. The coordinates on P_c are denoted by x_c , the coordinates on P are thus (x_1, x_2, \dots, x_n) . At time t , the system is at state $(x_1(t), x_2(t), \dots, x_n(t))$.

A vector field f on P that is compatible with the network architecture is said to be *admissible* for that network, and satisfies two conditions: (1) the domain - each component f_i corresponding to cell c_i must be a function of the cells in the $\mathcal{I}(c)$; (2) the pull-back condition - the components f_i and f_j of cells c_i and c_j are identical, up to a suitable permutation of the relevant variables, if the two cells have isomorphic input cells [9].

A symmetry is a transformation of the phase space that sends solutions to solutions. It consists of the group of permutations of the cells (and arrows) that preserves the network structure (including cell-types and arrow-types) and its action on P is by permutation of cell coordinates. The network in Figure 1 is an example of a network with $\mathbf{Z}_3 \times \mathbf{Z}_5$ symmetry.

3 Numerical simulations

The coupled cells system, associated with the network depicted in Fig. 1, is simulated. We use XPPAUT [7] and MATLAB [18] to compute numerically the relevant states. We consider the Chen oscillator as the phase space for each cell of the two rings and an unidimensional phase space for the ‘buffer cell’. The total phase space is thus twenty-fifth dimensional. The dynamics of a singular ring cell is given by [6,13]:

$$\begin{aligned} \dot{u} &= a(v - u) \\ \dot{v} &= (c - a)u - uv + cv \\ \dot{w} &= uv - bw \end{aligned} \tag{1}$$

where $a = 35$, $b = 3$, c are real parameters.

The unidimensional dynamics of the ‘buffer cell’ is given by [8,3]:

$$f(u) = \mu u - \frac{1}{10}u^2 - u^3 \tag{2}$$

where $\mu = -1.0$ is a real parameter.

The coupled cells system of equations associated to the network in Fig. 1 is given by:

$$\begin{aligned} \dot{x}_j &= g(x_j) + k(x_j - x_{j+1}) + db \quad j = 1, \dots, 3 \\ \dot{b} &= f(b) \\ \dot{y}_j &= g(y_j) + k(y_j - y_{j+1}) + db \quad j = 1, \dots, 5 \end{aligned} \tag{3}$$

where $g(u)$ represents the dynamics of each Chen oscillator, $k = -5.0$, $d = 0.2$, and the indexing assumes $x_4 \equiv x_1$ and $y_6 \equiv y_1$. We assume that the coupling between all cells is linear and is done only in the first variable of each Chen oscillator.

We vary parameter $c \in [15, 22]$, going from lower to higher values, and start from a steady state of the whole system.

In Figure 2, we plot (top) the time series solution of the coupled cell system (3) and (bottom) we represent the phase plane of oscillator y_1 of the 5-ring. The solution is a rotating wave state in the 5-ring, obtained by a Hopf bifurcation (HB1), from the trivial equilibrium branch. Cells in the 3-ring are at equilibrium. These solutions can be explained using the Equivariant Hopf Theorem for coupled cell systems in the symmetric case [11]. The bifurcation has occurred in the 5-ring.

We increase c again, and another Hopf bifurcation occurs (HB2). In Figure 3, we plot (top) the time series solution of the coupled cell system (3), (center) we show the phase planes for the oscillator x_1 of the 3-ring (center, left) and of the oscillator y_1 of the 5-ring (center, right). The solution is a rotating \mathbf{Z}_3 wave in the 3-ring and a rotating \mathbf{Z}_5 wave in the other ring. The full solution is quasiperiodic (Fig. 3, bottom).

Figure 4 shows the time series further away from the tertiary Hopf bifurcation (HB3) in the coupled cell system (3). Unlike the previous cases (Figures 2-3), the amplitude of the solution is higher and the wave form is qualitatively different, displaying typical relaxation oscillatory features. Relaxation oscillations are

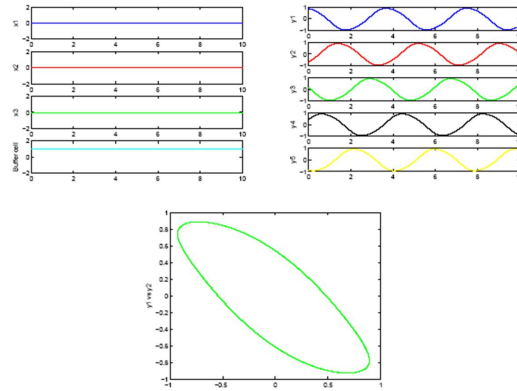


Fig. 2. Simulation of the coupled system (3) with $\mathbf{Z}_3 \times \mathbf{Z}_5$ symmetry. Time series from the nine cells after the first Hopf bifurcation point (HB1). (Top, left) Cells in the 3-ring are at equilibrium and cells in the 5-ring display a \mathbf{Z}_5 rotating wave (top, right). (Bottom) Phase plane of oscillator y_1 of the 5-ring.

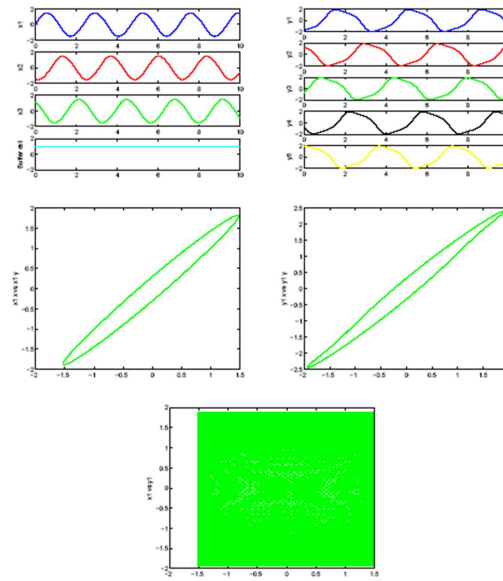


Fig. 3. Simulation of the coupled system (3) with $\mathbf{Z}_3 \times \mathbf{Z}_5$ symmetry, after the second Hopf bifurcation point (HB2). The cells in the 3-ring exhibit a rotating \mathbf{Z}_3 wave (top, left), and the cells in the other ring show a rotating \mathbf{Z}_5 wave (top, right). Phase planes of the oscillator x_1 (center, left) and of the oscillator y_1 (center, right). Cell x_1 vs cell y_1 (bottom). For more information see text.

solutions characterized by long periods of quasi-static behaviour interspersed

with short periods of rapid transition. These solutions are studied in the context of the canard phenomenon [17] in fast-slow systems.

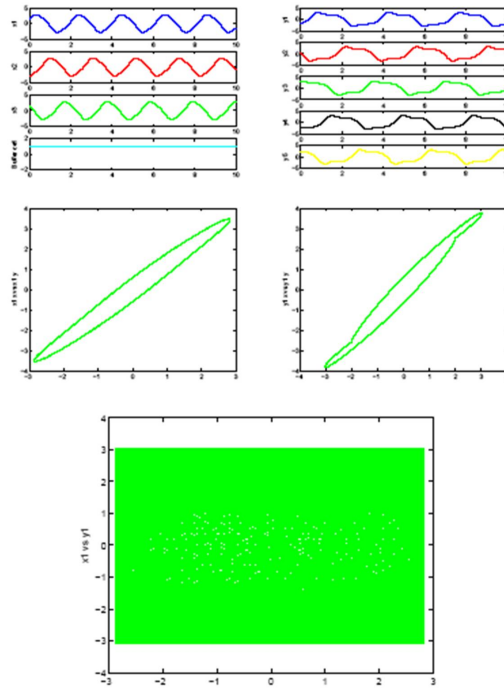


Fig. 4. Simulation of the coupled system (3) with $\mathbf{Z}_3 \times \mathbf{Z}_5$ symmetry, after the third Hopf bifurcation point (HB3). The cells in the 3-ring exhibit a \mathbf{Z}_3 rotating wave (top, left), whereas cells in the other ring depict a relaxation oscillation (top, right). Phase planes of the oscillator x_1 (center, left) and of the oscillator y_1 (center, right). Cell x_1 vs cell y_1 (bottom). For more information see text.

Further away of this third Hopf bifurcation point, ‘unusual’ and complex behaviors start to appear. In Fig. 5, the cells in the 3-ring appear to show a quasiperiodic motion and the cells in the 5-ring seem to depict a chaotic state. The full solution is quasiperiodic or chaotic (see Figure 5, bottom).

Thus, from the numerical results, we conclude that there is a richness of dynamic features produced by the network of two coupled rings with $\mathbf{Z}_3 \times \mathbf{Z}_5$ symmetry. The dynamical behavior is much more complex than the one found in [3,4,2,15], for the same network of two coupled rings with $\mathbf{Z}_3 \times \mathbf{Z}_5$ symmetry, but with simpler internal dynamics for each cell. This suggests that the network structure is important for these patterns to be observed but it seems not to be able to explain them fully.

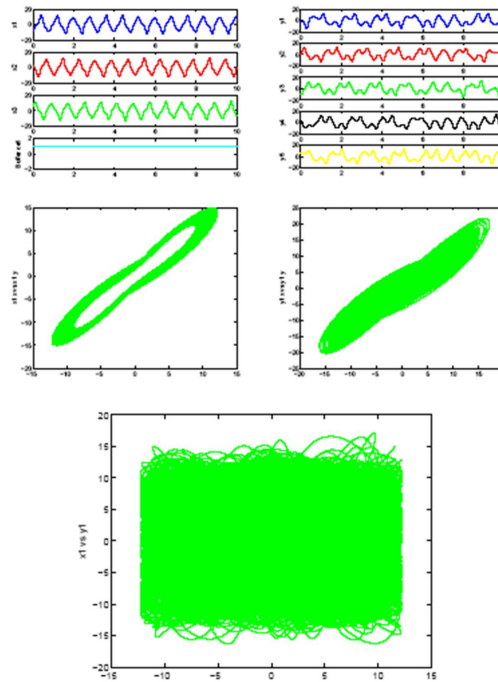


Fig. 5. Simulation of the coupled system (3) with $\mathbf{Z}_3 \times \mathbf{Z}_5$ symmetry, further away of the third Hopf bifurcation point (HB3). The cells in the 3-ring exhibit a quasiperiodic motion (top, left), whereas the cells in the other ring show a chaotic state (top, right). Phase planes of the oscillator x_1 (center, left) and of the oscillator y_1 (center, right). Cell x_1 vs cell y_1 (bottom). For more information, see text.

4 Conclusions

In this paper we study the dynamical behavior of a network consisting of two rings of chaotic Chen oscillators, that admit $\mathbf{Z}_3 \times \mathbf{Z}_5$ exact symmetry group. We find interesting patterns, some of them explained by local bifurcation theorems and some probably by the properties of the cells' internal dynamics, in this case, the Chen chaotic attractor. More work is needed to explain thoroughly these features.

5 Acknowledgements

Authors which to thank Fundação Gulbenkian, through *Prémio Gulbenkian de Apoio à Investigação 2003*, and the Polytechnic of Porto, through the *PAPRE Programa de Apoio à Publicação em Revistas Científicas de Elevada Qualidade* for financial support.

References

1. Antoneli, F., Dias, A.P.S. & Paiva, R.C. [2008] Hopf bifurcation in coupled cell networks with interior symmetries, *SIAM Journal on Applied Dynamical Systems*, **7**, 220–248.
2. Antoneli, F., Dias, A.P.S., & Pinto, C.M.A. [2010] Quasi-periodic states in coupled rings of cells, *Communications in Nonlinear Science and Numerical Simulations*, **15** 15, 1048–1062.
3. Antoneli, F., Dias, A.P.S., & Pinto, C.M.A. [2008] Rich phenomena in a network of two ring coupled through a ‘buffer’ cell, *Proc of the 2nd Conference on Nonlinear Science and Complexity NSC2008*.
4. Antoneli, F., Dias, A.P.S., & Pinto, C.M.A. [2008] New phenomena in coupled rings of cells, *Proc of the 3rd IFAC Workshop on Fractional Differentiation and its Applications FDA2008*.
5. Ashwin, P., Buescu, J., & Stewart, I. [1994] Bubbling of attractors and synchronisation of oscillators. *Physics Letters A*, **193**, 126–139.
6. Chen, G., & Ueta, T. [1999] Yet another chaotic attractor, *International Journal of Bifurcation and Chaos* **9**, 1465–1466.
7. B. Ermentrout. XPPAUT® – The differential equations tool, version 5.98, 2006. (<http://www.math.pitt.edu/~bard/xpp/xpp.html>)
8. Golubitsky, M., Nicol, M. & Stewart, I. [2004] Some curious phenomena in coupled cell systems, *Journal of Nonlinear Science*, **14**, 207–236.
9. Golubitsky, M. & Stewart, I. [2006] Nonlinear dynamics of networks: the groupoid formalism, *Bulletin of the American Mathematical Society*, **43**, 305–364.
10. Golubitsky, M., Stewart, I., Török, A. [2005] Patterns of synchrony in coupled cell networks with multiple arrows. *SIAM Journal of Applied Dynamical Systems* **4** (1) 78–100.
11. Golubitsky, M., Stewart, I. & Schaeffer, D.G. [1988] *Singularities and Groups in Bifurcation Theory*, vol. 2. Applied Mathematical Sciences **69**, Springer-Verlag, New York.
12. Kuramoto, Y. [1984] *Chemical Oscillations, Waves, and Turbulence*, Springer, Berlin.
13. Lü, J.H., Zhou, T.S., Chen, G.R., & Zhang, S.C. [2002] Local bifurcation of the Chen system, *International Journal of Bifurcation and Chaos* **12**, 2257–2270.
14. Pecora, L.M. & Carroll, T.L. [1990] Synchronization in chaotic systems, *Phys. Rev. Lett.*, **64**, 821–824.
15. Pinto, C. [2012] Exotic dynamics in networks of coupled rings of cells. *International Journal of Bifurcation and Chaos*, **22**(3), 1250064 (13 pages).
16. Stewart, I., Golubitsky, M. & Pivato, M. [2003] Symmetry groupoids and patterns of synchrony in coupled cell networks, *SIAM Journal of Applied Dynamical Systems*, **2** (4), 609–646.
17. Szmolyan, P., & Wechselberger, M. [2001] Canards in \mathbf{R}^3 , *JDE* **177**, 419–453.
18. The MathWorks, Inc. MATLAB®, 1994–2012. (<http://www.mathworks.com>)

Microscopic reaction diffusion patterns generated in nanometer size confinements

Jorge Carballido-Landeira* and Alberto P. Muñozuri

Universidad de Santiago de Compostela, Santiago de Compostela, Spain

*E-mail: jorge.carballido@gmail.com

Abstract: The Belousov-Zhabotinsky (BZ) reaction is one of the most studied reaction-diffusion systems able to display periodic oscillations when continued stirred and target patterns and/or spirals in spatially extended systems. Once the BZ reaction is placed inside nanometric micelles surrounded by an anionic surfactant and dispersed in an oleic system, the variety of spatial patterns increase considerably. The diversity on pattern formation is originated by the two different diffusion mechanisms available depending on the reagents charge nature. Non-polar chemicals may diffuse through the membrane and into the octane while polar chemicals diffuse within the entire nanodroplet, almost two orders of magnitude slower. On changing the confinement conditions where the BZ reaction takes place, the BZ-AOT system is able to present different dynamics, ranging from Turing structures (such as spots, stripes or labyrinthine) to standing waves, antispirals and packet waves.

Keywords: Reaction Diffusion systems. Belousov-Zhabotinsky reaction. Active microemulsion.

1. Introduction

The Belousov-Zhabotinsky (BZ) reaction is considered a prototype system for studies of reaction-diffusion phenomenon. This oscillatory chemical reaction involves the bromination and consequently oxidation of an organic substrate (originally citric acid) by bromate ions immersed into a strongly acidic solution [1]. Typically the catalysts used in the BZ reaction are cerium or ferroin, but the presence of ruthenium bipyridyl $[\text{Ru}(\text{bpy})_3^{+2}]$ complex has demonstrated photosensitive features in the BZ reaction. The presence of a redox indicator exhibiting different colors in the reduced and oxidized state of catalyst helps to visualize periodical temporal oscillations while the reaction is continuously stirred or spatiotemporal patterns when the reaction is kept unstirred [2].



The possibility to encapsulate the BZ reaction into nanodroplets of nanometric micelles bridges the gap between reaction diffusion systems and the effects of confinements. Thus, the BZ reagents are confined into nanometer-sized aqueous droplets surrounded by a surfactant monolayer and soaked in a continuous hydrophobic phase (octane). Here, the polar surfactant heads are orientated inwards (towards the droplet core), while the hydrophobic tails face the oil continuous phase [3].

There are two important parameters that define the reverse microemulsions. One of them is the hydrodynamic radius of the nanodroplets (R_d), which is defined as the addition of the size of the surfactant monolayer and the water nanodroplet core (R_w) [4]. The former is determined by the surfactant size (typically the anionic sodium bis(2-ethylhexyl) sulfosuccinate also known as AOT) and the latter is proportional to the molecular ratio between the aqueous and oil phase (ω_0):

$$R_w = 1.7\omega_0$$

The other main characteristic is the volume fraction of the water phase, defined as

$$\phi_w = \frac{V_w}{(V_w + V_o)}$$

where V_w and V_o are the volume of the aqueous and oil phases of the system of the micro-emulsion system. These properties of the micro-emulsion have a direct influence in the measurable features of the BZ reaction [5-7]

The so-called BZ-AOT system presents two different diffusive mechanisms of the chemical components. Polar BZ reagents are confined into the aqueous phase of the reverse microemulsion and diffuse with the water nanodroplets. The diffusion coefficient is then determined by the Stokes-Einstein equation:

$$D_d = \frac{K_B T}{6\pi\eta R_d}$$

where K_B , T , η are Boltzmann constant, the absolute temperature and the viscosity of the solvent, respectively.

In the course of the reaction several nonpolar intermediates are generated. These non-polar chemicals are able to diffuse through the membrane and into the oleic phase as single molecules with exhibiting diffusion coefficients almost two orders of magnitude faster than usual nanodroplets. Among the intermediates are the Br_2 and BrO_2 , which are known as fast-diffusing inhibitor and fast-diffusing activator, respectively [3].

2. The Model and Simulations

In order to model the main characteristics of the BZ-AOT system, Vanag and Epstein have proposed a variation of the well-known Oregonator model [8]. Thus, their model accounts those species able to migrate into the oleic phase in addition to the “ordinary” chemical reactions occurring in the aqueous compartments. The dynamics achieved in the BZ-AOT system can be expressed by the following set of differential equations [3]:

$$\frac{\partial x}{\partial \tau} = F(x, z, s, u) + D_x \Delta x \quad (1)$$

$$\frac{\partial z}{\partial \tau} = G(x, z, s, u) + D_z \Delta z \quad (2)$$

$$\frac{\partial s}{\partial \tau} = H(x, z, s, u) + D_s \Delta s \quad (3)$$

$$\frac{\partial u}{\partial \tau} = K(x, z, s, u) + D_u \Delta u \quad (4)$$

with

$$F(x, z, s, u) = -fz \frac{(x - q)}{(x + q)} + x(1 - \beta) - x^2 + s$$

$$G(x, z, s, u) = x - z(1 + \alpha) + \gamma u + D_z \Delta z$$

$$H(x, z, s, u) = \frac{1}{\varepsilon_1} (\beta x - s + \chi u) + D_s \Delta s$$

$$K(x, z, s, u) = \frac{1}{\varepsilon_2} (\alpha z - \gamma u) + D_u \Delta u$$

where x, z are the dimensionless concentrations of HBrO_2 and the catalyst of the reaction (i.e. ferriox, $\text{Ru}(\text{bpy})$, cerium), while s and u are the species soluble into the oleic phase: the inactive form of activator (BrO_2) and the inhibitor (Br_2), respectively. To account the differences in the diffusion rates we used $D_s = D_u \gg D_x = D_z$

The homogeneous steady state concentrations can be achieved by finding the solutions of the equations (1)-(4) once the temporal and spatial derivatives are setted to zero, *i.e.*, by solving $F(x, z, s, u) = 0$, $G(x, z, s, u) = 0$, $H(x, z, s, u) = 0$ and $K(x, z, s, u) = 0$. The stability of each one of the possible steady states will be determined by the eigenvalues obtained through the characteristic equation [9]:

$$\det(\mathbf{A} - \lambda \mathbf{I} - k^2 \mathbf{D}) = 0$$

where \mathbf{I} is the identity matrix, \mathbf{D} is the matrix of the diffusion coefficients here consider diagonal (neglecting cross-diffusion effects (even though they have been experimentally observed in the BZ-AOT systems) and \mathbf{A} is the Jacobian matrix of equations (5)-(6):

$$A(x, z, s, u) = \begin{pmatrix} \left(1 - \beta - 2x - \frac{f(q-x)z}{(q+x)^2} - \frac{fz}{(q+x)}\right) / \varepsilon & f(q-x) / (\varepsilon(q+x)) & 1/\varepsilon & 0 \\ 1 & -1 - \alpha & 0 & \gamma \\ (\beta \varepsilon_2) & 0 & -(1/\varepsilon_2) & \chi \varepsilon_2 \\ 0 & \alpha \varepsilon_3 & 0 & -\gamma \varepsilon_3 \end{pmatrix}$$

We observed that although Turing and Hopf instabilities may coexist in our range of parameters, the predominant mode differs according to the diffusion coefficient ratio (Figure 1). Thus, when the diffusion coefficient of the non-polar species is almost two-fold larger than the diffusion of the entire nanodroplet the dispersion relationship exhibits a predominant Turing mode slightly predisposed by Hopf domain (purple curve in Figure 1). However, decreasing the ratio of diffusion coefficients the Hopf mode prevails (red curve) until the Turing mode vanishes (black curve).

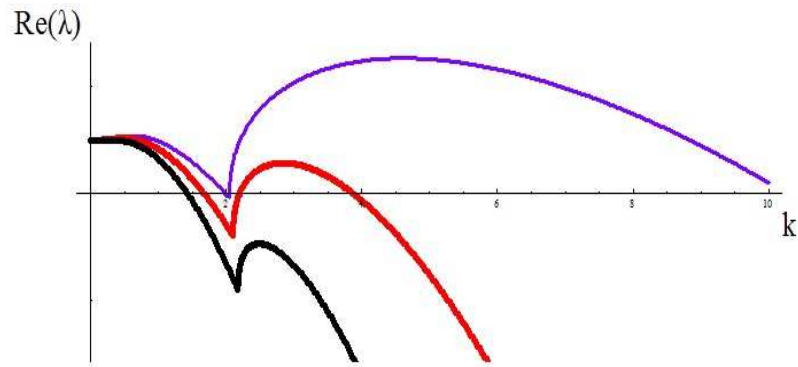


Figure 1. Dispersion relations exhibiting the interaction between the Turing and Hopf instabilities for different ratios between nonpolar intermediates and polar species confined in the microemulsion (D_s/D_x): 80 (violet curve), 40 (red), 8 (black). The model parameters to obtain this dispersion relations are $\alpha=8$;

$\beta=0.34$; $\gamma=0.2$; $\chi=0.$; $f=1.1$; $q=0.001$; $\varepsilon=0.37$; $\varepsilon_2=1.5$; $\varepsilon_3=0.006$;

Initially, we will consider the set of equations (1)-(4) in the absent of diffusion, *i.e.* without special considerations. This case resembles those reactions carried out under continuously stirring conditions in beakers. To do that, we use an Euler method with a time step of 0.01 time units (t.u.). Under these conditions, the BZ-AOT model exhibits an oscillatory solution with a characteristic period. Figure 2 (top) demonstrates this periodically behavior of the species concentration oscillating between a maximum and a minimum values.

Once diffusion was considered, simulations of equations (1)-(4) were performed by a Dufort-Frankel method in addition to Dirichlet and Newman conditions:

$$\begin{aligned} x(\bar{r}, t) \Big|_{t=t_0} &= x_{ini} \quad ; \quad \Big|_{\partial\Omega} \nabla x = 0 \\ z(\bar{r}, t) \Big|_{t=t_0} &= x_{ini} \quad ; \quad \Big|_{\partial\Omega} \nabla z = 0 \\ s(\bar{r}, t) \Big|_{t=t_0} &= s_{ini} \quad ; \quad \Big|_{\partial\Omega} \nabla s = 0 \\ u(\bar{r}, t) \Big|_{t=t_0} &= u_{ini} \quad ; \quad \Big|_{\partial\Omega} \nabla u = 0 \end{aligned}$$

Under Turing conditions (violet curve in Figure 1) we observed stationary patterns separated an equidistant wavelength. In Figure 2 (left panel) we show two characteristic Turing structures obtained by tuning the model parameters. The white (black) color in these figures stands for a high (low) concentration of the oxidized catalyst. Both kind of Turing patterns, spots and stripes, are experimentally achieved in the BZ-AOT system once the active micro-emulsion is sandwiched between two optical windows (Figure 2 right panel). The similitude between numerical and experimental patterns suggests that model (1)-(4) is a good candidate to display those structures obtained in the BZ-AOT system.

In addition to stationary Turing structures, the BZ-AOT system exhibits a rich variety of dynamics not possible without the confinement into nanodroplets, such as dashed waves, standing and packet waves, oscillons, segmented waves, etc [10-13]

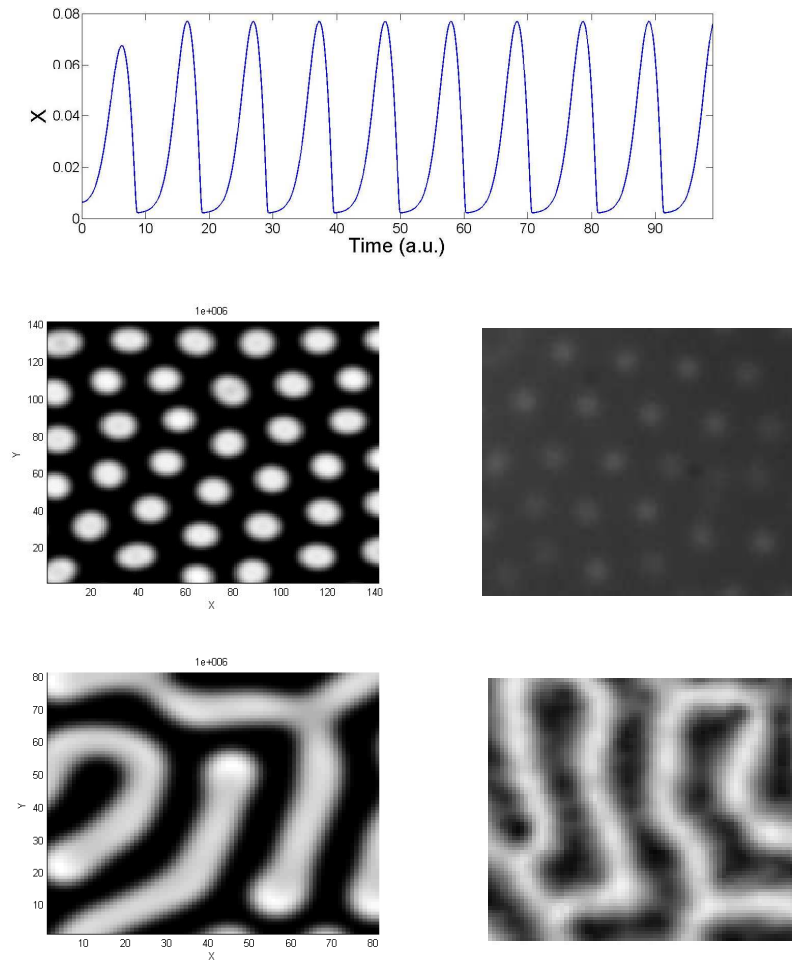


Figure 2. Model simulations of equations (1)-(4). Top: periodically temporal oscillations obtained in absence of diffusion. Middle and bottom: Two dimensional structures achieved numerically (left panel) and the comparative with experimental results (right panel) .

3. Conclusions

The confinement of a chemical oscillator into a micro-emulsion system generates a variety of spatial patterns not accessible without the compartmentalization. The diversity on pattern formation is understood by the presence of two different diffusion mechanisms. While Non-polar species may diffuse into the oleic phase, polar reagents are restricted to diffuse inside the nano-droplet system, being their diffusion coefficient considerably slower. The differences in the diffusion coefficients have been accounted by a four variable model, composed by two fast-diffusing species and two slow ones. We demonstrate the presence of Turing structures, which are patterns stationary in time with a characteristic spatial wavelength. Furthermore, we also present experimental results that qualitatively agree with our numerical simulations, validating our four variable model. It is remarkable to mention that there are several models to represent compartment active systems. They have been indiscriminately used to characterize the arising of new dynamics as well as the influence of external forcing into the well-known patterns [14-18]. Recently, cross-diffusion of the chemical reactants was considered one of the probable mechanisms to achieve such diversity of pattern formation and has been added to the model scheme [19].

References

1. B. P. Belousov, *Collected Abstracts on Radiation Medicine*. Moscow: Medgiz: A. V. Lebedinskii. Page 145 (1959.)
2. A.N. Zaikin, and A. M. Zhabotinsky, *Nature (London)*, 225, 535. (1970)
3. V. K. Vanag, *Phys.-Usp.*, 2004, 47, 923–941.
4. A.M. Cazabat, D. Langevin, D. and D.Pouchelon, *J. Colloid Interface Sci.*, 73, 1. (1980)
5. V.K. Vanag, and D.V. Boulanov, *JPhys. Chem.*, 1998, 1449 (1994)
6. E. Villar-Alvarez, *et al.* *The Journal of Chemical Physics*, 134 094512 (2011)
7. J. Carballido-Landeira, P. Taboada and A. P. Muñuzuri, *Phys. Chem. Chem. Phys.*, 13, 4596, (2011)
8. R.J. Field, and R.M. Noyes, *J. Chem. Phys.*, 60, 1877 (1974)
9. Strogatz, S. 1994. *Nonlinear Dynamics and Chaos*. Massachusetts: Perseus Books.
10. V. K. Vanag and I. R. Epstein, *Phys. Rev. Lett.* **87**, 228301 (2001).
11. J. Carballido-Landeira *et al.*, *Phys. Chem. Chem. Phys.*, 10, 1094-1096, (2008)
12. V. K. Vanag and I. R. Epstein, *Phys. Rev. Lett.* **88**, 088303 (2002).
13. V. K. Vanag and I. R. Epstein *Phys. Rev. Lett* 92, 128301 (2004)
14. J. Guiu-Souto *et al.*, *Phys. Rev. E*, 82, 066209, (2010)
15. J. Carballido-Landeira, V. K. Vanag and I. R. Epstein, *Phys. Chem. Chem. Phys.*, 12, 3656-3665, (2010)

16. A. Kaminaga, V.K. Vanag, and I.R. Epstein. *Angew. Chem. Int. Ed.*, 118, 3159–3161. (2006)
17. J. Guiu-Souto *et al.*, *Soft Matter*, DOI: [10.1039/c3sm27624d](https://doi.org/10.1039/c3sm27624d) (2013)
18. J. Carballido-Landeira, P. Taboada and A. P. Munuzuri, *Soft Matter*, 8, 2945 (2012)
- V. K. Vanag, F. Rossi, A. Cherkashin, and I. R. Epstein, *J. Phys. Chem. B* **112**(30), 9058 (2008)

Chaotic Dissipative Raman Solitons

Vladimir L. Kalashnikov

Aston University, Institute of Photonic Technologies, School of Engineering & Applied Science, Aston Triangle, Birmingham, B4 7ET, UK
(E-mail: v.kalashnikov@aston.ac.uk)

Abstract. A new type of dissipative solitons is announced. The numerical simulations based on the generalized nonlinear complex Ginzburg-Landau equation demonstrate that this soliton (dissipative Raman soliton, DRS) develops in the normal dispersion regime under effect of the stimulated Raman scattering (SRS). The SRS causes the red-shift and re-shaping of a soliton spectrum as well as changes a soliton group velocity. The main effects of SRS on a dissipative soliton are the chaotization of a soliton dynamics, the automodulational fragmentation of a soliton envelope and the enhancement of a tendency to multiple pulsing. As a result, a DRS becomes "noisy" and loses a property of energy scalability that troubles a high-energy pulse generation from mode-locked ber lasers.

Keywords: dissipative solitons, stimulated Raman scattering, chaotic modeling, generalized nonlinear complex Ginzburg-Landau equation.

1 Introduction

In the last decade, the concept of a dissipative soliton (DS), that is a strongly localized and stable structure emergent in a nonlinear dissipative system far from the thermodynamic equilibrium was actively developing and became well-established. This concept is highly useful in very different fields of science ranging from field theory and cosmology, optics and condensed-matter physics to biology and medicine [1]. Non-equilibrium character of a system, where the DSs emerge requires from them a well-organized energy exchange with an environment. In an optical system, the resonant and nonlinear coupling with such an environment causes a number of effects, in particular, the stimulated Raman scattering (SRS). In the last case, a light (photons) propagating through some medium (e.g., fiber) is scattered by oscillatory modes (phonons) of the latter [2]. As was found, the SRS can affect the DSs dramatically [3].

In this work, the results of numerical analysis of the DS dynamics affected by a strong SRS are presented. The testbed for such an analysis is the generalized nonlinear complex Ginzburg-Landau equation (generalized NCGLE), which is a common NCGLE (e.g., see [4]) supplemented with the SRS term in a general form as well as with the term describing a white quantum noise. To the best of



our knowledge, such a stochastic generalized NCGLE is considered for the first time.

The analysis demonstrates that the DS stability changes drastically, when the SRS becomes strong that is when the DS energy is large. The SRS destabilizes a DS and causes chaotization of its dynamics. The most interesting result is that a new type of DS develops in the presence of SRS. This DS can be named “dissipative Raman soliton” (DRS) because it is i) frequency down-shifted and ii) has a strongly inhomogeneous phase (i.e., “chirped”). The last property indicates the strong coupling of a DRS with an environment (i.e., this soliton is dissipative indeed). Also, it is found that the DRS dynamics is chaotic.

2 Generalized nonlinear complex Ginzburg-Landau equation

Simplest and most studied models for nonequilibrium phenomena in nonlinear systems are based on the different versions of NCGLE [1,5,6]. We will consider the following generalized version of the cubic-quintic NCGLE:

$$\begin{aligned} \frac{\partial a(z,t)}{\partial z} = & i \left[\frac{\beta}{2} \frac{\partial^2}{\partial t^2} - (1 - f_R) \gamma |a(z,t)|^2 \right] a(z,t) + \\ & + \left[-\sigma + \alpha \frac{\partial^2}{\partial t^2} + \kappa \left(1 - \zeta |a(z,t)|^2 \right) |a(z,t)|^2 \right] a(z,t) - \\ & - i f_R \gamma a(z,t) \int_{-\infty}^{\infty} dt' R(t') |a(z,t-t')|^2 + \chi(z,t). \end{aligned} \quad (1)$$

In particular, Eq. (1) can be interpreted in the following way. $a(z,t)$ is a slowly varying amplitude of light wave package, where z and t are a longitudinal propagation distance and a “local time”, respectively. In a laser, the propagation distance is simply resonator round-trip number in the framework of the distributed model. The local time is associated with a group velocity of wave package (e.g., see [7]). First row of Eq. (1) is a so-called nonlinear Schrödinger equation and describes the nondissipative factors such as a group velocity dispersion with the coefficient β and a self-phase modulation with the coefficient γ . Second row generalizes the nonlinear Schrödinger equation with taking into account the dissipative factors such as a saturable loss with the coefficient σ , a spectral dissipation with the coefficient α and a nonlinear gain with the coefficient κ . The nonlinear gain is saturable (the coefficient of saturation is ζ). The saturable net-loss is supposed to be energy-dependent: $\sigma = \varepsilon \left(\int_{-\infty}^{\infty} dt' |a(z,t')| \right) / E_s - 1$, where $\varepsilon = 0.05$ and E_s is a variable parameter defining the energy inflow in a system. These two rows of Eq. (1) give the cubic-quintic NCGLE, which is the basic model for analysis of an ultrashort pulse generation in both solid-state and fiber lasers.

We invent two physically relevant sophistication of the common cubic-quintic NCGLE (third row in Eq. (1)). 1) Since both amplification and dissipation in a laser produce inevitably the quantum fluctuations, Eq. (1) has to be stochastic that is provided by inclusion of the stochastic term χ . This term describes a complex white noise with the correlation function

$\langle \chi(z', t') \chi^*(z, t) \rangle = \Gamma \delta(z' - z) \delta(t' - t)$ (the noise “power” is $\Gamma = 10^{-10}/\gamma$ in our case). 2) At the high energy levels, the SRS becomes strong in fiber lasers [3]. Its influence is taken into account by the first term in third row of Eq. (1). We do not use the common approximation for this term in the form of the Taylor series expansion (e.g., see [8]). That allows the adequate description of an frequency conversion and energy flows for a DS affected by SRS.

In Eq. (1), the SRS is characterized by the response function [2]

$$R(t) = \frac{T_1^2 + T_2^2}{T_1 T_2^2} e^{-t/T_2} \sin\left(\frac{t}{T_1}\right), \quad (2)$$

where $T_1 = 12.2$ fs defines the Stokes frequency and $T_2 = 32$ fs defines the width of a Stokes line. The parameter $f_R = 0.22$ is defined by the Raman gain. All these numerical values correspond to a fused silica.

Eq. (1) was solved numerically by the symmetrized Fourier split-step method. The integral in Eq. (1) was evaluated in the Fourier domain on the basis of the convolution theorem. The size of temporal window and the propagation step were varied, the local time step was equal to 1 fs.

3 Results and discussion

The Raman lines in a fiber form a broad joined line that corresponds to a comparatively large T_2 . Since the DS developing in the normal dispersion regime ($\beta > 0$ in Eq. (1)) is stretched due to a large chirp, its width $T \gg T_2$ and one may expect that the SRS will play a substantial role in the dynamics of such solitons. The reason is that the group velocities of a Raman pulse and an ordinary DS differ due to dispersion. As a result, a Raman pulse must have an ample time for amplification during a time period, when it and a DS are overlapping [9]. On the other hand, the Raman frequency shift in a fiber is comparatively large (small T_1). But the DS spectral width is large as well (again due to a large chirp). Therefore one may expect an effective interpulse Raman scattering [2] in this case.

The calculations demonstrate that the SRS begins to contribute nontrivially into the DS dynamics and properties, when the DS energy $E \equiv \int_{-\infty}^{\infty} |a(z, t')|^2 dt'$ exceeds some threshold value (≈ 20 nJ in an all-fiber laser [9]). In the model under consideration, the DS energy is defined mainly by the parameter E_s . As was demonstrated in Ref. [10], the DS parametric space of the cubic-quintic NCGLE is two-dimensional and the relevant coordinates of this space are: $E' \equiv E_s \kappa^{3/2} \sqrt{\zeta}/\gamma \sqrt{\alpha}$ and $C \equiv 2\alpha\gamma/\beta\kappa$. Below, this dimensionless representation of the DS parametric space will be used.

For some fixed energy E_s , the multiple DSs appear when the dispersion β is relatively small (Fig. 1). These DSs redistribute an overall energy so that the energy of individual soliton becomes relatively small. As a result, the SRS does not affect their dynamics: there are no an extra group-delay and a transformation of spectrum.

The dispersion growth suppresses multipulsing so that a sole DS develops. Further growth of dispersion increases the difference of velocities between the

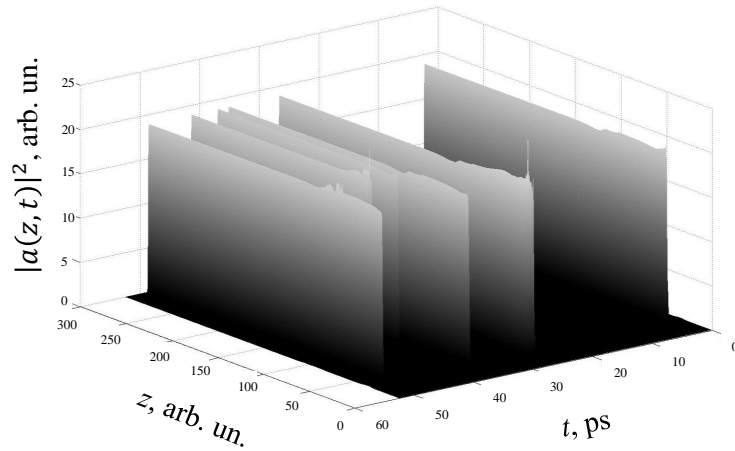


Fig. 1. Evolution of multiple DSs for $E' = 111$ and $C = 0.732$.

red and blue spectral components of a chirped pulse (remind that the DS phase is inhomogeneous) that stretches a DS. If the energy is sufficiently large, such a pulse becomes flat-top that corresponds to the energy scalable regime, when the peak power is fixed ($\approx 1/\zeta$). An energy scalable DS with the fixed peak power can remain stable if the energy growth, provided by energy inflow from an environment is compensated by the DS broadening [11].

For a comparatively small dispersions, i.e. in the vicinity of multipulsing threshold, the SRS causes i) pulse acceleration (i.e., growth of the group velocity in comparison with that of ordinary DS), ii) irregular perturbations at pulse traveling edge (where the blue spectral components are located), iii) chaotical evolution of the DS peak power, and iv) DS spectrum splitting (Fig. 2).

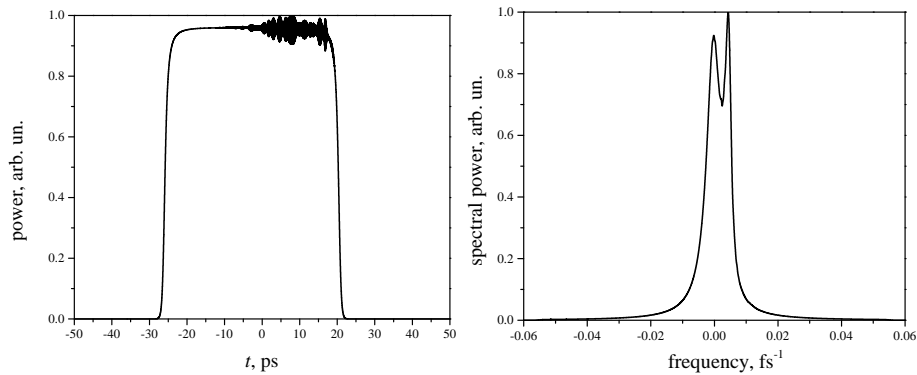


Fig. 2. Left: DS profile $|a(z = \text{const}, t)|^2$. Right: DS spectral power vs. frequency deviation from the central frequency corresponding to zero spectral dissipation (see second term of second row in Eq. (1)). $E' = 111$ and $C = 0.59$. Physically, the parameters correspond to an Yb-all-fiber laser with a 40 nm gain bandwidth.

Further dispersion growth enhances the DS acceleration. The pulse becomes noisy that is its envelope is strongly and irregularly perturbed and resembles a glass of boiling water (Fig. 3, left). As a consequence, the peak power evolves chaotically. Simultaneously, the regular (“solitonic”) part of the spectrum shifts into red-domain while the blue spike becomes intensive and irregular (Fig. 3, right).

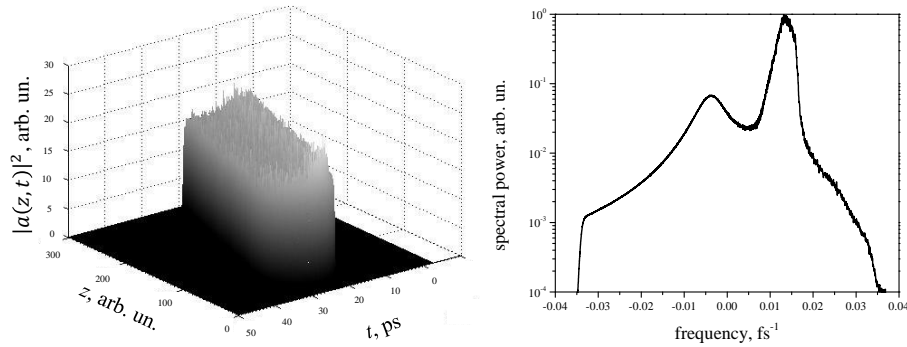


Fig. 3. Left: evolution of the DS profile $|a(z, t)|^2$. Right: logarithm of the averaged DS spectral power vs. frequency deviation. Averaging is performed over the interval $\Delta z = 2000$ with the step $\delta z = 10$. $E' = 111$ and $C = 0.244$.

Unlike the regime without SRS, larger dispersions cause the multipulsing yet again (Fig. 4, left) so that the domain of single pulse generation becomes confined along C -dimension. The chaotization of the peak power evolution and the perturbations of the DS traveling edge increase in parallel with the dispersion growth. The red part of the spectrum rises and shifts to lower frequencies.

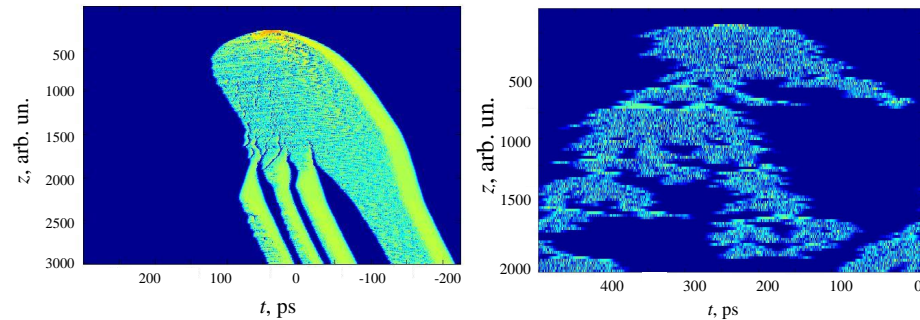


Fig. 4. Contour plot of the DS power evolution with (left) and without (right) SRS. Left: $E' = 111$, $C = 0.22$ and $F = 0.22$. Right: $E' = 111$, $C = 0.0366$ and $F = 0$.

Further increase of dispersion leads to a generation of DRS complexes. The example of such complex is shown in Fig. 5. Again, the traveling DRS edge is

perturbed that causes chaotic changes in the peak power evolution (Fig. 6, left). The chaotic character of evolution can be identified by the continuum-like RF spectrum of peak power set (Fig. 6, right). The spectrum splits in two separated parts shifted in opposite sides relatively the central frequency. Both parts have truncated edges (see inset in Fig. 5, right) that is the typical property of a chirped DS. The main part of the spectrum is red-shifted and modulated due to interference between DRSs.

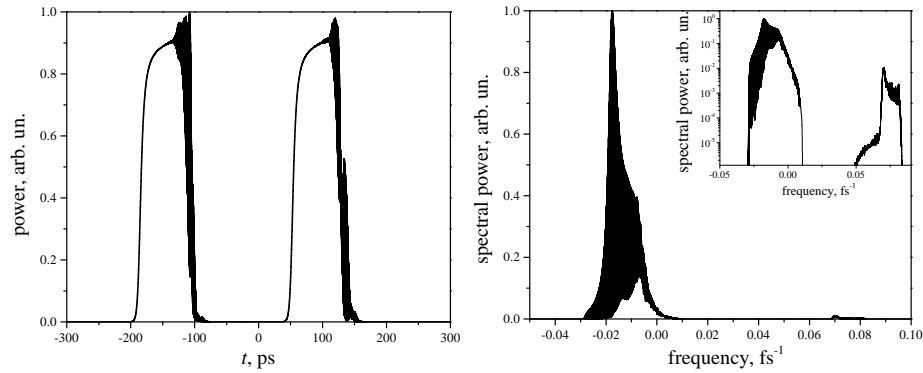


Fig. 5. Left: DS profile $|a(z = \text{const}, t)|^2$. Right: averaged DS spectral power vs. frequency deviation. Averaging is performed over the interval $\Delta z = 1000$ with the step $\delta z = 10$. Inset shows the spectrum on a logarithmic scale. $E' = 111$ and $C = 0.0366$.

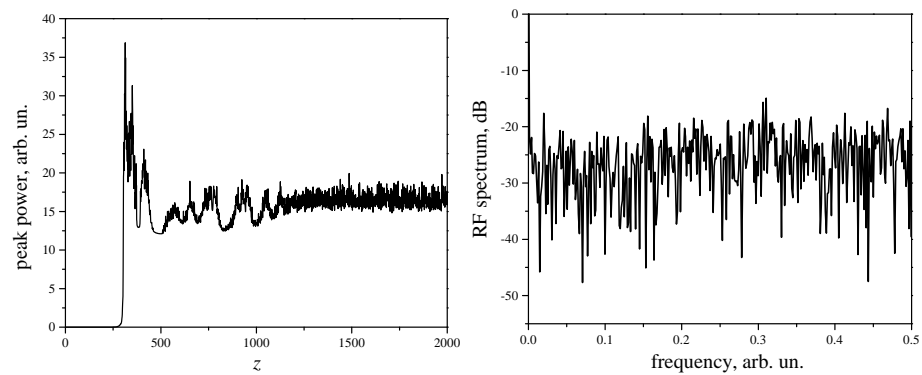


Fig. 6. Left: Evolution of DRS peak power. Right: RF spectrum of the peak power set over last interval $\Delta z = 750$. $E' = 111$ and $C = 0.0366$.

Why do we name the entity in Fig. 5 as a “dissipative Raman soliton”? First of all, one has to note that the spectrum in Fig. 5, right is a sum of almost identical spectra of individual pulses in Fig. 5, left. That is each pulse has a spectrum with both Stokes- and anti-Stokes “steep hills”. Such a spectrum is

not possible in an ordinary dissipative system with only self-phase modulation, second-order dispersion and spectral dissipation terms. Moreover, the main part of energy is concentrated in the lower frequency domain. All these observations suggest that the SRS contributes substantially into the pulse properties, both temporal and spectral. At last, truncated shape of the spectrum (inset in Fig. 5, right) suggests that the pulse is strongly chirped, i.e. it has a substantially inhomogeneous phase [10]. But the last fact testifies the nontrivial energy flows inside a pulse as well as between a pulse and environment [4]. Also, one has to add that there exists no DS without SRS for the parametrical set of Figs. 5, 6. The dynamics becomes completely chaotic without SRS in this case (Fig. 4, right). It is clear, that the SRS plays a crucial role in the DS stabilization for the large dispersions due to some “negative passive feedback” provided by spectral shift from the minimum of the frequency dissipation. Thus, one may conclude that the SRS is a formative factor for the DS considered so that such a soliton can be named a “dissipative Raman soliton”.

A passive negative feedback produced by the combined action of SRS and spectral dissipation enhances the tendency to multipulsing. The energy of individual DS in the multiple pulse complex is lower than that of single DS. Therefore, the frequency shift due to SRS is lower, as well. As a result, the spectral loss is lower too. Thus, the multipulsing becomes more advantageous energetically. This tendency to multipulsing in combination with the chaotization of DS dynamics in the presence of SRS confine the DS energy scalability.

4 Conclusion

For the first time to our knowledge, a new type of dissipative solitons of the generalized cubic-quintic nonlinear complex Ginzburg-Landau equation was described and analyzed. Such solitons emerge under action of stimulated Raman scattering in the presence of white quantum noise and can be named “dissipative Raman solitons”. Changes in the DRS characteristics with the dispersion growth were traced and a complicated structure of the region, where DRS exists, was established. It was found that the dynamics of DRS is chaotic due to irregular perturbation at the soliton traveling edge. A two-compound character of the DRS spectrum was revealed so that the soliton spectrum consists of Stokes- and anti-Stokes spices with truncated edges. The last fact suggests that the DRS considered is strongly chirped. It was demonstrated that the DRS can exist in the regions of large dispersion where an ordinary DS does not emerge. Simultaneously, the SRS leads to an additional spectral loss in a system with the spectral dissipation. This confines a DS energy scalability.

Acknowledgments

This work was supported by the FP7-PEOPLE-2012-IAPP (project GRIFFON, no. 324391).

The computational results have been achieved using the Vienna Scientific Cluster (VSC).

References

1. Dissipative Solitons, N. N. Akhmediev and A. Ankiewicz, editors, Springer, Berlin, 2005.
2. G. P. Agrawal. Nonlinear Fiber Optics, Academic Press, Oxford, 2013.
3. A. E. Bednyakova, S. A. Babin, D. S. Kharenko, E. V. Podivilov, M. P. Fedoruk, V. L. Kalashnikov, A. Apolonski. Evolution of dissipative solitons in a fiber laser oscillator in the presence of strong Raman scattering. *Opt. Express*, 21:20556–20564, 2013.
4. N. Akhmediev, A. Ankiewicz. Dissipative solitons in the complex Ginzburg-Landau and Swift-Hohenberg equations. In N. N. Akhmediev and A. Ankiewicz, editors, *Dissipative Solitons*, pages 1–17, Springer, Berlin, 2005.
5. Nonlinear Waves: Classical and Quantum Aspects, N. N. Akhmediev and A. Ankiewicz, editors, Kluwer Academic Pub., Dordrecht, 2004.
6. Dissipative Solitons: From Optics to Biology and Medicine, N. N. Akhmediev and A. Ankiewicz, editors, Springer, Berlin, 2008.
7. N. N. Akhmediev, A. Ankiewicz. Solitons: Nonlinear Pulses and Beams, Chapman & Hall, London, 1997.
8. N. Akhmediev, W. Królikowski, A. J. Lowely. Influence of the Raman-effect on solitons in optical fibers. *Optics Commun.*, 131:260–266, 1996.
9. D. S. Kharenko, E. V. Podivilov, A. A. Apolonski, S. A. Babin. 20 nJ 200 fs all-fiber highly chirped dissipative soliton oscillator. *Opt. Lett.*, 37:4104–4106, 2012.
10. V. L. Kalashnikov, E. Podivilov, A. Chernykh, A. Apolonski. Chirped-pulse oscillators: theory and experiment. *Applied Physics B*, 83:503–510, 2006.
11. V. L. Kalashnikov. Chirped-Pulse Oscillators: Route to the Energy-Scalable Femtosecond Pulses. In A. H. Al-Khursan, editor, *Solid State Laser*, pages 145–184, InTech, 2012.